Dissertation

zur Erlangung des Doktorgrades der

Fakultät für Mathematik und Physik der

ALBERT LUDWIGS UNIVERSITÄT FREIBURG

Tracking Performance of Micromegas Chambers for the ATLAS New Small Wheel Project

---

Vorgelegt von

Patrick Scholer

am

22. Dezember 2021

Betreuer: Prof. Dr. Ulrich Landgraf
Fakultät für Mathematik und Physik
Albert-Ludwigs-Universität Freiburg

Patrick Scholer: Tracking Performance of Micromegas Chambers for the ATLAS New Small Wheel Project

---

Dekan:	Prof. Dr. Michael Thoss
Leiter der Arbeit:	Prof. Dr. Ulrich Landgraf
Referent:	Prof. Dr. Ulrich Landgraf
Koreferent:	Prof. Dr. Beate Heinemann
Tag der Verkündung des Prüfungsergebnisses:	07.03.2022

Kurzzusammenfassung

Ab dem kommenden Datennahmezeitraum wird die innerste Endkappe des Muon Spektrometers des ATLAS Experiments durch das "neue kleine Rad" (New Small Wheel, NSW) ersetzt. Im NSW werden die beiden Technologien Micro-Mesh Gaseous Detectors (Micromegas) und small-strip Thin Gap Chambers zum Einsatz kommen, um sowohl die Selektion von physikalisch interessanten Ereignissen als auch die Rekonstruktion der Teilchenspuren zu verbessern. Dies ist notwendig, da im Rahmen des Ausbaus des LHCs zum High-Luminosity LHC stark erhöhte Teilchenraten erwartetet werden. Der Fokus dieser Dissertation liegt auf der Rekonstruktion von zu erwartenden geneigten Teilchenspuren mit den Micromegas Detektoren im NSW. Der erste von zwei Teilen dieser Arbeit beschäftigt sich mit der Charakterisierung der Rekonstruktionsleistung eines der ersten Micromegas Module aus der Serienproduktion in einer dedizierten Teststrahl Kampagne. Für die Rekonstruktion von geneigten Teilchenspuren wurden zwei Methoden untersucht: die micro Time Projection Chamber (μTPC) und die Cluster Time Projection (CTP) Methode. Während das temporär hohe Hintergrundrauschen im verwendeten experimentellen Aufbau einen negativen Einfluss auf die Ergebnisse der μTPC Methode, insbesondere auf die Rekonstruktionseffizienz, hatte, konnte mit der CTP Methode eine Präzision von 212 μm bei einer Rekonstruktionseffizienz von 90 % und mehr erreicht werden. Im zweiten Teil dieser Arbeit wurde die Simulationsoftware der Micromegas Detektoren innerhalb des ATLAS Software Frameworks erheblich verbessert, und mehrere Parameter der Detektorsimulation wurden optimiert, um die Signale der echten Detektoren bestmöglich nachzubilden. Des Weiteren wurden verschiedene Rekonstruktionsmethoden für geneigte Teilchenbahnen in die Software integriert. Deren Leistung und Genauigkeit wurde für verschiedene Detektorkonfigurationen, basierend auf simulierten Detektordaten, untersucht. Auch in diesen Studien stellte sich die CTP Methode als die beste heraus. Daher wird sie in Zukunft für die präzise Rekonstruktion von Myon-Spuren eingesetzt werden, welche einen entscheidenden Anteil am äußerst erfolgreichen Physikprogramm der ATLAS Kollaboration haben.

Abstract

For the upcoming data taking period, the innermost end-caps of the ATLAS Muon Spectrometer will be upgraded with the New Small Wheels (NSWs), deploying Micro-Mesh Gaseous Detectors (Micromegas) and small-strip Thin Gap Chambers for improved tracking and trigger capabilities at increased collision rates introduced by the High-Luminosity LHC upgrade. This dissertation focuses on the reconstruction of inclined tracks with the Micromegas detectors, as they will be present in the NSW. The first of two parts of the thesis covers a dedicated test beam campaign, where the position reconstruction performance of one of the first Micromegas modules from the series production was investigated. Focus was laid on the reconstruction of clusters from inclined tracks, employing two different reconstrution algorithms, the micro Time Projection Chamber (μTPC) and the Cluster Time Projection (CTP) methods. While the performace of the μTPC method, especially in terms of the reconstruction efficiency, suffered from the exceptionally high noise levels observed temporarily in the test beam, the CTP method was able to reconstruct clusters with a precision of 212 μm at efficiencies of 90 % and above. In the second part of this thesis, the simulation of the Micromegas detectors inside the ATLAS offline software, athena, has been significantly improved and several parameters have been optimized in order to better mimic the response of the actual detector. Furthermore the reconstruction algorithms for inclined tracks have been integrated into athena, and their performance was studied for different physics scenarios obtained from the detector simulation. The CTP method showed the most promising results and will therefore be used for the precise reconstruction of muon tracks in ATLAS, which is of key importance for the physics program of the collaboration.

Thank you for everything, Stephanie!

Contributions by the Author

This thesis work was carried out within the ATLAS New Small Wheel (NSW) collaboration. Contributions were made in, amongst others, two major fields of the project, which are discussed in the following:

The author participated in two test beam campaigns. A short first one took place in April 2018 and was targeted at the validation of the final readout chip deployed in the NSW, the VMM3a, mounted on a small Micromegas prototype detector. The second test beam, the results of which are reported in this document, took place in summer 2018 and lasted over five weeks. In both test beam campaigns, the author took a leading role in both the operation of the detectors during data taking and the subsequent data analyis. In the analysis, especially for inclined tracks, the author was one of two main analysers, and all results presented in part II, other than figure 8.2, were exclusively produced by him based on an almost entirely self-written analysis software. The results were presented in various ATLAS internal meetings and as a poster at the Micro-Pattern-Gaseous Detector Conference 2019 (MPGD19) in La Rochelle, France, which was followed up by a proceeding [1]. Furthermore several public plots summarizing the test beam results were created and can be found on the public results page of the NSW [2].

Also the contributions to the ATLAS offline software, athena, described in part III of this thesis were made almost exclusively by the author, including the different improvements to the event digitization and the development of the constrained μTPC method, as well as the adaptations of the other cluster reconstruction methods for the use in athena. The production and analysis of all samples of simulated events needed for the studies presented in this document were also done by the author, while making significant contributions to dedicated analysis tools developed in collaboration with the NSW software working group. The author conceptually developed the correction of the magnetic field and the calibration of the raw data, leaving the technical implementation to other members of the collaboration. The results from the cosmic ray test stand used for the comparison of the digitization output to data were provided by the corresponding working group, in which the author contributed to the not-yet-finished analysis of the time resolution. For the simulation itself, a set of public plots regarding the results of the optimization of the digitization and the performance of the reconstruction methods was prepared as part of this thesis and is published in [2].

Contents

Glossary

ADC analog-to-digital converter

ASIC application-specific integrated circuit

BCID Bunch Crossing ID

CERN European Organization for Nuclear Research

CKBC Bunch Crossing Clock

CMS Compact Muon Solenoid

CS charge sharing

CTF clock and trigger generation and fanout

CTP Cluster Time Projection

DUT device under test

ENC equivalent noise charge

FPGA field-programmable gate array

HL-LHC High-Luminosity LHC

HT Hough transform

HV high voltage

ID Inner Tracking Detector

IP interaction point

LHC Large Hadron Collider

LHCb Large Hadron Collider beauty

LS2 Long Shutdown 2

MIP minimum ionizing particle

Micromegas Micro-Mesh Gaseous Detector

MS Muon Spectrometer

NL neighbor logic

NSW New Small Wheel

PCB printed circuit board

SM Standard Model

SPS Super Proton Synchrotron

sTGC small-strip Thin Gap Chamber

SW Small Wheel

TAC time-to-amplitude converter

μTPC micro Time Projection Chamber

1. Introduction

The progress of humanity has always been driven by the curiosity to explore the phenomena observed in nature, leading to a better understanding of its fundamental principles and underlying structures. In modern particle physics, the underlying structure of all forms of matter discovered so far and the interactions among them is explained by the Standard Model (SM). In the past century the SM was tested in a variety of experiments, many of them located at particle colliders. The success of those experiments is outstanding and lead to the discovery of all elementary particles predicted in the current formulation of the SM, the most recent one being the Higgs boson discovered in the year 2012 by the ATLAS and CMS experiments [3, 4]. These two experiments are analyzing the proton-proton collisions happening in the Large Hadron Collider (LHC) at the European Organization for Nuclear Research (CERN).

The success of collider experiments was and will always be driven by pushing the accelerator equipment to the technological limit and beyond. Achieving higher and higher magnetic fields strengths, e.g. by inventing superconducting magnets, allows for higher beam energies while other innovations assist the increase of luminosity in the colliders. In order to keep up with the improving particle accelerators, many groundbreaking developments are also present in the field of particle detection. While historically information about particle tracks was reconstructed by analyzing photographs of particles passing through so-called bubble chambers, today's state-of-the-art detectors are read out fully automatically with an ever-improving precision and rate, withstanding more and more extreme environments due to, e.g., the high rate of ionizing radiation or increased magnetic fields inside experiments.

Although the discovery of the Higgs boson filled the last vacant position in the SM, many observations, which cannot be explained by it yet, impose the need to conduct further, even more detailed measurements of the SM. In order to achieve an increased sensitivity, the LHC is undergoing several successive upgrades mostly targeting a higher luminosity. The final stage of the upgrades leading to the High-Luminosity LHC (HL-LHC), are scheduled for the year 2027. In the light of the forthcoming HL-LHC also the experiments located at the interaction points of the LHC, need to undergo continuous improvement. One such upgrade already being installed for the upcoming data taking period starting early 2022, is the replacement of the innermost end-cap of the ATLAS Muon Spectrometer by the New Small Wheel (NSW). Micro-Mesh Gaseous detectors (Micromegas) and small-strip Thin Gap Chambers are deployed in the NSW in order to maintain an excellent muon track resolution at the increased particle rates expected from the HL-LHC, and also to improve the ability to select scientifically relevant collisions with high momentum muons in the final state in real time.

This dissertation is dedicated to the characterization of the tracking performance of the Micromegas detectors employed in the NSW, especially for the case of inclined tracks. The thesis is divided into three parts. Part I serves as an introduction and also contains a description of the methodologies deployed later. Chapter 2 gives a short overview of the SM with a focus on the muon. Then the theory of gaseous detectors, which are widely used in the detection of muons, is briefly described, followed by an overview of the LHC and the ATLAS experiment. Chapter 5 then introduces the NSW. First the motivation for replacing the current Small Wheel is given, followed by a short discussion of the deployed detector technologies and the overall mechanical structure. Chapter 6 discusses Micromegas detectors in more detail. Then the working principles of several algorithms to reconstruct the position of strip clusters created by the ionizations of a charged particle track in the Micromegas gas volume are described. Special focus is put on the case of inclined particle tracks, where the drift time information, obtained for each Micromegas strip, needs to be exploited in order to guarantee a precise position reconstruction.

In part II, the study of the performance of one of the first Micromegas chambers from the series production is presented. The investigations had two major goals: the validation that the VMM front-end chip works well on a full-size Micromegas chamber and the characterization of the module for inclined particle tracks. Chapter 7 first introduces the overall test beam setup and the readout system, including the VMM front-end chip and its calibration which was carried out in the scope of this thesis. The results of the performance studies are discussed in chapter 8, while chapter 9 summarizes the test beam studies.

Part III describes the contributions that were made to the ATLAS software in connection to the integration of the Micromegas detectors. Chapter 10 focuses on the improvements developed for the simulation of the detector and the electronics response of the Micromegas, referred to as digitization. In the second half of that chapter, studies are presented which compare quantities of strip clusters, between simulated events and data obtained with the final detectors. Those comparisons aim at optimizing the physics configuration of the Micromegas digitization in order to get a simulated response corresponding to the real detector as close as possible. Other than the simulation of events, the ATLAS software is also used to reconstruct the properties of final state particles emerging from the proton-proton collisions. Major contributions have been made to the Micromegas part of the reconstruction software. They are described in chapter 11 and include the technical implementation and optimization of the cluster reconstruction algorithms, studies of their performance, and finally the procedure to calibrate the cluster positions as a function of the magnetic field. Chapter 12 provides a summary of the software part.

Chapter 13 recapitulates the entire thesis and puts the results in context with the requirements on the detector performance as imposed by both the HL-LHC scenario and the ATLAS physics program.

Part I.

Theoretical and Experimental Foundations

In this part a brief introduction is given to the theoretical and experimental framework this thesis is embedded in. First, the Standard Model of particle physics is introduced in chapter 2, highlighting the importance of muon detection in modern-day particle physics experiments, which is what this thesis is centered around. In chapter 3, the theoretical concepts of gaseous detectors, widely deployed in muon reconstruction, are discussed. Since this dissertation was carried out in the context of the New Small Wheel upgrade of the ATLAS detector, the experiment itself is introduced in chapter 4, with a particular focus on the Muon Spectrometer and the event simulation and reconstruction software. The discussion of ATLAS is preceeded by a short description of the LHC and its upgrades. Chapter 5 is dedicated to the New Small Wheel upgrade of the Muon Spectrometer of ATLAS, including its motivation, a description of the detector technologies deployed, and an overview of its mechanical structure. Finally chapter 6 describes the Micromegas detector technology in detail. The second part of that chapter discusses different reconstruction algorithms used to reconstruct strip clusters in Micromegas detectors, especially focusing on drift time based methods which are critical in order to precisely reconstruct inclined particle tracks. The study of the performance of those methods is the main focus of this thesis.

2. Muon Physics

This dissertation is dedicated to the study of the detection and reconstruction of *muons* which are elementary particles belonging to the category of leptons. All observable particles are described by the *Standard Model* (SM) which serves as the theoretical backbone for modern particle physics research and is introduced in this chapter. Furthermore the second part of this chapter discusses the properties of the muon and its special role within the SM, making it an ideal tool for high energy experiments.

2.1. The Standard Model of Particle Physics

The SM of particle physics, e.g. see [5], is a renormalizable [6] quantum field theory with underlying gauge groups $SU(3)_C \times SU(2)_L \times U(1)_Y$ that describes all known elementary particles and all known fundamental forces except gravity. In this section, a short overview of the elementary particles included in the SM is presented, followed by a discussion of observed phenomena that cannot be explained within the framework of the SM.

2.1.1. Content of the Standard Model

Figure 2.1 shows the elementary particles contained in the SM, which come in two main groups. The first class of particles, called *fermions*, are characterized by having half-integer spin, while particles belonging to the second class, referred to as *bosons*, have an integer number as spin. The role of the elementary bosons inside the SM is to mediate the interactions between all particles, while all matter discovered so far is made out of fermions, lending them the name *matter particles*. The three fundamental interactions, also referred to as forces, that are explained by the SM are the electromagnetic, the weak, and the strong force. The strong (electromagnetic) interaction is described by the theory of quantum chromodynamics (QCD) (quantum electrodynamics (QED)) based on the SU(3) (U(1)) symmetry group, while the understanding of the weak force follows the SU(2) symmetry in the framework of quantum flavor dynamics (QFD). While the strong interaction couples to so-called color charge, the electromagnetic (weak) force couples to electric charge (weak hypercharge). The strength of the different interactions corresponds to the different coupling constants and varies by multiple orders of magnitudes. The coupling strength of the weak (electromagnetic) interaction is of the order 10^{13} (10^2) times smaller compared to that of the strong force [8], taking into account the properties of the mediator particles. It needs to be noted that Glashow, Salam and Weinberg were able to unify the description of the electromagnetic and the

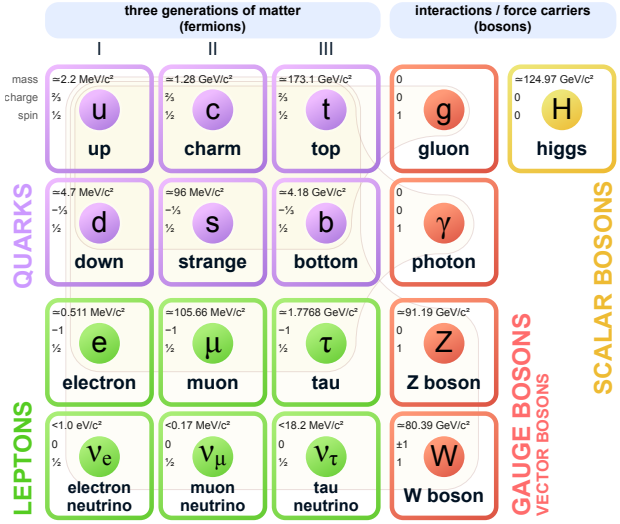

Figure 2.1.: Fundamental particles of the standard model. Modified from [7].

weak force into one common gauge theory with the underlying symmetry $SU(2)_L \times U(1)_Y$ [9–11], referred to as the *electroweak* force.

There are 12 so far discovered, elementary fermions contained in the SM which can be split into two groups: quarks and leptons. So-called up-type quarks carry an electrical charge of $+1/3\,e$, where e stands for the elementary charge, as opposed to down-type quarks whose electrical charge is $-2/3\,e$. Both types of quarks come in three so-called generations, where the first (third) generation of quarks has the lowest (highest) mass. The six instances of quarks are called flavor, and changes between the different flavors are mediated by the weak charged force exclusively. All flavors of quarks carry color charge and, hence, are subject to the strong interaction. Also the leptons come in three generations. There are three flavors of leptons that carry an electric charge of $-1\,e$, namely the electron e, the muon μ, and the tau lepton τ. The other three lepton flavors, called neutrinos, are electrically neutral and according to the current formulation of the SM do not have mass. The latter stands in contradiction to observations which will be discussed in the next section. All types of leptons carry a weak hypercharge but no color charge, therefore neutrinos only interact via the weak force while the remaining lepton flavors are also subject to the electromagnetic interaction.

As discussed above, three of the four fundamental interactions can be described by quantum field theories, where the excitation for these fields are known and referred to as the mediators of the corresponding interaction. Since all of them are spin-1 particles, they are also called *vector bosons*. For QED, the mediator particle is the photon. It is massless and carries no electric charge, therefore it does not couple to itself, and the coupling strength of the electromagnetic interaction decreases with $1/r^2$. In QCD, the interactions are mediated by gluons. They are massless and also do not carry electrical charge but unlike all other vector bosons, gluons do not only couple to particles with color charge but carry color charge themselves, resulting in self-interactions. In

contrast to QED, the interaction strength in QCD does not decline with the distance, but increases with r. This has two consequences: the first one is called confinement. It describes the fact that at low energies, corresponding to large distances, quarks cannot be observed on their own but only in composite states referred to as hadrons. There are two categories of hadrons, mesons and baryons, defined by a baryon number of 0 and 1 respectively, where (anti-)quarks have a baryon number of $+1/3$ ($-1/3$) respectively. One prominent example for a baryon is the proton, a composite state of two up and one down quark. The second consequence of the interaction strength increasing with distance is the effect of asymptotic freedom. At large energies, equivalent to small distances between quarks, the coupling strength of the strong force gets small and quasi-free quarks can be observed. This allows the investigation of the substructure of hadrons and is therefore the basis of many modern-day high energy physics experiments by relying on deep inelastic scattering of hadrons. The first experiments based on deep inelastic scattering were conducted at SLAC in the late 1960s [12, 13].

The situation is different for the weak interaction whose three exchange particles, the $W^{\pm}$ and the Z bosons, do not only carry the weak hypercharge, but in case of the $W^{\pm}$, also electrical charge. Additionally, they are also very massive compared to the proton where the mass of the W bosons is 80.4 GeV while the Z boson weighs 91.2 GeV [14]. When understood as excitations of an underlying locally gauge-invariant quantum field based on the SU(2) symmetry group, one would have expected the three aforementioned bosons to be massless. Since this is in clear contradiction to the experimental results, the common theory of the electroweak force needs to be amended. In an intuitive understanding, this was done by imposing the breaking of the $\mathrm{SU}(2)\times\mathrm{U}(1)$ symmetry via random interactions of the electroweak fields with a yet unknown scalar field, a process called spontaneous symmetry breaking. The process of spontaneous symmetry breaking itself was first proposed by Yoichiro Nambu [15] in 1960, based on his work on superconductors. Two years later three independent research groups almost simultaneously published an exact formulation of the mechanism explaining how the spontaneous symmetry breaking introduces masses in the SM [16–18]. It is called the Englert–Brout–Higgs–Guralnik–Hagen–Kibble (BEH) mechanism named after the authors. The mechanism requires the presence of a new scalar field with a massive excitation, which has been discovered by the ATLAS and *Compact Muon Solenoid* (CMS) collaborations in 2012 [3, 4]. The boson corresponding to the excitation of the new field is called the Higgs boson (H) and according to the latest measurements it has a mass of $(125.25 \pm 0.17)\,\mathrm{GeV}$ [14]. The BEH mechanism does not only explain the masses of the heavy vector bosons but also allows fermions to obtain mass via the so-called Yukawa coupling to the Higgs field.

2.1.2. Phenomena Not Described by the Standard Model

The SM is one of the most tested theories of modern science. It is able to describe the known matter extremely well, but some empirical observations remain unexplained by the theory in its current form. Three of the most prominent of these are briefly discussed in the following.

Neutrino Masses: The mathematical formulation of the SM is based on the assumption that neutrinos are massless, but in multiple experiments the so-called neutrino oscillations were observed [19]. The term refers to the effect that neutrinos periodically change their flavor, e.g. an electron neutrino becomes a muon neutrino, as a function of time, oscillating between all three generations of leptons. This is only possible if the neutrinos have mass. Measurements of the absolute neutrino mass are ongoing and an upper limit of 0.8 eV could be determined [20]. Due to these almost negligible masses the predictions of the SM are still accurate within the precision of current experimental measurements. Several proposed extension of the SM are available aiming at an explanation of the neutrino masses, many of them are based on the so-called seesaw mechanism.

Cosmological Phenomena: The observed velocity of constituents of galaxies, e.g. stars, as a function of the distance to the galactic center does not match with the theoretical expectation. Since most of the visible matter is located close to the center of the galaxy, one should presume a decline of the rotation velocity with increasing radius. But it was observed that the velocity is actually constant or even increases at larger radii [21]. This indicates that there must be some form of heavy matter that barely interacts with the known particles, the so-called dark matter. Another hint for the existence of dark matter is that, e.g., gravitational lensing cannot be explained because the visible matter is not sufficient to bend the light and create the patterns that are observed. Cosmological measurements suggest that the visible matter, explained by the SM, only makes up about 5 % of the total matter and energy content of the Universe, while the rest is accounted for by dark matter and another concept called dark energy.

Unification of Forces and Gravity: The SM contains the description of three of the four fundamental forces: the electromagnetic, the weak, and the strong force. The fourth yet missing interaction is gravitation. As discussed above, it was already possible to unify the electromagnetic and the weak forces into the common electroweak interaction, meaning that their coupling strengths become equal at higher energies. However a unification of all four forces and thus a consistent formulation including a quantum theory of gravity was not yet successful.

In order to explain these shortcomings of the SM a variety of theories beyond the SM were developed, most of which include the introduction of new and heavy particles. A lot of effort has been made in the past years in order to search for and hopefully find any signs of new physics phenomena by many experiments scanning a large energy range. Furthermore the various parameters of the SM are re-measured with an ever improving precision in order to detect any inconsistencies that may indicate the existence of new particles.

2.2. The Muon

The muon is a second generation lepton with a mass of 105 MeV [14]. Its charge is $-1\,\mathrm{e}$ and its lifetime is $2.2\,\mu\mathrm{s}$. [14]. It was discovered in 1936 by Carl Anderson and Seth Neddermeyer [22] studying ionizing particles from *cosmic rays*, i.e. the particle flux we receive from outer space. Further studies carried out in reference [23] confirmed the existence of the new type of particle as suggested by Anderson and Neddermeyer. In the cosmic radiation muons are created as the product of a two-step process. First incoming ionizing radiation from space, mostly protons, interacts with the gas molecules of the Earth's atmosphere creating a type of light mesons that are called pions. Those then further decay into muons. Due to time dilation and their long lifetime, muons are able to reach the surface of the Earth without decaying beforehand. They arrive at the surface with a rate of about $1/(\mathrm{cm}^2\,\mathrm{min})$ and given this abundance, cosmic muons are often used for tests of detectors which require ionizing particles. While their mean energy is 4 GeV they offer a very wide energy spectrum that is useful in these kind of measurements.
Due to its high mass, the muon loses much less energy per travelled path length compared to lighter charged particles like the electron. Details on this will be given in section 3.1. Together with its long lifetime, the limited energy loss lends the muon a very unique signature in modern particle physics experiments. It is able to travel through huge amounts of material, e.g. calorimeters, while the long lifetime makes it possible to reconstruct the trajectory of muons over a long distance. Together with a magnetic field this allows a very precise momentum measurement, given the huge lever arm.
Both its low energy loss and its lifetime make the muon an important tool in searches for unknown particles and the precision measurements of SM parameters. An example is the discovery of the Higgs boson [3,4] which relied on, amongst others, the decay into two Z bosons which subsequently produced four muons that could be detected in the experiments. Muons also played a role in the discovery of the Z itself in 1983 [24]. One example where the muon is used to precisely determine SM parameters is the study of the decay of a B meson, i.e. a composite state of a b quark and a u or d quark, into a lighter meson called a Kaon and two leptons. In the current formulation of the SM this decay should take place at an equal rate (up to a mass correction) for both electrons and muons, however, there is evidence obtained by the *Large Hadron Collider beauty* (LHCb) collaboration that the process yields more decays into electrons than into muons [25]. This precision measurement involving muons could open the door for future discoveries.

3. Muon Detection with Gaseous Detectors

Gaseous particle detectors are deployed in a broad range of applications since they offer excellent particle detection properties while being cheap, compared to other technologies, and having a low material budget. The latter property is important since, in contrast to, e.g., calorimeters, gaseous detectors are mainly used to track particles where as little distortion of the particle track as possible is desired. In particle physics experiments located at colliders, the main use for gaseous detectors is the detection of muons which requires the precise tracking of particles in large volumes of magnetic fields and therefore huge detector volumes. Gaseous detectors are ideal in this case since they offer good tracking performance, short dead times, and also good time resolution for fast event preselection.
This chapter introduces the basic theory of gaseous detectors. It mostly follows [26]. First it discusses the primary and secondary ionizations of the active gas by a charged particle passing through the detector, followed by a description of the motion of electrons in electromagnetic fields. Finally the process of charge amplification is introduced.

3.1. Interaction of Charged Particles with Matter

The dominant processes of energy loss for low-energetic, charged particles passing through matter are the ionization and excitation of atoms or molecules. For particles that are heavier than the electron, the mean energy loss $\mathrm{d}E$ per path length $\mathrm{d}x$ due to ionization and excitation is described by the Bethe-Bloch formula [26]:

$$-\left\langle \frac{\mathrm{d}E}{\mathrm{d}x} \right\rangle = K \frac{Z}{A} \rho \frac{z^2}{\beta^2} \left[\frac{1}{2} \ln \frac{2\, m_e\, c^2 \beta^2 \gamma^2\, T_{max}}{I^2} - \beta^2 - \frac{\delta(\beta\gamma)}{2} - \frac{C(\beta\gamma, I)}{Z} \right], \tag{3.1}$$

where z is the charge of the incoming particle in units of the elementary charge and β is its velocity divided by the speed of light. All other quantities depend on the detector medium: Z is its atomic number and A its mass, I is the mean ionization energy, δ a correction for the density, and T_{max} the maximum energy that can be transferred to the orbital electron. $C(\beta\gamma, I)$ is a shell correction that is relevant for low β values. The last three terms in the bracket are relativistic and quantum mechanical corrections to the energy loss. They can be considered small compared to the logarithmic term.
Figure 3.1 shows the mean energy loss per path length of an anti-muon in copper versus its momentum. For slow muons, the energy loss is dominated by the $1/\beta^2$ pre-factor while for faster

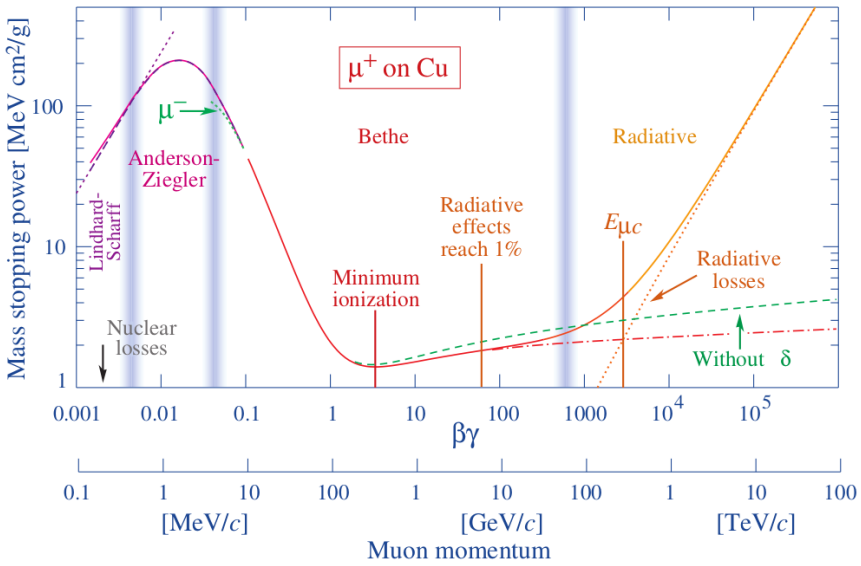

Figure 3.1.: Energy loss of anti-muons in copper. For a wide range of muon momenta between a few MeV and a few 100 GeV, the dominant energy loss mechanism is ionization and excitation of the copper atoms. The mean energy loss in this region is described by the Bethe-Bloch formula. Particles at $\beta\gamma = 3.5$ are called minimum ionizing particles due to the large plateau of low energy loss. Above a momentum of a few hundred GeV the radiation becomes the dominant process where the energy loss rises linearly with the muon momentum. Figure taken from [27].

ones the $\ln(\gamma)$ term takes over. In between, there is a region of minimal energy loss, with only small dependence on the momentum. Particles in this region are therefore called *minimum ionizing particles* (MIPs). A prominent example of MIPs are muons created in interactions of charged particles from outer space with the atmosphere of the earth, referred to as *cosmic muons*. At muon momenta above a few hundred GeV, radiative losses start to become larger than the losses through ionization and excitation. This leads to a linear increase of the energy loss as a function of momentum. Further processes that cause primary ionizations in gaseous detectors are photons which ionize the detector gas (e.g. via the photo effect, Compton scattering, or pair production), and neutrons that interact with the nuclei of the detector gas. At modern colliders with high luminosities and therefore large numbers of neutrons created, this is an important background to the detection of muons.

All the processes described so far create so-called *primary ionizations*. Some of the electrons created in these primary ionizations have enough energy to ionize further gas molecules. This process is called *secondary ionization*. As a reference, a MIP crossing 1 cm of pure argon gas typically produces 29.4 primary ionizations. Including the secondary ionizations, this number rises to 94 ionizations in total. The amount of secondary ionization per primary ionization is randomly distributed. Since an initial electron with high energy is needed, the most probable

value for the number of secondary ionizations is zero but the distribution has large tails towards high numbers of secondary ionizations. This implies that the charge created along the muon track is not equally distributed, leading to a degradation of the position resolution of the detector as will be discussed in section 6.3.

3.2. Motion of Charged Particles in Electromagnetic Fields

After the ionization processes discussed above have happened, an electrical field applied to the gas volume forces the electrons to drift towards an electrode, where they can be detected. This field is reffered to as *drift field*. Therefore the motion of electrons in electromagnetic fields will be discussed in the following.
The distribution of a charge cloud, i.e. multiple electrons from ionizations, in a medium is described by the Boltzmann transport equation [26]:

$$\frac{\mathrm{d}f}{\mathrm{d}t} = \frac{\partial f}{\partial t} + \frac{\mathrm{d}\vec{r}}{\mathrm{d}t}\vec{\nabla}_{\vec{r}} f + \frac{\mathrm{d}\vec{v}}{\mathrm{d}t}\vec{\nabla}_{\vec{v}} f = \frac{\partial f}{\partial t}_{|\mathrm{coll}}, \tag{3.2}$$

where $f(\vec{r}, \vec{v}, t)$ is the distribution of the charge cloud in the six-dimensional phase space. The term on the right describes the interaction of the charge cloud with the medium, e.g., through collisions. The second term in the partial derivative describes the diffusion of the charge cloud while the third one refers to changes in the velocity. The latter one is induced by external electromagnetic fields dictating the term $\mathrm{d}\vec{v}/\mathrm{d}t$. A detailed discussion of the solutions for the equation is given in [26]. From these solutions macroscopic quantities of the charge cloud like drift velocity and diffusion can be obtained, as discussed below.

3.2.1. Drift Velocity

The drift velocity of the charge cloud is given by the mean velocities of its particles:

$$\vec{v}_D = \langle \vec{v} \rangle = \int \vec{v}\, f(\vec{v})\, \mathrm{d}\vec{v}. \tag{3.3}$$

In the case of thermal motion, $f(\vec{v})$ is symmetric around zero and therefore the drift velocity of the cloud will vanish. Applying an external electric or magnetic field to the cloud will skew $f(\vec{v})$, leading to a non-vanishing $\vec{v}_D$. In the following, two relevant scenarios of fields in gaseous detectors will be discussed: first, the case of applying only an electric field with a single component, $\vec{E} = (0, 0, E)$, and second, the combination of the electric field with a magnetic field being perpendicular to $\vec{E}$, e.g. $\vec{B} = (0, B, 0)$. Solving the Boltzmann transport equation for the first scenario and putting the resulting $f(\vec{v})$ into equation 3.3 [26] leads to:

$$v_{D,3} = \frac{qE}{m}\left(\frac{2}{3}\left\langle\frac{\lambda}{v}\right\rangle + \frac{1}{3}\left\langle\frac{\mathrm{d}\lambda}{\mathrm{d}v}\right\rangle\right) = \mu\, E, \tag{3.4}$$

where λ is the mean free path length of the electrons and μ stands for the mobility. The components $v_{D,1}$ and $v_{D,2}$ are vanishing. Introducing the mean time between two collisions as

$$\langle \tau \rangle = \left\langle \frac{\lambda}{v} \right\rangle, \tag{3.5}$$

and adding the assumption that λ is not changing significantly with the velocity, the mobility can be written as

$$\mu = \frac{2}{3} \frac{q}{m} \langle \tau \rangle. \tag{3.6}$$

In the second scenario of applying an additional magnetic field perpendicular to the electric one, equation 3.3 solves [26] to give

$$\begin{aligned} v_{D,1} &= \frac{qE}{m} \left\langle \tau \frac{\omega\tau}{1+\omega^2\tau^2} \right\rangle, \\ v_{D,2} &= 0, \\ \text{and} \quad v_{D,3} &= \frac{qE}{m} \left\langle \tau \frac{1}{1+\omega^2\tau^2} \right\rangle, \end{aligned} \tag{3.7}$$

with the synchrotron frequency

$$\omega = \frac{q}{m} B. \tag{3.8}$$

Two observations on the drift velocity can be made from equation 3.7. First, the drift velocity gets reduced with increasing values of B and therefore ω:

$$\frac{v_D^B}{v_D^0} = \frac{\sqrt{(v_{D,1})^2 + (v_{D,3})^2}}{|v_D^0|} = \frac{1}{1+\omega^2\tau^2}, \tag{3.9}$$

where the mean value from the right side of equation 3.7 has been replaced by assuming an effective τ. The second observation is that the drift direction becomes non-parallel to the electric field lines. The angle between the drift direction and the electric field lines is called the *Lorentz angle* α_L, and it can be calculated as follows:

$$\tan \alpha_L = \frac{|v_{D,1}^B|}{v_{D,3}^B} = \omega\tau. \tag{3.10}$$

It can be seen that $\tan \alpha_L$ increases for increasing values of ω and therefore increasing magnetic field strength.

3.2.2. Diffusion

While drifting through the gas, the electrons and ions undergo several random scattering events, leading to a deviation of the drift path of the individual particles from the drift direction of the

particle cloud $\vec{v}_D$. This deviation is called *diffusion* and it leads to an increase of the size of the particle cloud. The amplitude of the diffusion follows a Gaussian distribution:

$$\rho\left(\vec{r},t\right) = \left(\frac{1}{4\pi\, D\, t}\right)^{\frac{3}{2}} \exp\left(-\frac{\vec{r}^{\,2}}{4\, D\, t}\right), \tag{3.11}$$

where $\vec{r}$ is the displacement from the path, t is the time, and D is the diffusion constant for electrons passing the active detector medium. For a constant drift velocity $\vec{v}_D$ and in the thermal limit where the electrons and ions have an energy of $\epsilon = {}^3\!/_2 kT$, the width of the distribution is given by

$$\sigma_x = \sqrt{2Dt} = \sqrt{\frac{2Dx}{v_D}} = \sqrt{\frac{2kTx}{qE}}, \tag{3.12}$$

where x is the drift distance from the initial point of charge creation and E is the electric field causing the drift. For higher electric fields the diffusion is not isotropic anymore but splits into a component parallel to the drift field, called *longitudinal diffusion*, and into a component perpendicular to the field, the so-called *transverse diffusion*.

3.3. Charge Avalanche

Close to the electrode most gaseous detectors have a much stronger electric field compared to the drift field, leading to a multiplication of the number of electrons. This is required in order to achieve a low enough signal-to-noise ratio, allowing the detection of ionizations in the detector. In this context *signal* refers to the number of electrons arriving on an electrode, which were created in actual ionizations due to a charged particle crossing the detector, and *noise* refers to the charge induced from, e.g., the thermal motion of electrons. In the following the process of charge multiplication in gaseous detectors is introduced. First the process itself together with descriptive quantities is discussed, followed by a description of effects which limit the gain. The fluctuation of the gain is briefly addressed and finally different operation regions of gaseous detectors and their fields of application are given.

3.3.1. Townsend Coefficient

At very high strengths of externally applied electric fields, the primary electrons obtain enough energy between two collisions to ionize the gas molecules and the electrons created in these ionizations themselves subsequently ionize further gas molecules. This process, where a single electron creates a charge cloud, is called a *gas avalanche*. Given the exponential characteristics of the process, the number of electrons $\mathrm{d}N_e$ created per path length $\mathrm{d}x$ is given by

$$\mathrm{d}N_e = N_e\, \alpha\, \mathrm{d}x, \tag{3.13}$$

where α is the so-called Townsend coefficient,

$$\alpha = \sigma_{ion}\, n = \frac{1}{\lambda_{ion}}, \tag{3.14}$$

with σ_{ion} being the cross section for the ionization of a gas molecule, n the density of the gas, and λ_{ion} the mean free path between two collisions leading to an ionization. The gas gain, G, is then defined as the ratio between the initial number of electrons, N_0, and the number of electrons, N, yielded by the avalanche:

$$G := \frac{N}{N_0} = \exp\left(\int_{x1}^{x2} \alpha(x)\, \mathrm{d}x\right). \tag{3.15}$$

Given that the ionization cross section depends on the kinetic energy of the electrons provided by the external field, the Townsend coefficient becomes dependent on the electric field. Furthermore, since both the mean free path and therefore also the pressure of the gas vary with its density, the Townsend coefficient and the gas gain also depend on it. Rose and Korf tried to approximate these dependencies with the following formula [28]:

$$\frac{\alpha}{p} = A \exp\left(-B\frac{p}{E}\right), \tag{3.16}$$

where A and B are constants that characterize the gas mixture used in the detector, p is the pressure, and E is the electric field. It can be seen that the Townsend coefficient increases exponentially with the external electric field. Its dependency on the pressure is given by the combination of a linearly increasing term and an exponentially decreasing one.

3.3.2. Raether Limit

If the gas gain reaches values of order 10^8, a sufficient number of electrons and ions are produced to build an electric field acting against the external field causing the avalanche. This eventually leads to a region were the electric field is canceled out allowing the electrons and ions to recombine rather than drift apart and therefore the avalanche stops. This maximum gain is called the Raether limit. The recombination process then yields photons which again ionize the detector gas leading to the formation of new avalanche clouds. The combination of multiple avalanche clouds leads to a so-called streamer which can be seen due to the accompanying emission of photons. If the streamer reaches the electrode, the ion cloud forms a plasma which establishes a conducting connection between the anode and the cathode resulting in an emission of sparks. Compared to a purely electron-driven avalanche, the photons travel an order of magnitude faster. Therefore some detector types rely on the creation of streamers to have a fast signal, but it can also lead to serious damage on the electrodes for other detectors types. One way to suppress the creation of streamers is the admixture of so-called *quenching gases* to the operation gas. The quenching gas absorbs the photons emitted by the recombination into rotational and vibrational states and therefore blocks the creation of further avalanches. Typical examples of quenching gases are CO_2

or isobutan, while, e.g., Argon can serve as active gas. Another method to suppress streamers is to introduce resistive electrodes. In that case the current, induced by the streamer, flows through the electrodes leading to an ohmic voltage drop along its path. This reduces the effective voltage at the point where the streamer hits the electrode, subsequently leading to a reduction of the local amplification field which stops the charge multiplication.

3.3.3. Gain Fluctuations

As described above, the gas avalanche process relies on the collision of electrons with the gas molecules. Since this is a statistical process, also the gain itself varies for each avalanche. To describe the gain fluctuations in homogeneous fields, the so-called Polya function is used. It describes the probability to observe a certain gain value, $P(G)$, as following:

$$P(G) = C_0 \frac{(1+\theta)^{1+\theta}}{\Gamma(1+\theta)} \left(\frac{G}{\bar{G}}\right) \exp\left(-(1+\theta)\frac{G}{\bar{G}}\right), \tag{3.17}$$

with θ being related to the relative gain variance $f = 1/(1+\theta)$ and $\bar{G}$ describing the mean gain. Although the Polya distribution has no physical derivation, it accurately describes the data.

3.3.4. Operation Regions of Gaseous Detectors

Gaseous detectors are often categorized according to the gain they are operated at, which spans over several orders of magnitude depending on the use case of the detector. Figure 3.2 shows the major gain regions which are briefly discussed following the description in [26].

Recombination Region In the case of a weak electric field applied, the chance for a recombination of electrons and ionized gas molecules is higher than for the electrons to arrive at the electrode. Hence the gas gain is below 1 and only some fraction of the originally created electron-ion pairs induce a signal on the electrodes.

Ionization Region This region is characterized by a gas gain of around 1, which is too low to identify individual particles, as they create only a few electrons in the primary and secondary ionization processes. It is used to measure particle flows, e.g., in dosimeters.

Proportional Region With a gas gain of $10^1 - 10^5$, the signal is proportional to the initial amount of ionizations. This mode allows the measurement of a single charged particle penetrating the detector together with the number of primary or secondary ionizations it has created along its path in the detector. The latter is important to achieve a good reconstruction of the particle's position.

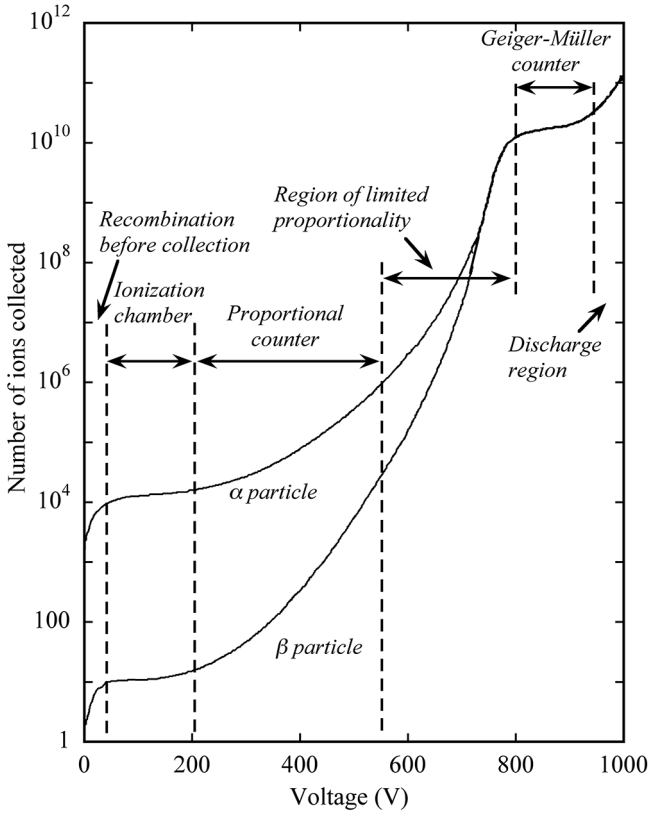

Figure 3.2.: Numbers of ions collected in a proportional counter as a function of the applied voltage. Figure taken from [29] following [30].

Limited Proportional Region At gains of $10^5 - 10^8$ the proportionality to the initial charge deposit gets limited due to space-charge effects reducing the strength of the amplification field.

Saturation and Geiger Region At gains around 10^{10} the signal is no longer proportional to the primary charge deposition. Since in this mode the detector produces many electrons per passing primary particle, a good signal-to-noise ratio can be achieved, allowing a readout with simpler and thus cheaper electronics. This is why this mode is often used to only count particles passing through the detector. However, compared to the proportional mode, the position of the particle cannot be determined as accurately.

Discharge Region At gains greater than 10^{10} the detector principle is based on gas discharges induced by particles passing the detector. This operation mode yields a very good time resolution since, as discussed above, photon-driven avalanches travel faster than purely electron-driven ones.

4. The Large Hadron Collider and the ATLAS Detector

The work of this thesis was carried out in the context of the upgrade of the Muon Spectrometer of the ATLAS experiment located at the *Large Hadron Collider* (LHC) at the *European Organization for Nuclear Research* (CERN), close to Geneva, Switzerland. In the first section of this chapter a brief introduction to the LHC, the largest particle accelerator in the world, is presented, together with the motivation and the technical details of its upgrade to the *High-Luminosity LHC* (HL-LHC). Section 4.2 then gives an overview of the ATLAS experiment, which is one of four main experiments at the LHC. The focus is placed on the Muon Spectrometer of ATLAS, whose upgrade is discussed in chapter 5.

4.1. The Large Hadron Collider

The LHC [31] is the world's largest circular particle accelerator. Since the start of its operation in 2008, it has already reached unprecedented values for both the beam energy and the collision luminosity. The LHC is built in a 27 km long tunnel, located at CERN. It is designed to accelerate two proton or heavy ion beams in opposite direction. Although the LHC's heavy ion program has lead to astonishing results, it will not be discussed any further herein as it was not relevant for this thesis.

The LHC is the last machine in a complex chain of accelerators shown in figure 4.1, which provide the proton beams at an energy of 6.5 TeV at the time of writing this thesis. While the design luminosity of $1 \cdot 10^{34}/(\mathrm{cm}^2\,\mathrm{s})$ could be exceeded during the second data taking period already, the design beam energy of 7 TeV has not yet been reached given technical limitations discussed below. The first element in the accelerator chain is the linear accelerator LINAC2[1]. Thereafter, the proton beams travel through the *Proton Synchrotron Booster*, the *Proton Synchrotron*, and the *Super Proton Synchrotron* (SPS), all of which are circular accelerators and each of which increases the kinetic energy of the beams, eventually reaching 450 GeV when leaving the SPS. Also the beam profiles are shaped to maximize the number of protons for one entire fill of the LHC. From the SPS the proton beams are inserted into the LHC where they are accelerated to the final energy at which they will ultimately be brought to collision at four designated *interaction point*s (IPs) that are spread along the circumference of the collider. Besides the filling of the LHC, the

[1] Up to now this was taken care of by the LINAC2 accelerator. For the next data taking period starting in 2022, the LINAC2 will be replaced by the LINAC4.

aforementioned pre-accelerators also provide beams to other experiments and test beam facilities located at CERN where new detector materials and prototypes are studied.

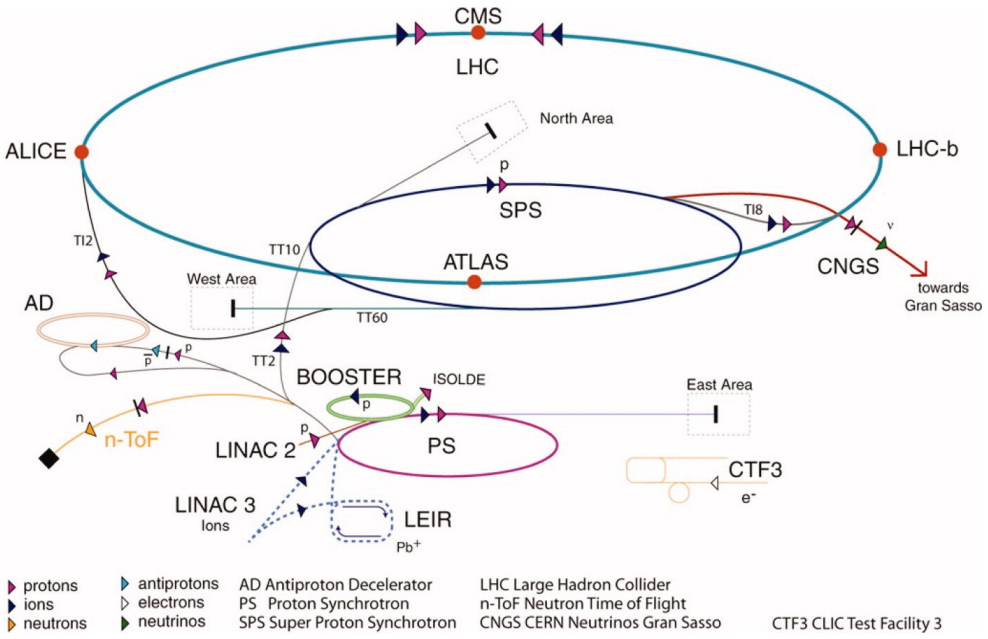

Figure 4.1.: Chain of accelerators at CERN. Before the proton beam arrives to the LHC, it travels through several pre-accelerators. First a linear accelerator is used, namely the LINAC2 after which the beam travels through the proton synchrotron booster (PSB), the proton synchrotron (PS), and finally the super proton synchrotron (SPS) which are all circular colliders. The different pre-accelerators also provide the beam to smaller experiments and test beam areas like the north area at the SPS. Figure taken from [32].

For the acceleration of the beams to the final energy, the LHC relies on 16 superconducting *radio-frequency* cavities. The cavities are operated at a voltage of up to 2 MV that rapidly alternates with a frequency of 40 MHz. Protons that enter the cavities first are attracted by the field. When the protons reach the center of the cavity, the polarity of the field changes, leading to a repulsion of the protons from the electrode through which they have entered while being attracted by the electrode at the exit of the cavity. Once the protons approach the second electrode, the polarity is changed again such that they now are repulsed by that electrode and thus pushed forward towards the next cavity. Besides the increase of beam energy, the alternating electric field also ensures the segmentation of the proton beam into so-called *bunches*. At the final beam energy, protons with the correct timing are not further accelerated by the cavities, but protons that arrive early (late) are decelerated (accelerated) such that the bunches are always spatially isolated. In this way, the cavity frequency determines the so-called *bunch separation* of 25 ns.
To keep the protons in a circular beamline, the LHC uses 1232 superconducting magnets operated at a field strength of 7.7 T, which is necessary given the LHC radius of more than 4 km and a beam

energy of 7 TeV. The strength of the magnetic field is also the limiting factor for further increasing the beam energy to its design value of 7 TeV. Magnets of higher order are employed to focus the beam, which is relevant especially before and after the two proton beams are collided. The entire magnetic system is cooled by liquid helium since it can only be operated at a temperature of 1.9 K. This is because otherwise the energy required by the magnets could not be provided whereas superconducting materials at this temperature have only negligible electrical resistance. In the LHC the two beams are collided at four locations. Each of the four collision points is surrounded by one or more detectors, recording the particles created in the collision. These detectors are:

- ATLAS [33] and the CMS [34], which are both multi-purpose detectors located at opposite positions of the LHC,
- *A Large Ion Collider Experiment* (ALICE) [35], focused on investigating the quark-gluon plasma created in the collisions of lead nuclei,
- the LHCb [36] detector, specialized for studying the properties and decays of b-quarks produced in the proton-proton collisions,
- and four smaller experiments, located in the vicinity of ATLAS and CMS. These are LHCf, TOTEM, FASER, and MODAL.

The most relevant observables to describe particle collisions are the beam energy and the instantaneous luminosity. The latter can be described as follows:

$$\mathcal{L} = \frac{f N N_1 N_2}{\sigma_x \sigma_y}, \tag{4.1}$$

where f refers to the revolution frequency of a bunch in the LHC, N denotes the number of bunches, N_i the number of protons in bunch i, and $\sigma_{x/y}$ defines the spatial size of the beam. The maximum number of bunches present in a complete fill of the LHC is 2556[2]. There are in the order of 10^{11} protons in a bunch and the size of the beam at the interaction points is in the order of a few μm. This yields an instantaneous luminosity of up to $2 \cdot 10^{34}/(\mathrm{cm}^2\,\mathrm{s})$, or $0.02/(\mathrm{pb}\,\mathrm{s})$, exceeding the design luminosity by a factor of 2.
The outstanding luminosity of the LHC is key to the physics program for which it has been designed, as will be motivated in the following based on the example of the decay of a Higgs boson into four leptons. Given its outstanding signal-to-background ratio, it was one of the Higgs discovery channels in 2012 [3, 4]. The rate at which the process takes place can be determined by taking the product of the luminosity and the cross section. Here the cross section is $\sigma_H = 3.28 \pm 0.3\ (\mathrm{stat.}) \pm 0.11\ (\mathrm{syst.})$ fb at a center-of-mass energy of 13 TeV [37]. At the above-mentioned peak luminosity this yields about 5.7 events per 24 h of data taking. While for the

[2]The intial LHC filling sheme foresaw a maximum of 2808 bunches, but with optimizations in the pre-accelerator, reducing the number of bunches, a better emmitance was achieved.

discovery of the Higgs boson only a few events were sufficed, the precise measurement of its properties needs thousands of events. Even at the current outstanding luminosity of the LHC this corresponds to several years of operation.
Since its start in 2008, the LHC has been subject to several upgrades with the ultimate one being the HL-LHC [38] scheduled for the years 2024 – 2027. The goal of these upgrades is the increase of beam energy and collision luminosity. As has just been demonstrated in the estimation above, the increase in luminosity is crucial to the improvement of the sensitivity to rare processes that involve, e.g, the Higgs self-coupling. Also it is essential in order to extend the phase space in the search for heavy, beyond Standard Model particles. Furthermore, a higher luminosity also allows for a more precise measurement of parameters predicted by the SM, e.g. the coupling strenghts. Figure 4.2 shows the timeline of the different LHC upgrade stages. After a first round of upgrades during the *Long Shutdown 1* the LHC operated with a beam energy of 6.5 TeV and already reached twice its design luminosity of $1 \cdot 10^{34}/(\mathrm{cm}^2\,\mathrm{s})$ at the end of the second data taking period ("run 2"). In total the LHC delivered 184.26/fb of proton-proton collisions from the start of its operation until the end of 2018 [39, 40]. At the time of writing this thesis, the *Long Shutdown 2* (LS2) is ongoing. In the LS2, among other things, civil engineering work in preparation of the HL-LHC is conducted, e.g. excavating new underground caverns, while also the experiments at the LHC are overhauled and improved in anticipation of the higher luminosity scenario. The actual upgrade of the LHC itself to the HL-LHC configuration will take place in the *Long Shutdown 3*. In order to reduce the beam size at the interaction points, which is how the luminosity is increased, the quadruplet magnets used to focus the beam will be replaced by stronger ones, reaching 12 T instead of the 8 T achieved so far. Also the beams will not be collided head-on anymore but will be tilted to increase the overlap. Therefore so-called crab cavities with a very precise phase alignment are under development. Furthermore the machine protection system, the bending magnets, and the superconducting power lines will need to be upgraded together with all the pre-accelerators. The ultimate goal of the HL-LHC is to operate at 7.5 times the nominal instantaneous luminosity of the LHC collecting up to 4000/fb of collision data by the end of its lifetime.

4.2. The ATLAS Detector

The ATLAS detector is a multi-purpose detector located at the LHC. It weighs around 7000 t, has a length of 44 m, and a diameter of 25 m. An overview of the ATLAS detector is given in figure 4.3. The detector has the shape of a cylinder which is centered around the collision point. It can be divided into three major regions, the barrel region and the two caps of the cylinder referred to as *end-cap* regions. The ATLAS detector consists of three major detector systems, namely the *Inner Tracking Detector* (ID), the calorimeters, and the *Muon Spectrometer* (MS). In the barrel region these are radially stacked around the beam pipe with the ID being the innermost system, followed by the calorimeters and the MS. In the end-cap regions the different systems are implemented as wheels which are stacked along the beam pipe. Besides the detector systems, ATLAS has a dedicated system of solenoidal and toroidal magnets assisting the measurement of

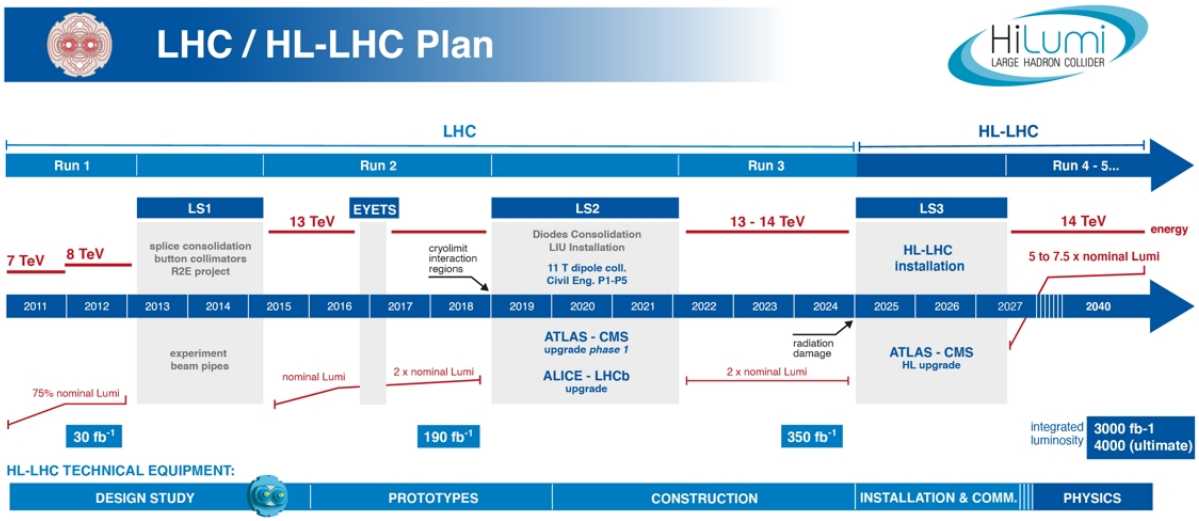

Figure 4.2.: Timeline of the High-Luminosity LHC upgrade. Figure adapted from [41].

the momentum of charged particles. In the following the different detector systems, the magnets, the data acquisition system, and the software used to simulate particles passing through ATLAS and to reconstruct the particle collisions are described, focusing on the MS which is relevant for this thesis. But first the coordinate systems used in ATLAS is discussed.

4.2.1. Coordinate System

In ATLAS, positions and directions are mostly described by two different coordinate systems: a Cartesian and a cylindrical one. The Cartesian one is used to represent the position of detector parts. In this system, the z-axis points along the beam pipe, the x-axis points to the center of the LHC ring, and the y-axis points upwards. However, particle tracks are usually described in a cylindrical coordinate system, with the z-axis being the same as for the Cartesian system. The azimuthal angle ϕ indicates the rotation around the beam axis and the polar angle θ specifies the opening angle between the particle track and the beam pipe. This opening angle can also be transformed into the pseudo-rapidity η:

$$\eta = -\ln\left[\tan\left(\frac{\theta}{2}\right)\right]. \tag{4.2}$$

An illustration of the two coordinate systems is given in figure 4.4.

4.2.2. Inner Tracking Detector

The detector system closest to the beam pipe is the ID. Its inner and outermost layers are located at radii of 31 mm and 1066 mm, respectively. The ID is composed of four layers of silicon pixel detectors at low radii, followed by four layers of silicon strip sensors. Further out,

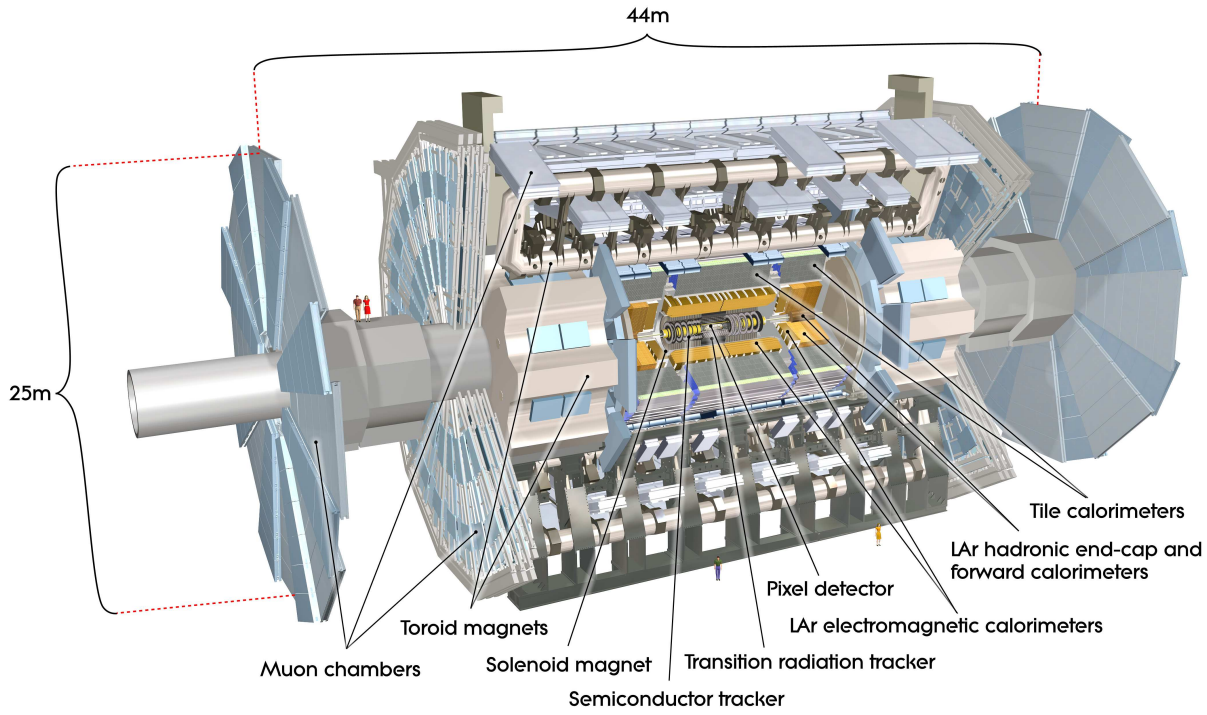

Figure 4.3.: Overview over the different detector systems of the ATLAS experiment. In the central region the three detector systems are radially stacked around the beam pipe. The innermost system is the inner tracking detector which is surrounded by the calorimeters. The outermost detector system is the Muon Spectrometer. In the end-cap region the three detector systems are implemented as wheels which are positioned orthogonally to the beam pipe. Two systems of magnets are used to allow for the measurement of the momentum of charged particles. In the inner detector a solenoidal field is present. In the Muon Spectrometer the field is produced by toroid magnets. Figure taken from [33].

a transition radiation tracker is used for tracking and electron identification. In the end-cap regions the same technologies are employed but with a different number of layers arranged in discs around the beam pipe. This arrangement of detectors allows for a very precise reconstruction of particle trajectories used to measure their momenta, to determine the primary vertex, and also to reconstruct secondary vertices from the decay of short-lived particles like b-hadrons. More information on the inner detector is given in [43–46].

4.2.3. Calorimeters

The inner detector is surrounded by the *electromagnetic* (ECAL) and the *hadronic* (HCAL) calorimeters. The calorimeter fully absorbs almost all particle types, except muons and neutrinos, and measures their energy deposits in the process. This allows to reconstruct the initial energy

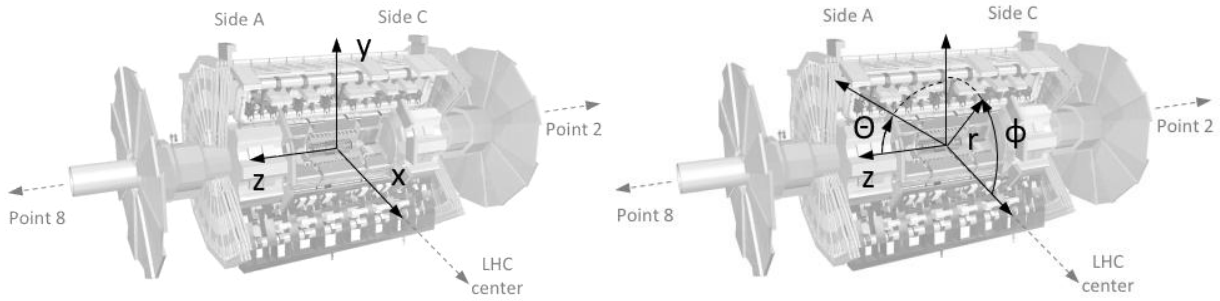

(a) Cartesian coordinate system.

(b) Cylindrical coordinate system.

Figure 4.4.: Graphical illustration of the two coordinate systems used in ATLAS. The left drawing shows the Cartesian coordinate system mainly used to identify the position of detector elements. The right drawing illustrates the cylindrical system mainly used to describe particle tracks. Figures taken from [42].

of the particles. All calorimeters in ATLAS are designed as so-called sampling calorimeters. This means that most of the energy is deposited in high density passive absorber materials and only a small energy fraction is absorbed in an active detector medium. The passive and active materials are alternated along the particle track. In the ECAL, liquid argon acts as the active detector medium, while lead is chosen as the absorber. The lead and the liquid argon layers are arranged in an accordion-like shape allowing to stack two to three active layers along the particle trajectory. This gives the possibility to determine the direction of flight of the particles, which is especially helpful for neutral particles like photons, since those are invisible in the inner tracker. The ECAL is surrounded by the HCAL. In the barrel region of the HCAL, scintillator tiles are deployed as active material and steel as absorber while in the end-cap region liquid argon and copper are used. Outside of the end-cap HCAL, the *forward calorimeter* (FCAL) is located. Its purpose is to measure particles very close to the beamline. It consists of copper and tungsten as absorbers and liquid argon as active detector medium. Further information on the calorimeters can be found in [33, 47, 48].

4.2.4. Muon Spectrometer

An overview of the Muon Spectrometer is given in figure 4.5. It is the outermost and also largest detector system of ATLAS, covering radii from 5 m up to 10 m. Its purpose is to track muons, the only charged particles escaping the calorimeters. It also needs to provide fast muon track information for the event preselection system that runs during data taking, referred to as *trigger* (see section 4.2.6). The MS makes use of four detector technologies arranged in three concentric circles around the beam pipe in the barrel region, and three so-called wheels on each side of the end-cap region. These six wheels are mounted orthogonally to the beam pipe. Despite its diameter of about 10 m, the innermost wheel of each side is referred to as *Small Wheel* (SW),

while the four outer ones, having a diameter of 24 m, are called *Big Wheels*. Two of the four technologies focus on the precise tracking of the muons, especially the bending in the magnetic field. The other two technologies are dedicated to obtaining fast particle information.

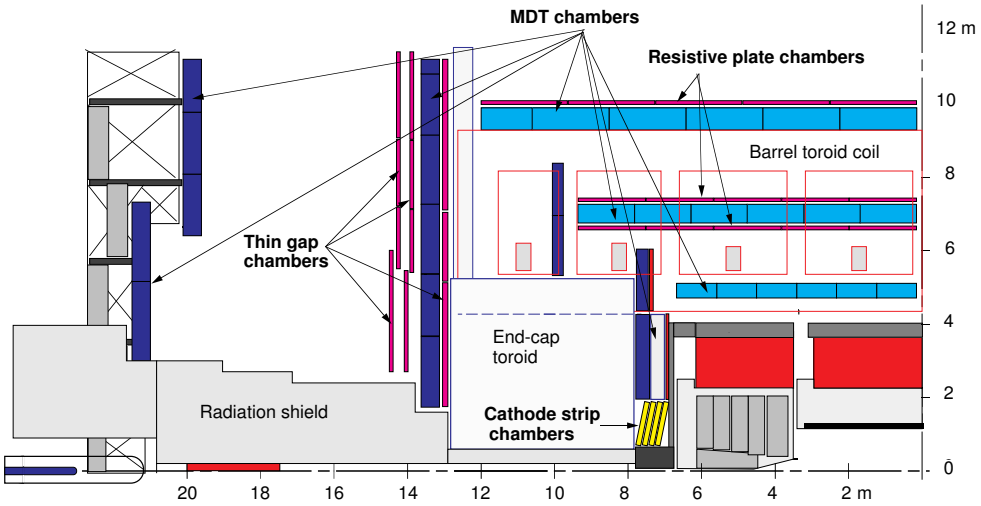

Figure 4.5.: Illustration of one quarter of the Muon Spectrometer. The horizontal axis of the drawing points along the beamline and the interaction point is in the bottom right corner. In the barrel region the detectors are mounted in three rings parallel to the beamline. Monitored Drift Tubes (MDTs) are used for the tracking and Resistive Plate Chambers (RPCs) to obtain fast signals for the trigger. In the end-cap region, the detectors are positioned orthogonally to the beamline on three so-called wheels. Due to the size, the two inner wheels are called Small Wheels (SW) and the outer four wheels are referred to as Big Wheels. Thin Gap Chambers (TGCs) are deployed to get the fast trigger signal in the end-cap region. The precise tracking is mostly provided by the MDTs. On the SW, Cathode Strip Chambers (CSCs) are used at small radii, since the rate of particles exceeds the cababilities of the MDTs. Figure taken from [49].

As the main tracking detector technology, *Monitored Drift Tubes* (MDTs) are deployed both in the end-cap and the barrel regions. The MDTs consist of a stainless steel tube with a radius of 3 cm, filled with gas. A thin wire is fixed in the center of the tube. Muons penetrating the detector ionize the gas in the tube and a voltage applied to the wire leads to a drift of the electrons towards the wire which finally results in a charge avalanche close to the wire that can be detected. The MDT chambers provide a precision of down to 35 μm perpendicular to the wire, but cannot reconstruct the position along the wire. The second technology used for tracking are *Cathode Strip Chambers* (CSCs). Those are multi-wire proportional chambers with a strip-segmented cathode. Since the strips on the two cathodes are rotated by 90° with respect to each other, a reconstruction of two coordinates is possible. The distance between the cathodes of the CSCs is only 5 mm, therefore ions created in the avalanche close to the wire are collected much quicker than in the MDTs,

leading to a higher rate capability of the CSCs compared to the MDTs. For this reason, the CSCs cover the inner region of the SW where the high flux of background particles would exceed the rate capability of the MDTs. For trigger purposes, *Resistive Plate Chambers* (RPCs) stacked on the MDT chambers are used in the barrel region. With a time resolution of about 10 ns the RPCs are able to identify the bunch crossing in which the traversing particle was produced. This is crucial information for the trigger. Additionally the RPCs provide a measurement of the coordinate parallel to the wires of the MDTs. In the end-cap region the fast trigger information is obtained by *Thin Gap Chambers* (TGCs) positioned on top of the MDT detectors. These are also a type of multi-wire proportional chamber, but with an even thinner gas gap than the CSCs. In addition to the fast signal, the TGCs also provide a measurement of the track in the coordinate parallel to the MDT wires. To determine the movement of the muon chambers in ATLAS due to, e.g., thermal expansion of the holding structure, an optical alignment system is in place, achieving a precision of 50 μm. Further information on the MS can be obtained from [49].

4.2.5. Magnets

The momentum of charged particles can be determined by measuring the bending radius of the particle trajectory in a magnetic field. The momentum can be determined as follows:

$$p[\text{GeV}] = 0.3\, q[\text{elementary charge}]\, B[\text{T}]\, R[\text{m}], \tag{4.3}$$

where q is the charge of the particle, B is the strength of the magnetic field, and R is the bending radius. The two quantities dictating the uncertainty of the momentum measurement are the resolution of the measurement of the bending radius, given by the spatial resolution of the detector, as well as the strength and precise knowledge of the magnetic fields. So it is desirable to minimize the spatial resolution of the detector and to maximise the magnetic field strength to reduce the uncertainty on the momentum measurement. The complex magnetic field of the ATLAS detector is created by four large, superconducting magnets namely the central solenoid, the barrel toroid, and the two end-cap toroids. The solenoid provides an axial field around the beam axis in the region of the ID with a strength of 2 T. The barrel toroid consists of eight coils providing a toroidal field of about 0.5 T in the region of the barrel MS. The two end-cap toroids are located between the inner and middle muon end-caps and provide a toroidal field of 1 T. With this magnetic field configuration, ATLAS has a momentum resolution for muons in the order of 10 % at a momentum of 1 TeV. Further details on the magnet system can be found in [33, 50–53].

4.2.6. Data Acquisition System

The *data acquisition system* (DAQ) of ATLAS consists of the configuration and readout of the electronics mounted on the detector, the fast event preselection (called trigger), and the permanent storage of the data of the selected events. In the following the DAQ system is described with a focus on the trigger.

At a luminosity of $2 \cdot 10^{34}/(\mathrm{cm}^2\,\mathrm{s})$, the rate of raw data collected by the ATLAS detector is of the order of 100 PB/s. Since this exceeds by far the capabilities of any available storage technology, ATLAS deploys a two stage trigger system to filter the data stream for scientifically relevant events. In order to make a fast enough decision on keeping or discarding an event, the first level of the trigger system is based on *application-specific integrated circuit*s (ASICs) and *field-programmable gate array*s (FPGAs). Therefore it is also referred to as the *hardware trigger*. The decision of the first trigger level is based on the information from the fast muon detectors (TGCs and RPCs) and fast information from the calorimeters, which have a reduced spatial granularity. The information provided by the MS allows to identify events containing high-momentum muons, while the calorimeter information is used to trigger on other high-momentum particles such as leptons and hadrons. The trigger information from the calorimeter also allows identification of events with so-called *missing energy* carried by particles that do not interact with the detector, e.g. neutrinos or particles not yet known in the SM. The first trigger level receives events at a rate of 40 MHz. The rate of events which pass the selection and are forwarded to the second trigger level, called the *High Level Trigger* (HLT), is 100 kHz. The HLT is fully software-based. It reconstructs event fragments using the full detector granularity in the regions of interest provided by the first trigger level and then makes a trigger decision. The HLT further reduces the event rate to 1.5 kHz which is equivalent to a data rate of 1.5 GB/s. After being accepted by the HLT, the events' *raw data*, i.e. all signals as read out from all channels, is written to disk for permanent storage and offline processing as described in the next section. Further information on the trigger and data acquisition system in general is available in [54–56].

4.2.7. The ATLAS Offline Software

The offline software of ATLAS, called *athena* [57], is the central framework for the simulation and reconstruction of events[3]. Here *offline* refers to the system being executed not during data taking (unlike, e.g., the trigger) but later when the raw data that has been collected by the detector has been stored on disk. Figure 4.6 provides an overview of the different components, also called transformations, of athena which can be split into two categories. The first category is used to simulate events inside ATLAS starting with the modeling of the hard collision of protons followed by the propagation of the final state particles through the detector and finally simulating the detectors themselves together with their readout electronics. The results of the simulation are the signals as they would be read out from the detector in reality. The second category of transformations is used for the reconstruction. It takes either the simulated or real detector signals as input and reconstructs the particle trajectories from it. In the following, the different transformations are briefly introduced, focusing on the implementation of the Muon Spectrometer which is the relevant part for this thesis.

[3] Actually athena includes more functionalities, but since they are not relevant for this thesis they are omitted.

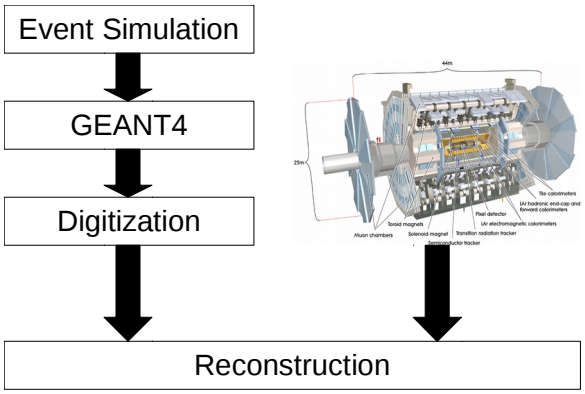

Figure 4.6.: Overview of the various transformations of athena. In the left column the different steps of the event simulation chain are shown. The detector response from the simulated events is then sent to the same reconstruction software as the data from the real detector.

Event Simulation: This transformation takes care of the simulation of the physics processes in the *pp* collisions. It yields the final state particles with their four-momenta. For the studies presented in this thesis, muons are created at the interaction point instead of simulating the full hard collisions.

GEANT4: In this transformation the final state particles from the previous step are propagated through the full ATLAS detector simulation using the GEANT4 simulation toolkit [58]. Thereby the interactions of the particles with the different materials in the detector are modeled. The output is the deposited energy per active detector volume, e.g. per MDT tube. The output format is called *HITS*.

Digitization: This transformation converts the energy deposits into the same format as the actual detector output. First, the processes of signal formation in the detector, i.e. gas ionization, drift, and avalanche, are simulated, then the response of the readout electronics is taken into account. The quantities and the data output are of the same format as delivered by the ATLAS detector. The data format produced by the digitization is called *Raw Data Object* (RDO).

Reconstruction: The reconstruction takes the raw signals from either the detector or the simulation and uses them to reconstruct the trajectories of the particles created in the hard collisions. In the case of the MS, clusters are created from the events in the same layer, if the detector is strip-like segmented. Then, track segments are created within each of the three rings of the barrel and the three wheels of the end-cap and finally the different segments are combined to one track through the full Muon Spectrometer. Afterwards the tracks from the MS are combined with the tracks from the inner detector and the energy deposits in the calorimeter.

Athena uses two different coordinate systems, a global and a local one. The global coordinate system is expressed in either Cartesian or cylindrical coordinates as was already introduced in section 4.2.1. The latter one is used if a position in ATLAS is expressed with respect to the IP. The second coordinate system is the local one. It is used to express a position within a specific detector, e.g. a gas gap of the TGC detectors or a single MDT tube.

5. Upgrade of ATLAS: The New Small Wheel

As described at the end of section 4.1, the LHC is undergoing an intensive upgrade program which aims for an increase in luminosity to 7.5 times the design value of the LHC. In order to cope with the extreme conditions provided by the HL-LHC, the experiments located at the LHC will also need to be improved. The various upgrades of the ATLAS detector are done in two phases. In the first phase [59], taking place in the LS2 at the time of writing this thesis, the major upgrade is the replacement of the muon SW by the so-called *New Small Wheel* (NSW) [60]. Furthermore new detectors are being added to the barrel region of the Muon Spectrometer in order to increase coverage for the trigger and the tracking. Also the electronics of the calorimeter are being renewed. Phase two of the upgrades [61] will take place in the Long Shutdown 3 planned for the years 2025 – 2027. Its major project is the full replacement of the inner tracker. In addition, the readout system of the Muon Spectrometer and the calorimeter will be further improved along with the trigger architecture. New chambers with better rate capabilities will also be added to the MS.
In the following, the NSW project is presented in more detail since it was the main topic of this thesis. First the physics motivation for the NSW is summarized. Then the involved detector technologies are discussed, and finally a description of the structure and the arrangement of the different components is given, which also includes a short overview of the local coordinate system of the NSW used in athena.

5.1. Physics Motivation for the New Small Wheel

The motivation for the replacement of the inner muon end-cap is threefold:

1. Provide additional information from the inner muon end-cap to the first level of the trigger.
2. Maintain excellent tracking performance despite the high rate of background particles expected in the HL-LHC.
3. Sustain an excellent performance while operating in the extreme conditions of the HL-LHC for over 10 years.

In the following sections the trigger and the tracking aspects of the NSW are discussed in more detail.

5.1.1. Trigger Motivation

Figure 5.1a compares the number of L1 muon trigger candidates and the number of muons reconstructed by athena as a function of η. The L1 trigger candidates are built based on the information from the dedicated fast detector technologies while the athena reconstruction uses the information from all detector technologies. The plot shows that for the regions of $|\eta| \geq 1.2$, the end-cap region of the MS, the number of trigger candidates rises dramatically while the number of reconstructed muons with a transverse momentum of more than 10 GeV follows the expected flat distribution. Therefore it can be concluded that most of the muon L1 trigger candidates in the end-cap region are artifacts of the trigger system. They are responsible for up to 90 % of the total muon trigger rate.
In light of the increase in luminosity provided by the HL-LHC and the consequential rise in trigger rate, the high number of false trigger candidates needs to be reduced since it will saturate the bandwidth of the trigger electronics. One way to do so would be to increase the momentum

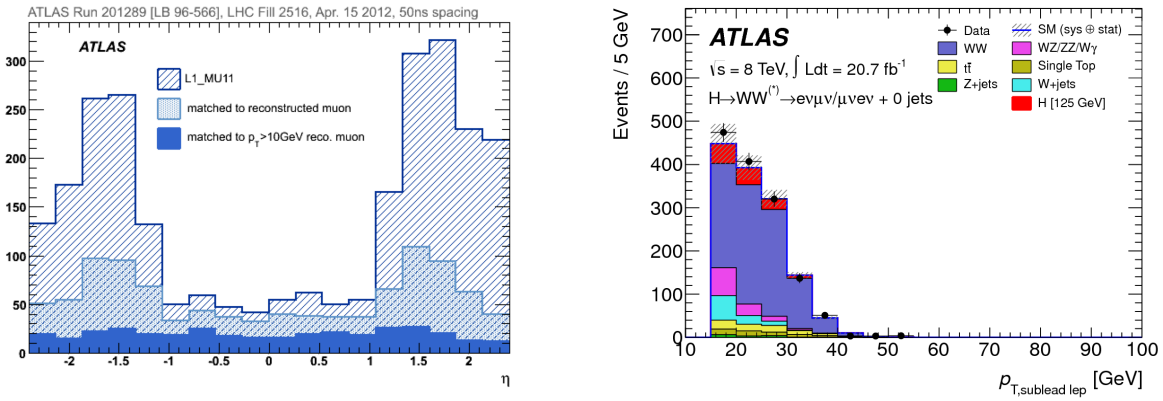

(a) Rate of trigger candidates in the Muon Spectrometer

(b) Impact of an increased p_T threshold in the trigger system

Figure 5.1.: Physics motivation for adding the NSW in the L1 trigger system. **Left:** Comparison of the number of muon trigger candidates (L1_MU11) ($p_T \geq 10$ GeV) and the number of trigger candidates that can be matched to a muon reconstructed by athena using the full detector granularity, as a function of η. Also the number of matched muons with a transverse momentum of more than 10 GeV is shown. It can be seen that in the end-cap region of the Muon Spectrometer ($|\eta| \geq 1.2$) many of the trigger candidates cannot be matched to reconstructed muons since they are artifacts of the trigger system. **Right:** p_T distribution of the sub-leading lepton in events with a $l\nu l\nu$ final state at $\sqrt{s}$ =8 TeV. The contribution of the Higgs decay $H \to WW \to l\nu l\nu$ is shown in red. The plot indicates the loss of sensitivity to relevant physics processes, e.g. here the Higgs decay, if the momentum threshold in the muon L1 trigger would be increased to, e.g., 40 GeV which would be needed to cope with the HL-LHC conditions without the NSW. Both figures taken from [60].

threshold for the L1 muon trigger. But this would imply major drawbacks to the sensitivity in the searches for, e.g., SUSY or for measurements using Higgs decays with leptons in the final state. For example, figure 5.1b shows the p_{T} distribution of the sub-leading lepton in the $H \to WW \to l\nu l\nu$ decay. Increasing the p_{T} threshold for the muon trigger to, e.g., 40 GeV would result in the loss of nearly all signal events.

Figure 5.2 illustrates the origin of the false trigger rate and the intended mitigation with the NSW. In the initial configuration of ATLAS, the muon trigger in the end-cap region is provided by several layers of TGC detectors mounted on the middle one of the three wheels, also called Big Wheel EM[1]. Any particle track passing the TGCs that points towards the IP is taken as a trigger candidate. The false trigger candidates are therefore tracks that pass the TGCs at an angle which points to the interaction point, but where the particle itself is not created at the interaction point. These kind of tracks can be induced by the high flux of background particles like neutrons or low energetic particles created by interactions with the end-cap toroid material or other structural elements of ATLAS in the region between the NSW and the EM wheel. In figure 5.2 the false trigger candidates are indicated with B and C. With the NSW the reconstruction of muon tracks in

[1]EM refers to *End-cap Middle*.

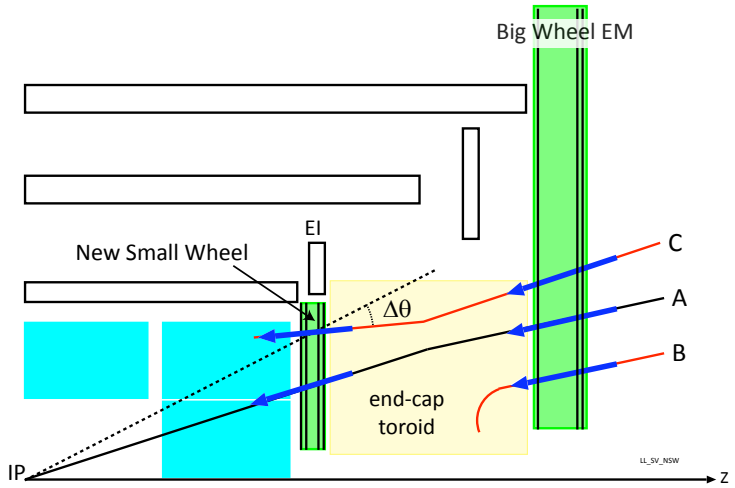

Figure 5.2.: Illustration of the intended improvement of the muon trigger system in the end-cap region by inserting the NSW. Without the NSW, the trigger candidates are only formed based on the angle of the particle tracks passing thought the TGC detectors mounted on the first of the two big wheels. If the angle is compatible with a particle coming from the IP, a trigger candidate is formed. Including the Level 1 trigger information of the NSW improves the track reconstruction at trigger level, rejecting tracks B and C which do not come from the IP, but are induced by background particles like neutrons or particles created by the interaction with the structural elements of ATLAS or the end-cap toroid magnet. Figure taken from [60].

the trigger will be improved by adding another point to the measurement of the particle trajectory, rejecting the fake tracks B and C and only triggering on the genuine muon track A. Therefore it will decrease the rate of false trigger candidates and will allow to maintain the low p_{T} threshold for muons. For the rejection of wrong trigger candidates, the NSW has to provide a real-time track angle resolution of better than 1 mrad.

5.1.2. Tracking Motivation

The current SW uses CSC detectors for the region close to the beamline and a combination of MDT and TGC chambers at large radii, where the MDTs measure the η coordinate and the TGCs provide the ϕ coordinate. Figure 5.3 shows the efficiency of the MDT chambers versus the hit rates in the region of the SW. While the single MDT tubes already show a deteriorated efficiency at the hit rates present with the design LHC luminosity of $1 \cdot 10^{34}/(\mathrm{cm}^2\,\mathrm{s})$, the chambers are still reasonably efficient. For the HL-LHC at least a fivefold higher luminosity, and therefore also a fivefold increased hit rate is expected. This increased rate will lead to an even higher loss of efficiency for the MDT chambers. Since the magnetic field of the end-cap toroid is located in the region between the SW and the first Big Wheel, an inefficiency in the SW means that the muon momentum cannot be reconstructed efficiently, and consequently the combined muon momentum resolution will deteriorate. This has a direct effect on the physics performance of ATLAS as a whole, e.g. in searches for heavy, exotic particles. For this reason, the NSW will use detectors with excellent resolution and high rate capabilities aiming to provide a muon momentum resolution of 10 % at $p_{\mathrm{T}} = 1\,\mathrm{TeV}$.

5.2. Detector Technologies of the NSW

The NSW deploys two detector technologies from the family of gaseous detectors, namely *Micro-Mesh Gaseous Detector* (Micromegas) and *small-strip Thin Gap Chambers* (sTGCs). Both technologies provide excellent trigger and tracking performance in high rate environments. In the following the detector technologies are briefly introduced.

5.2.1. small-strip Thin Gap Chambers

Figure 5.4 shows the schematics of an sTGC detector as it is used in the NSW. It is a multi-wire proportional chamber, consisting of a 1.4 mm thin gas gap filled with a mixture of CO_2 (quenching) and n-pentane (active gas). In the center of the gas gap, wires are installed on which a voltage of 2.8 kV is applied. The electrodes on both ends of the gas gap are segmented into different shapes. On one side, the electrode consists of strips with a pitch of 3.2 mm, providing a spatial resolution of below 50 μm for perpendicular tracks. On the other side pads with a size of several cm^2 are used to provide coarse track information to the Level 1 hardware trigger. Due to their thin gas gap the sTGC detectors can achieve a time resolution below 25 ns. This is why

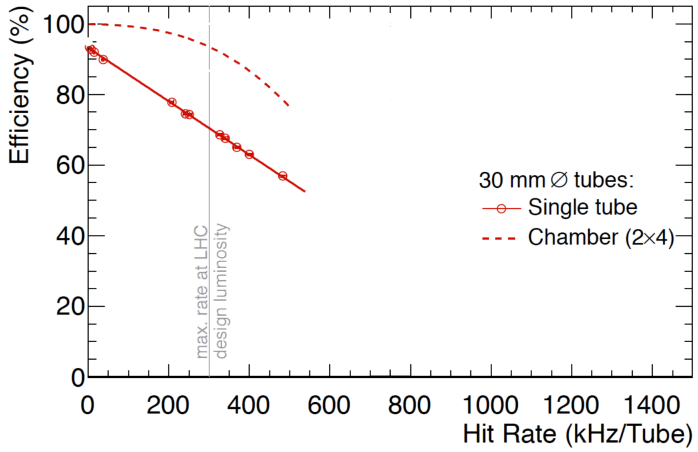

Figure 5.3.: Efficiency of MDT tubes and chambers as a function of the hit rate. At the LHC design luminosity a hit rate of up to 300 kHz/tube is expected at the location of the SW. While the single MDT tubes already lose a significant amount of efficiency at this rate, the full MDT chambers still show efficiencies well above 90 %. But at the fivefold increased luminosities expected in the HL-LHC also the efficiency of the chambers will deteriorate significantly making the MDTs unsuitable for the SW region. Figure taken from [60].

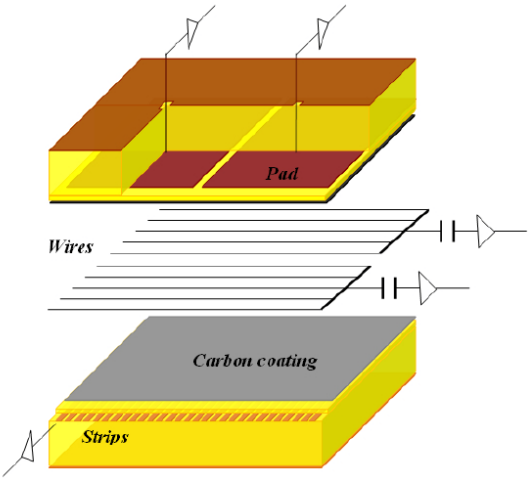

Figure 5.4.: Schematic of an sTGC detector. In the middle of a 1.4 mm wide gas gap, wires are located on which a voltage of 2.8 kV is applied. The two electrodes are segmented into different patterns. One uses a strip pattern to provide high spatial resolutions while the other is segmented into so-called pads, which provide a fast signal for the event selection. Figure taken from [62].

chambers of this type are employed to identify the correct bunch crossing in which the particle traversing the detector have been produced.

5.2.2. Micromegas Detectors

A sketch of a Micromegas detector is given in figure 5.5. The setup consists of a stainless steel mesh in a gas gap, splitting it into two parts. The upper gas gap, called *drift gap*, has a width of 5 mm. Here the muons interact with the gas as discussed in section 3.1 leading to the occurrence of the primary ionizations. Due to an electric field of 600 V/cm applied to the drift gap, the electrons drift towards the mesh. The lower gas gap is only 128 μm thick. A high electric field of about 45 kV/cm is applied to the so-called *amplification gap*, leading to a multiplication of the primary electrons in an avalanche process as described in section 3.3. The anode located at the lower end of the amplification gap is segmented into strips with a pitch of 425 – 450 μm. As protection against sparks in the amplification gap due to the high rate environment, a resistive layer is placed on top of the copper readout strips. The thin amplification gap allows the ions, that were created in the avalanche, to quickly drift to the grounded mesh where they are collected. This yields a small dead time, while the narrow strip pitch leads to an excellent spatial resolution in the order of 100 μm. The Micromegas are operated with a gas mixture of Argon (active) and CO_2 (quenching gas), with a mixing ratio of 93 %:7 %.

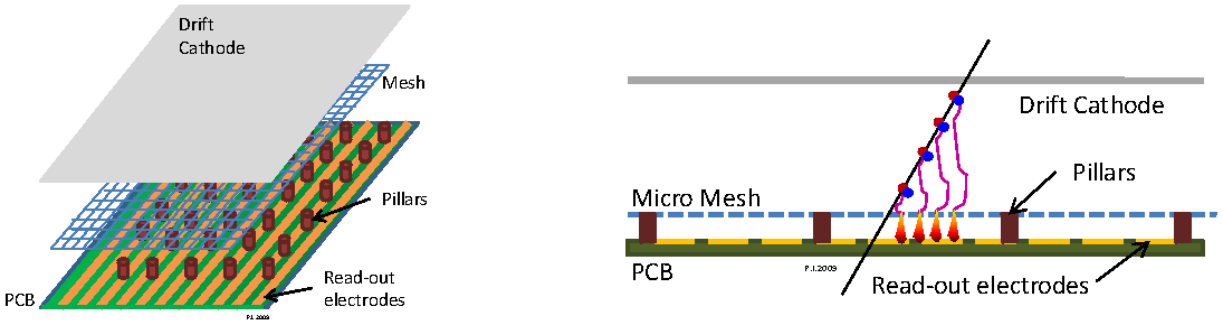

Figure 5.5.: Schematic of a Micromegas detector. The stainless steel mesh separates the gas gap of a Micromegas into two regions of different field strengths, the drift and the amplification field. In the drift region, the charged particle penetrating the detector ionizes the gas molecules along its track, and due to the weak drift field applied between the cathode and the mesh the electrons drift towards the mesh. The amplification field between the readout electrodes and the mesh is much stronger. Therefore the electrons entering this region undergo charge amplification. Finally the electrons created in the avalanche are collected by the strip-like segmented readout electrodes. Figures taken from [60].

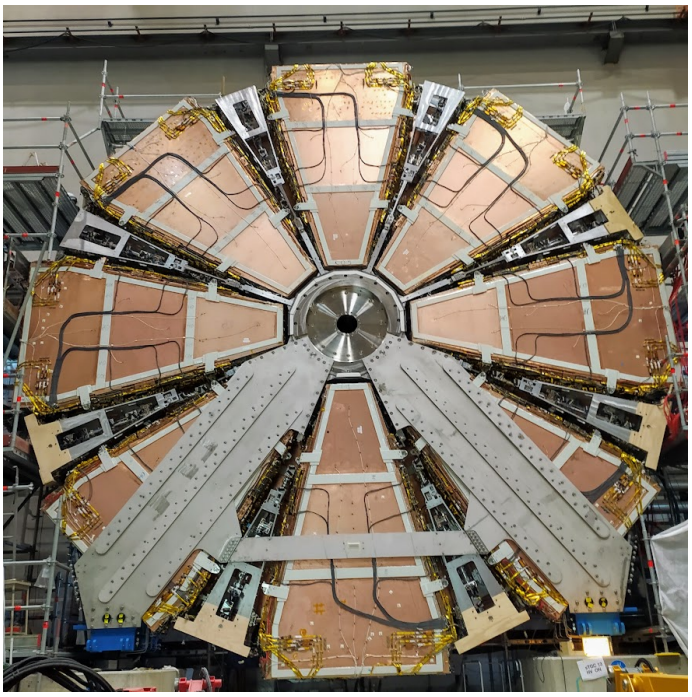

(a) The NSW C during the surface commissioning with all sectors mounted.

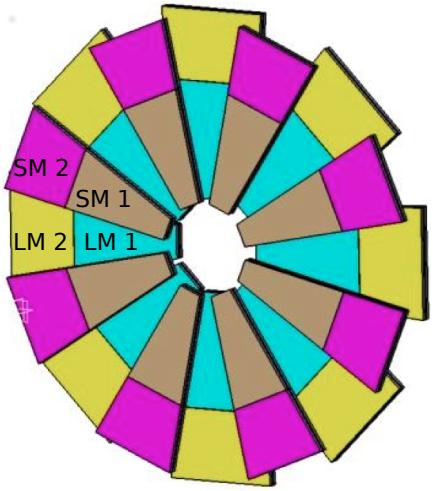

(b) Schematic drawing of the Micromegas sector structure. The NSW consists of 8 large and 8 small sectors which are mounted in two overlapping layers. Figure taken from [63].

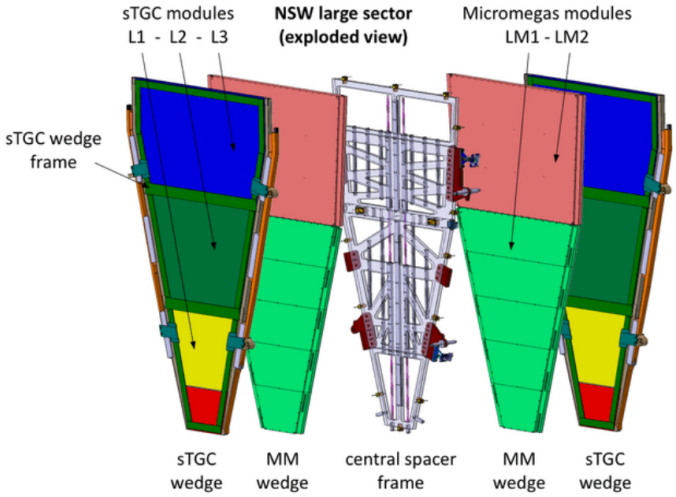

(c) Explosion drawing of a sector. Each sector consists of two wedges of sTGCs which surround two wedges of Micromegas mounted on a spacer frame. The wedges are radially segmented into modules, each containing four layers of the respective detector technology. Figure taken from [64].

Figure 5.6.: Mechanical structure of the NSW.

5.3. Mechanical Structure of the NSW

A picture of one mechanically completed NSW during the surface commissioning is shown in figure 5.6a. In total the NSW consists of sixteen *sectors* that are installed in two layers such that every sector overlaps with two others. This is also illustrated in figure 5.6b. The sectors installed on the layer closer to the IP are slightly smaller than those closer to the HO side, lending them the name *small sector* while the other ones are called *large sectors*. As shown in figure 5.6c, each sector is comprised by four so-called *wedges* stacked parallel to the beamline, each hosting four layers of either Micromegas (inner two wedges) or sTGC detectors (outer two wedges). This leads to a total of 16 detector layers in each NSW sector. The wedges themselves are further segmented along the radial direction into so-called *quadruplets* (also referred to as: *modules* or *chambers*). In the case of the Micromegas, each wedge consists of two quadruplets, where the one at smaller radius is referred to as *Module 1* (M1) and the one at large radius is called *Module 2* (M2). In figure 5.6b the M1s are shown in brown and turquoise depending on the sector size, while the M2s are depicted in pink and yellow. For the sTGCs the wedges are segmented into three quadruplets. The four detector layers in a wedge slightly differ in terms of geometry. For the sTGCs, the geometry of the pads is different to improve the capability to separate tracks for the trigger. For the Micromegas the strips in the four outermost layers are perpendicular to the radial direction, allowing the precise measurement of the η coordinate of a track. Therefore they are referred to as η *layers*. To measure the track position parallel to the strips, the strips of the four inner Micromegas layers are tilted by $\pm 1.5^\circ$ with respect to the ones in the η layers. Those layers are called *stereo layers*.

5.4. Local Coordinate System of the NSW in Athena

As described in section 4.2.1 athena uses a global and a local coordinate system, where the latter one is needed to describe the position within a specific part of the detector. In the following the local coordinate system of the NSW will be introduced. It describes the positions within a gas gap of either an sTGC or a Micromegas chamber. Its origin is located at the center of a quadruplet. The x coordinate is orthogonal to the strips and the y coordinate describes the direction parallel to the strips[2]. The z coordinate follows the direction of the global z coordinate of ATLAS. The origin of the z component for the sTGCs is on the plane of the wires and for the Micromegas in the center of the drift gap. To describe the position of a gas gap, the variables listed in table 5.1 are used. They follow the mechanical structure of the NSW given above.

[2]This is different for the sTGC strips and pads, but those are not relevant for this thesis.

Name	**Range**	**Description**
stationName	MML, MMS STL, STS	MM/ST: Micromegas or sTGC L/S: large or small sector
stationEta	$\pm(1-3)$ (sTGC) $\pm(1-2)$ (MM)	sign: side A (positive) or C (negative) absolute value: quadruplet in radial direction
stationPhi	$1-8$	indicates sector number in polar direction one phi station includes a large and a small sector
multiplet	$1-2$	wedge number in z-direction
gas gap	$1-4$	gas gap number within a wedge in z-direction

Table 5.1.: Variables describing the NSW structure inside athena.

6. Micromegas Detectors

Micromegas were introduced in 1996 by Y. Giomataris et al. [65]. With their micro-pattern-structured readout electrode they provide very precise tracking while having an excellent rate capability due to a thin amplification gap. The Micromegas technology is well established and different types are deployed in a variety of experiments, e.g. COMPASS [66]. While all Micromegas used in experiments so far are small in size ($\leq 1\,\mathrm{m}^2$) the Micromegas on the NSW have a surface of more than $2\,\mathrm{m}^2$ per quadruplet covering a total active area of $1280\,\mathrm{m}^2$ in multiple layers.
In the following the basic concept of Micromegas detectors is introduced. The main emphasis is put on the implementation as used in the NSW. Afterwards different methods for the position reconstruction of particle tracks with Micromegas are discussed focusing on the reconstruction of inclined tracks where the drift time of the electrons in the drift gap needs to be taken into account.

6.1. Setup of Micromegas Detectors

Figure 6.1 shows a sketch of a Micromegas detector. It consists of a gas volume surrounded by the drift cathode at the top and the strip-segmented readout anode at the bottom. Furthermore there is a stainless steel mesh separating the gas gap into two regions where electrical fields of different strenghts are applied, the drift and the amplification region. In the following the main components are discussed in detail.

Drift Cathode In the type of Micromegas deployed in the NSW, the drift cathode is implemented as a copper plate spanning the full surface of a quadruplet. A negative voltage of 300 V is applied on the cathode, creating an electric field of 600 V/cm between the cathode and the stainless steel mesh, which are 5 mm apart from each other. This electric field is referred to as drift field, the region between the cathode and the mesh is called drift gap accordingly. The incoming charged particle transverses the drift gap and ionizes the gas along its path as discussed in section 3.1. The electrons created in these processes follow the drift field lines and drift through the gas towards the mesh, which was described in section 3.2.

Stainless Steel Mesh The mesh is held on ground potential and therefore divides the gas gap into two regions of different electric field strengths, the drift and the amplification field. The mesh itself is woven out of stainless steel wires with a diameter of $30\,\mu$m and a pitch of $71\,\mu$m. The distance between the mesh and the readout electrode is $128\,\mu$m. To guarantee this tiny distance

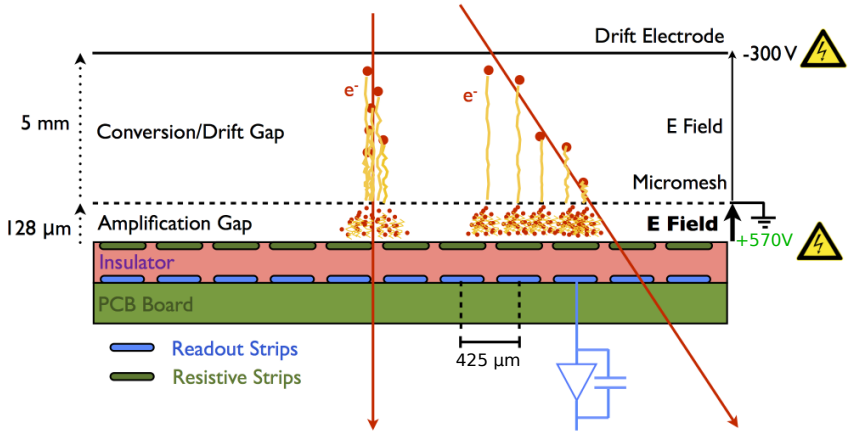

Figure 6.1.: Sketch of a Micromegas detector. It consists of a gas gap surrounded by a drift anode and a micro-pattern electrode. A stainless steel mesh divides the gas gap into two zones with different field strengths. Figure taken from [67].

over a surface of more than $2\,\mathrm{m}^2$, the mesh is mounted into the detector with a certain tension. Furthermore there are pillars, made out of so-called *photo imageable coverlay*, positioned on the readout electrode supporting the mesh and keeping its distance to the readout strips with a very good precision.

Readout Anode The readout anode of the Micromegas is segmented into strips with a pitch of $425-450\,\mu\mathrm{m}$ depending on whether they are part of a large or a small sized quadruplet. This geometry guarantees a good spatial resolution. The anode consists of two layers of strips: the upper layer formed by the so-called *resistive strips* made out of carbon and right underneath, separated by a layer of kapton, *copper strips* are located. The strips have a width of $300\,\mu\mathrm{m}$ and the gap between them is $125-150\,\mu\mathrm{m}$. A positive voltage of 570 V is applied on the resistive strips, creating an electric field of $45\,\mathrm{kV/cm}$ between the strips and the mesh. This strong field leads to gas avalanche as discussed in section 3.3. The choice for resistive strips was made in order to protect the detector against sparks which harm the material and also create dead time. In case a spark occurs, the induced current flowing through the resistive strips reduces the amplification field and stops the avalanche, thus suppressing the creation of further sparks. While the copper strips cover the full width of the detector, the resistive strips contain a very thin gap in the center of the chamber, dividing it into two high voltage sections. The actual charge readout of the chamber is done through the copper strips, which receive the signal via capacitive coupling to the resistive strips. Given the small strip pitch and the capacitive coupling between neighboring resistive and copper strips, part of the signal on a copper strip is induced by neighboring resistive strips (see figure 10.5). This effect is called *charge sharing* (CS) and has a significant impact on the performance of the detector as will be shown later. The charge on the copper strip gets read out, amplified, and digitized by the so-called *VMM* ASIC, which is discussed in section 7.2.

6.2. Operating Gas

Micromegas detectors are operated with a variety of gas mixtures depending on the field they are deployed in. In the NSW a gas mixture of Argon and CO_2 with a ratio of 93:7 will be used, where Argon guarantees a high number of ionizations and CO_2 acts as the quenching gas. In the following, the properties of this gas mixture are discussed, focusing on their impact on the detector performance.

6.2.1. Drift properties

For the motion of the electrons in the drift gap, the key parameters of the gas mixture are the drift velocity of the electrons and the diffusion in longitudinal and transverse directions. Figure 6.2a shows the drift velocity of the electrons in the drift gap as a function of the electric field. At the value of the drift field of 600 V/cm the drift velocity is 47 μm/ns. At this field strength the drift velocity is rather stable such that it does not depend too much on the field strength. This is important because then the drift distance, used in the reconstruction of the particle trajectories passing through the detector, is obtained linearly from the drift time and velocity. A variation of the drift velocity therefore has a direct impact on the spatial resolution of the detector. The drift velocity corresponding to the chosen field strength is such that all electrons created in the drift gap reach the mesh within 105 ns which is well below the readout window of the front-end electronics of 200 ns. At this field strength the transverse (longitudinal) diffusion of electrons with a drift distance of 1 cm is 365 μm (198 μm). The drift properties were determined using the software *PyBoltz* [68].

6.2.2. Amplification Properties

Figure 6.2b shows the distribution of the number of electrons produced in the avalanche of a single electron in the amplification gap, referred to as *gas gain*. It is described by the Polya function defined in equation 3.17. Initially the plan was to operate the Micromegas detectors with 600 V applied on the resistive strips, leading to a field strength of about 47 kV/cm. This corresponds to an average gas gain of 10^4, as it is shown in the aforementioned figure. Due to voltage instabilities, the working point of the Micromegas had to be reduced to 570 V. This corresponds to a gas gain of about 8000, which is still sufficient to yield a good overall detector performance.

6.3. Position Reconstruction with Micromegas Detectors

For the reconstruction of clusters of coincident signals on copper strips (see below), referred to as *clusterization*, and their positions with a Micromegas detector there are different methods available, the applicability of which mainly depends on the incident angle of the track and the time resolution of the detector. The performance of an individual cluster reconstruction method

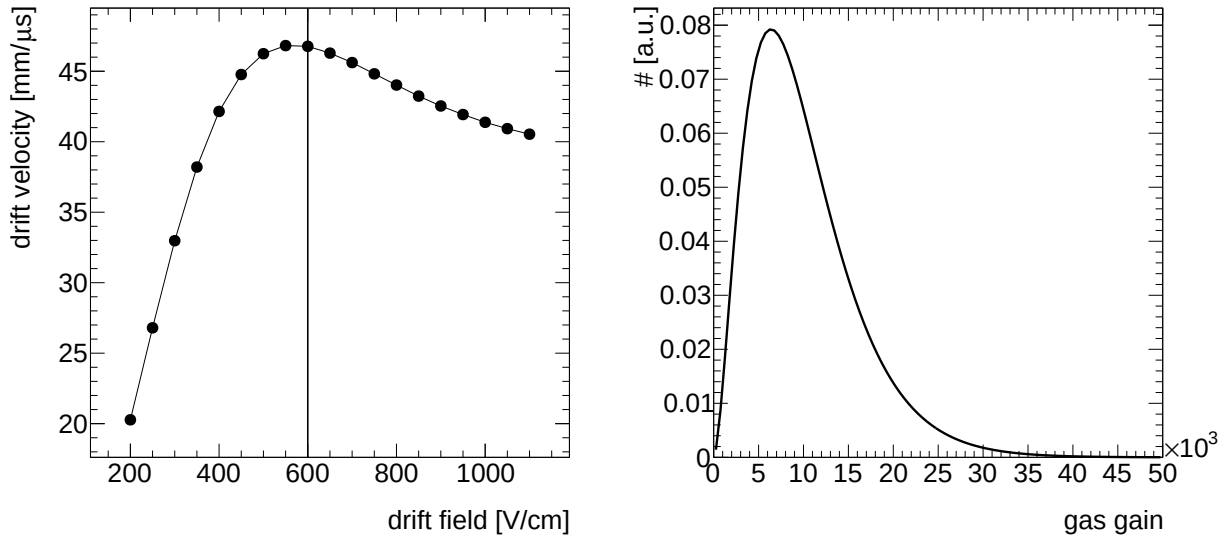

(a) Drift velocity of electrons in a gas mixture of Argon-CO_2 (93:7) as a function of the electric field.

(b) Polya distribution describing the gas gain in gaseous detectors.

Figure 6.2.: Properties of the Argon:CO_2 (93:7) gas mixture used in the Micromegas detectors of the NSW.

is assessed by two quantities: the *position resolution*, which describes the precision of the reconstructed cluster location per Micromegas layer, and the *reconstruction efficiency*, which is a measure for the probability of a clusterization method to correctly build a cluster for a genuine particle track for each layer.

For tracks perpendicular to the strip plane, the computation of the particle position from the charge-weighted mean position of strips whose signal exceeds the threshold (*centroid method*) performs very well. But in ATLAS, tracks with an inclination of $7-31°$ with respect to the beamline are expected from the geometry of the NSW, leading to a loss of precision for the centroid method. Hence for inclined tracks, more sophisticated methods are needed, taking into account the time of arrival of the charge on each strip. Using the drift time information turns the drift gap into a *micro Time Projection Chamber* (μTPC), which also gives the name to the most prominent reconstruction method. In order to further optimize the position resolution and the reconstruction efficiency, two methods have been studied which employ the additional information of an external estimate of the track angle. One way to obtain this estimate is to perform a fit of a track through several detector layers. However, this requires a first round of position reconstruction with either the centroid or the μTPC method without the external angle estimate. The information of the external angle estimate is exploited differently in the two methods. The first approach uses it together with the charge-weighted mean time of the strips to project the position calculated by the centroid method to the center of the drift gap. It is

Method / Input Parameters	Strip Position	Charge	Drift Time	Ext. Angle Estimate
centroid	yes	yes	no	no
CTP	yes	yes	yes	yes, as fixed value
μTPC	yes	no	yes	no
constrained μTPC	yes	no	yes	yes, as constraint

Table 6.1.: Position reconstruction methods for Micromegas detectors and their input parameters.

called the *Cluster Time Projection* (CTP) method and was first introduced in [69]. In the second method the recipe of the μTPC clusterization is deployed, but the angle in the fit is constrained towards the estimate. Therefore it is called the *constrained μTPC* method and was developed in the scope of this thesis. The different methods and their input variables are summarized in table 6.1.
In the following the different clusterization methods are discussed in detail. All of them consist of two major steps. The first is to group strips whose signal has exceeded the threshold into so-called *clusters*, where a cluster contains all strips that received charge from the same particle passing through the detector. In a second step the positions of the clusters are computed using the information discussed above. The position of each cluster is expressed in a two dimensional coordinate system, where the x-axis is orthogonal to the strips and the z-axis is antiparallel to the drift direction (see section 5.4). By construction, the methods mentioned above place the clusters at a z-value equal to the half of the maximal drift distance, referred to as the center of the drift gap. The x-value of the position is called the *precision coordinate* and all the studies presented in the following express the position resolution in the direction of this coordinate.
The NSW performance goals discussed in section 5.1, i.e. a momentum resolution of 10 % at $p_{\mathrm{T}} = 1\,\mathrm{TeV}$ and a good reconstruction efficiency at high particle rates, translate into the requirements on the clusterization algorithms to provide a position resolution in the order of $100\,\mu$m and a reconstruction efficiency of 90 % or above.

6.3.1. Centroid Method

For perpendicular tracks the reconstruction with the centroid method is already sufficient to reach a spatial resolution of better than $100\,\mu$m. The clusterization of the strips is done by merging neighboring strips, which have a signal above a certain threshold set in the VMM, into a cluster. If multiple groups of adjacent strips exceed the threshold, multiple clusters are reconstructed.
Since the noise level is non-negligible for the large quadruplets due to the long copper strips, gaps of one missing strip are allowed in centroid clusters to account for strips not exceeding the threshold. For inclined tracks, the centroid method loses its precision due to several reasons. The main one is that the initial ionizations do not occur at the same precision coordinate anymore but along the inclined track. Given the production of different amounts of charge on the strips caused by variations in the primary and secondary ionizations and the avalanche of the charge, the reconstructed position is skewed towards those ionizations that produce more charge. This

effect can be mitigated by including the drift time into the calculation of the cluster position as is discussed below.

6.3.2. Cluster Time Projection Method

As discussed above the centroid clusterization loses its precision for inclined tracks due to fluctuations in the primary and secondary ionization and in the avalanche process. To overcome this issue, the CTP method corrects the centroid position with the drift time measurement and an external estimate of the incident angle. The goal of this correction is to project the cluster to the vertical center of the drift gap. An illustration of the CTP method is given in figure 6.3. As a first step the position obtained with the centroid method and the mean drift distance obtained from the mean time of the strips weighted by their charge ("charge-weighted mean time") are calculated as follows:

$$\bar{x} = \sum_i q_i \, x_i \quad \text{and} \tag{6.1}$$

$$\bar{d} = \sum_i q_i \, t_i \, v_D = \sum_i q_i \, d_i, \tag{6.2}$$

where v_D is the drift velocity, x_i the individual strip position, and t_i the time measurement of the strip. Here, the index i enumerates the strips. Neglecting the uncertainty on the charge

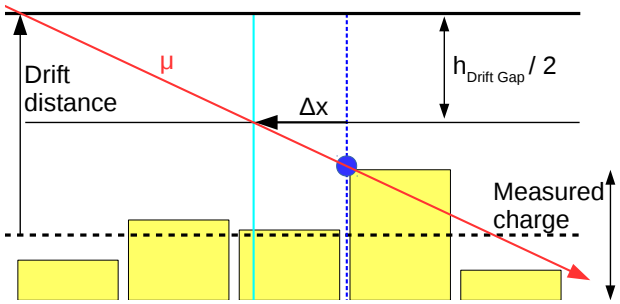

Figure 6.3.: Illustration of the working principle of the Cluster Time Projection method. The dashed blue line indicates the position of the cluster calculated by the centroid method, while the blue dot also includes the information of the mean time of the strips weighted by their charge. Compared to the particle position at the center of the drift gap ($h_{\text{Drift gap}}/2$), the centroid position is skewed to the right. Using an external estimate for the inclination of the track and the information from the drift time, the cluster position can be corrected by Δx to the left in order for the cluster to be at half the height of the drift gap, where any fit combining different layers would expect it. The projected position is indicated by the solid turquoise line.

measurement, the errors of the positions and the drift distances are given by:

$$\sigma_{\bar{x}} = \sqrt{\sum_i (\sigma_{x_i}\, q_i)^2} \quad \text{and} \tag{6.3}$$

$$\sigma_{\bar{d}} = \sqrt{\sum_i (\sigma_{d_i}\, q_i)^2}. \tag{6.4}$$

The uncertainty on the drift distances and the strip positions is computed from the transverse and longitudinal diffusions, σ_{Trans} and σ_{Long}, the pitch of the strips and an uncertainty on the ionization time σ_{Ion}, respectively. They are computed with the following formulae taken from [70]:

$$\sigma_{x_i} = \sqrt{\left(\frac{\text{pitch}}{\sqrt{12}}\right)^2 + (\sigma_{\text{Trans}}\, d_i)^2} \quad \text{and} \tag{6.5}$$

$$\sigma_{d_i} = \sqrt{(\sigma_{\text{Ion}}\, v_D)^2 + (\sigma_{\text{Long}}\, d_i)^2}. \tag{6.6}$$

Using the centroid position, the mean value in time and the knowledge of the incident angle of the track θ, the cluster can now be projected towards the center of the gap as following:

$$x_{\text{proj}} = \bar{x} - \left(\bar{d} - \frac{h_{\text{drift}}}{2}\right) \tan(\theta), \tag{6.7}$$

where h_{drift} is the height of the drift gap. The uncertainty on the projected position is given by:

$$\sigma_{x_{\text{proj}}} = \sqrt{\sigma_{\bar{x}}^2 + (\sigma_{\bar{d}} \tan(\theta))^2}. \tag{6.8}$$

6.3.3. Micro Time Projection Chamber Method

The μTPC method [71, 72] aims to not only measure the cluster position at the center of the gas gap, but also the incident angle. Therefore it can be used without having an external estimate of the angle. The algorithm consists of three major steps:

- coarse clustering of neighboring strips, allowing up to three consecutive missing strips,
- application of a *Hough transform* (HT) [73, 74] to filter strips that belong to a straight line through the drift gap, and
- fitting a straight line to the strips passing the filter and extracting the cluster position at the center of the drift gap.

The first step is only relevant in ATLAS, where many unrelated hits are expected due to background events. It serves as a first coarse filter to minimize the CPU time spent in the HT and to avoid disruptions from unreasonable line segments.

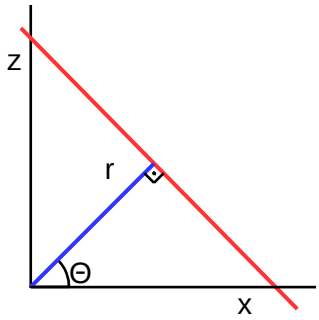

Figure 6.4.: Representation of a line in the Hesse normal form. Here the red line is expressed by θ and r rather then slope and intercept. This has the advantage that for any rotation of the line, the θ-value changes linearly while the slope would diverge for vertical lines. Drawing follows [75].

In the HT a line is expressed in the Hesse normal form as illustrated in figure 6.4. In this form a line is described by the angle θ and the radius r rather than the slope and the intercept. This has a few advantages, the main one being that a rotation of the line leads to a linear change of θ for any orientation while the slope diverges for vertical lines. Therefore this form is ideal for the use in the HT. For a given value of θ the radius can be determined as follows:

$$r = x\cos(\theta) + z\sin(\theta). \tag{6.9}$$

In the case of the Micromegas, x denotes the strip position and z the drift distance. In the HT for each strip above threshold in a given layer, the radius r is calculated for a range of θ values and the (r,θ)-pairs are filled into a histogram called the *accumulator*. Figure 6.5 shows a typical μTPC event from the Micromegas simulation and its corresponding accumulator. In the accumulator, the (r,θ)-pairs for each strip are visible as a line. These intersect, leading to bins with elevated numbers of entries (yellow in figure 6.5a). The (r,θ)-values corresponding to the bin with the highest number of entries are chosen to define the line corresponding to the expected particle trajectory through the gas gap. If the highest bin is below a certain threshold, e.g. 3, the HT is declared non-successful and the clusterization for the particular gas gap is stopped. This excludes cases where a line is made up by two strips, which are on a line by definition. Using the (r,θ) of the highest bin one can compute the χ^2 of all points with respect to the line that one has obtained. If more than one bin have the same maximum number of entries, the estimate leading to the line with the smallest χ^2 is chosen. Strips whose position deviates from the median residuals of all points to the line by more than 1 mm are excluded from the cluster. The median of the residuals is taken to account for extrapolation uncertainties due to the bin sizes of the accumulator. It is also used for the computation of the χ^2 discussed above. If at least three excluded points are present, the clusterization is repeated for those, which can lead to more than one cluster per gas gap if the repeated HT was successful. The HT is a standard method in the

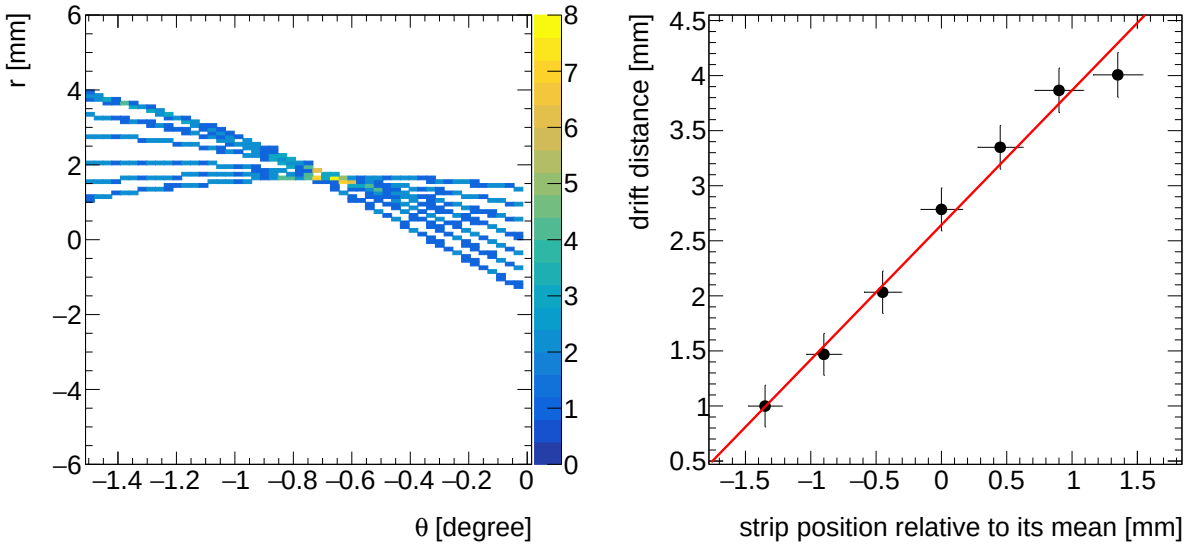

(a) Accumulator of the HT

(b) Fit of the μTPC line segment

Figure 6.5.: Depiction of the μTPC clustering method for one gas gap in an exemplary event. **Left:** Accumulator of the HT used to determine the best value for the angle and radius of a line segment in a gas gap. For each strip exceeding the threshold, r is calculated for multiple angles according to equation 6.9. Each of the (r, θ) pairs is put into the accumulator and the bin with the most entries then gives the estimate for the angle and the radius. **Right:** After the strips belonging to the estimated line have been selected, a linear fit is performed and the cluster position is extracted at the center of the gas gap.

field of pattern recognition in pictures.

For each line identified by the HT the corresponding hits are fitted using the uncertainties on the strip position and the drift time described in the equations 6.5 and 6.6 respectively (see figure 6.5b). The cluster position is then determined at the intersection of the fitted line and the center of the gas gap. The uncertainties on the cluster position are taken from the propagation of the errors on the fit parameters.

6.3.4. μTPC with a Constrained Angle

This method follows the concept of the μTPC one, but rather than reconstructing the angle of the particle passing the detector, an external estimate of θ and its uncertainty σ_θ is used as a seed in the cluster finding procedure and as a constraint in the final fit. The procedure for the clusterization of the strips before the final fit is illustrated in figure 6.6. Instead of having to implement the entire HT as for the unconstrained μTPC method in the previous section, only the intersect needs to be estimated. For this, first the strip positions are recalculated to be centered

around their mean value. Afterwards the points are located on a line which crosses the center of the drift gap at the mean strip position, e.g. the point (0,2.5) in figure 6.6. The slope of the line is given by the angle estimate. A corridor is opened by two lines with slopes of $(-\operatorname{atan}(\theta \pm \sigma_\theta))^{-1}$ also intersecting at the point (0,2.5), and the points which are inside the corridor within three times their uncertainty pass the filtering. This procedure is repeated by varying the z value of the intersection point to account for offsets in timing. The z value with the most hits passing the filter is chosen and the associated hits are assigned to the cluster. Like for the μTPC method this procedure is repeated for strips not passing the filter if there are more than three of them. The position of the cluster is determined by a fit of the associated hits, where the main difference compared to the μTPC method is that a constraint is applied on the angle in the fit. In order to fit a line with a constraint on the angle, the log-likelihood method is deployed, which essentially

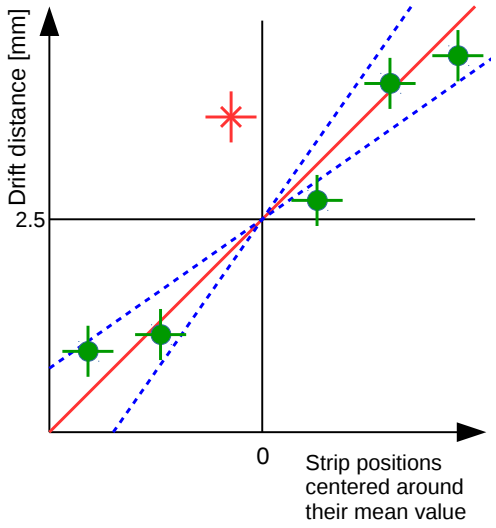

Figure 6.6.: Illustration of the strip selection in the constrained μTPC method. Since the strip positions are centered around their mean value, the pairs of strip position and drift times ideally lay on a line which intersects the center of the drift gap at the mean strip position. In the plot this would correspond to the point (0,2.5). The slope of the line is given by the external estimate of the angle (solid red line). In order to find the points belonging to a cluster, a corridor is opened by varying the slope by $\pm\sigma_\theta$, which is the uncertainty on the angle estimate (blue dashed lines). Points which are inside the corridor within three times their uncertainty are accepted for the cluster (green circles), while those outside are excluded (red stars). To account for variations of the timing, the corridor is moved up and down by changing the z coordinate of the intersection point of the dashed blue lines in steps of 0.1 mm. The intercept with the most associated hits is selected.

minimizes the following term:

$$\mathcal{L}(\theta, c) = \left(\sum_i \frac{(-\frac{1}{\operatorname{atan}\theta} x_i + c - z_i)^2}{\sigma_{z,i}^2 + \sigma_{x,i}^2 \left(-\frac{1}{\operatorname{atan}\theta}\right)^2} \right) + 0.5 \left(\frac{(\theta - \theta_0)^2}{\sigma_\theta^2} \right), \tag{6.10}$$

where the first part represents the residuals between the fitted points (x_i, z_i) and the predicted line and the second term adds a constraint on the angle θ. The strength of the constraint is given by the uncertainty of the estimate, σ_θ. Finally the cluster position is extracted by evaluating the fit at the center of the gas gap. The uncertainty on the cluster position follows from the propagation of the errors of the fit parameters.

Part II.

Micromegas Performance in the Test Beam

In the summer of 2018 a test beam campaign with one of the first Micromegas production modules took place in the CERN north area. It was the first time that the front-end chip used in the NSW, namely the pre-final version VMM3, was deployed on a full-size Micromegas quadruplet. Therefore the test beam had two major goals: first validate that the VMM readout chip works on a full-size module and, second, study the performance of the detector. For the latter, the most important aspect is the spatial resolution for tracks under an angle, since for the NSW only inclined tracks are expected.

This part consists of three chapters. In the first, the setup of the test beam is described followed by a disussion of the readout electronics. Focus is put on the individual calibration of over 2000 VMM channels deployed in the test beam setup, which was carried out in the scope of this thesis. This calibration is required for the later analysis of the data but also the data taking itself. In the second chapter, the performance of the different position reconstruction methods as measured in the experimental setup is discussed, focusing on the methods used for inclined tracks. Finally chapter 9 summarizes the studies conducted.

7. Setup and Calibration

This chapter first introduces the experimental setup of the test beam, which includes the mechanical setup followed by a description of the readout electronics. Then the procedure of calibrating the over 2000 electronics channels is discussed, to which significant contributions have been made. Two categories of calibrations need to be performed: first, the noise of each VMM channel is measured and a threshold is applied according to the noise. This type of calibration needs to be applied to the readout chip before data taking. Second, the *analog-to-digital converter* (ADC) counts associated to charge and time measurements are calibrated in order to correctly convert them to physical units, used in the data analysis. Both types of calibration are discussed in this chapter in terms of procedure, results, and their impact on the detector performance.

7.1. Mechanical Setup

Figure 7.1 shows the setup used in the test beam. The *device under test* (DUT) was the first SM2 quadruplet from the series production, built by a consortium of German universities lead by the University of Munich. For the external tracking, three Micromegas prototypes with a size of 10 cm×10 cm have been deployed. Two of those tracking chambers were mounted downstream of the SM2 quadruplet and one upstream of it. For the trigger two equal-sized scintillators with a size of 10 cm×10 cm were attached to the two downstream tracking chambers. For the readout, the pre-final version of the chip used in the NSW, namely the VMM3, was connected to the DUT. The full setup was located at the north area of CERN in the H8 beamline. In the following more details on the beamline and the DUT are given.

7.1.1. The H8 Beamline

The H8 beamline is located in the north area of CERN. It is part of a complex of several beamlines which are all connected to the SPS. It can either carry the proton beam directly from the SPS or secondary beams consisting of hadrons or electrons. The secondary beam is generated by colliding the primary SPS beam with a beryllium target and then selecting the desired secondary beam via a dedicated system of magnets. For the studies discussed in this thesis, a secondary pion beam was used. It had positive polarity, a momentum of 180 GeV, and a rate of several kHz. The beam diameter is in the order of several cm.

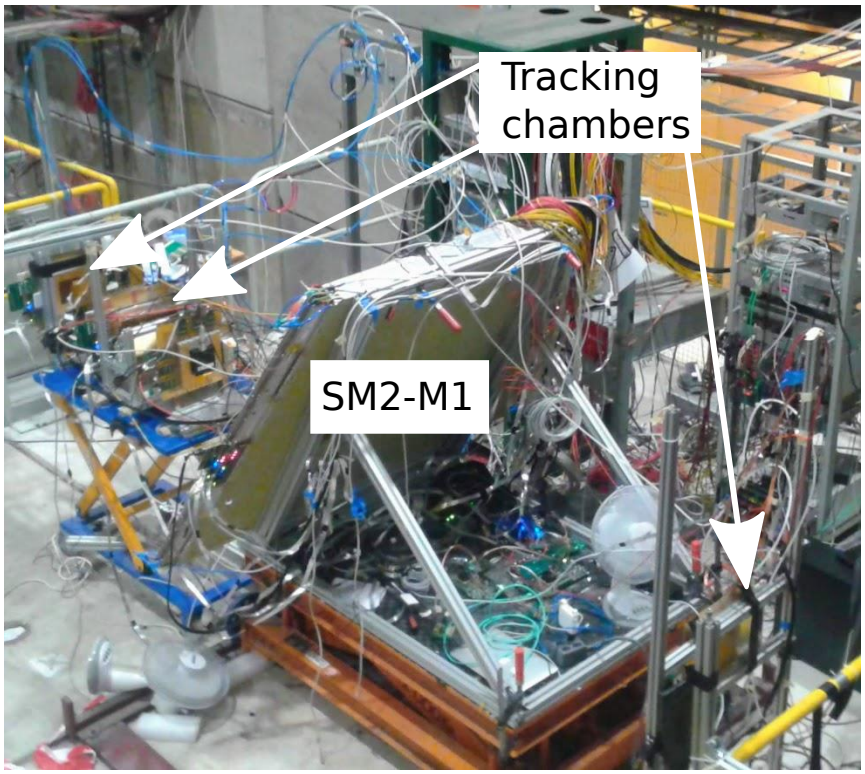

(a) Picture of the test beam setup.

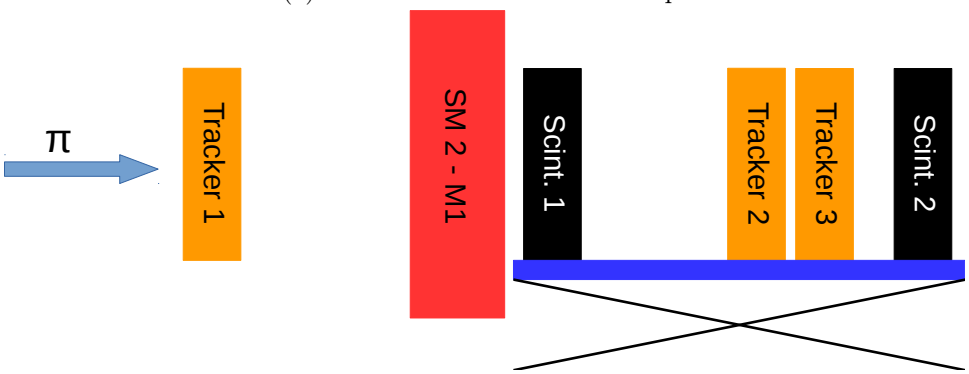

(b) Sketch of the relevant parts of test beam setup.

Figure 7.1.: Picture and sketch of the test beam setup. The setup consisted of the first series production module of the SM2 type, which is visible in the center of the photograph. In the direction of the beam, one small Micromegas prototype detector was placed 208.5 cm in front of the SM2 module (bottom right in the picture) and two small Micromegas were placed 78.6 cm and 83.4 cm behind the SM2 module, respectively. Those three small detectors are used to determine the reference track through the SM2 module. The trigger is realized using two scintillators, one behind the SM2 module and one behind the tracking detectors.

7.1.2. SM2 Chamber under Test

The SM2 quadruplet has a width of 1.7 m, is 1.2 m long and consists of four layers of Micromegas detectors. Each layer is segmented into three *printed circuit board*s (PCBs), hosting two *high voltage* (HV) sections each denoted with L and R, as shown in figure 7.2. Due to HV instabilities of the chamber, mostly the bottom right HV section was studied, referred to as HV section 8R, but a few runs were also taken with the central PCB 7, referring to HV sections 7L and 7R, positioned in the beam.

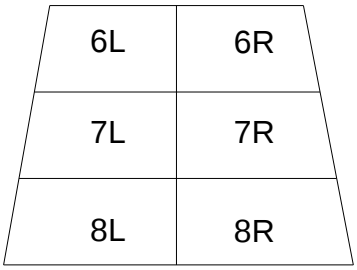

Figure 7.2.: High voltage sections of one layer of the SM2 chamber. Due to high voltage instabilities in the other sections, mostly the section 8R was used in the studies.

7.2. Readout Electronics

The readout of the DUT and the tracking detectors was realized with the VMM3 front-end chip [76, 77]. The VMM3 is the pre-final version of the VMM3a eventually used in the NSW. A sketch of the VMM is given in figure 7.3. The chip houses 64 readout channels. Each channel has an individual shaping amplifier which was operated with a gain of 9 mV/fC and a so-called *peaking time* of 100 ns and 200 ns. Behind the amplifier, each channel has a discriminator. The discriminator is controlled by two values, one DAC value which is common for all channels of the chip and the so-called *channel trimmer* which can change the individual channel threshold in a small range on top of the global value. This is used to correct for individual channel responses to the global DAC value. In the VMM3 these trimmers are not functional[1]. Therefore there was only the possibility to set a global threshold per VMM and no way to make the individual channel thresholds equal. After the amplification stage follows the digital part of the VMM. ADCs of different resolutions and processing times are available to digitize the pulse amplitude. The time measurement is given by two values, a coarse one which associates the peak to a counter driven by an external clock, and a fine one, a *time-to-amplitude converter* (TAC), which yields the time between the peak and its associated clock cycle. Apart from the time at the peak, also the time at the threshold can be measured with the same mechanism. For the recovery of signals below

[1] This was one of the reasons to invent the VMM3a, but at the time of the test beam not enough VMM3a chips were available.

the threshold, the VMM has a so-called *neighbor logic* (NL). With the NL enabled, the VMM also reads the two neighboring channels adjacent to a strip above threshold independently of whether or not they have signals above threshold.

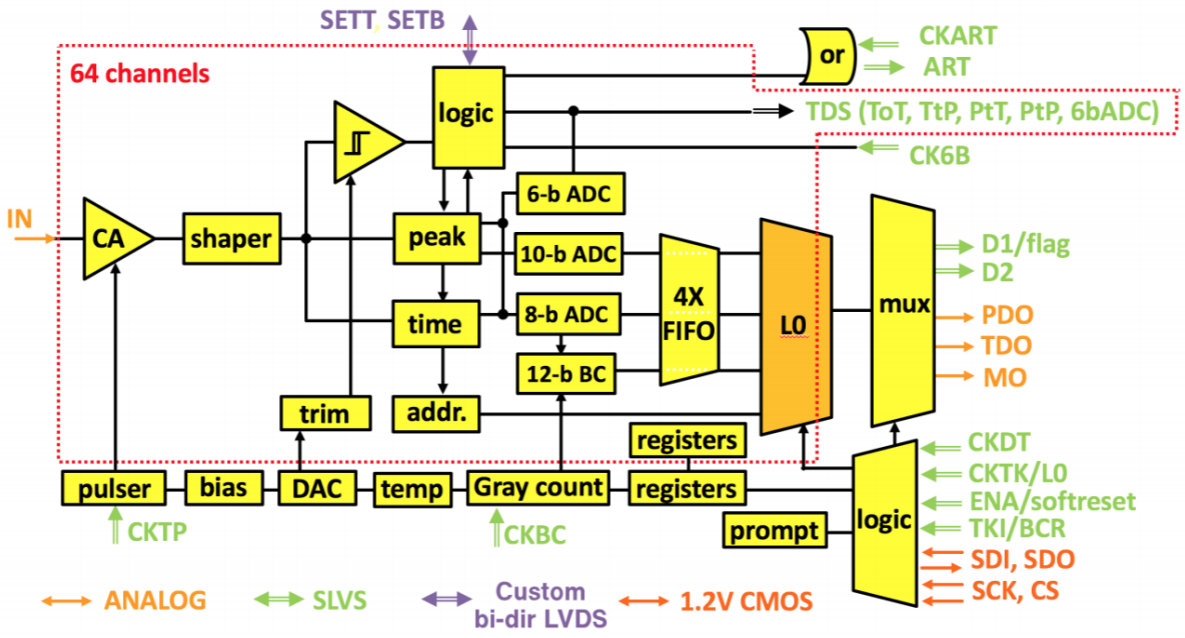

Figure 7.3.: Schematic drawing of the function principle of the VMM chip [77].

The connection of the readout to the DUT is done using a so-called *MMFE8* board. It houses eight VMMs and can therefore read 512 strips of the Micromegas. The MMFE8 version used in the test beam also has an FPGA. It collects the data from the VMMs and sends it out to the readout computer over an Ethernet connection. It also receives configurations through the network connection and forwards them to the VMMs. For the synchronization of the multiple MMFE8s a Xilinx VC709 FPGA board was used. It receives a 40 MHz clock, similar to the LHC bunch crossing clock (see next section), from a custom made *clock and trigger generation and fanout* (CTF) card [78] and forwards it to the MMFE8s. The CTF card is connected to a coincidence unit which itself is connected to the two scintillators. The coincidence signal is propagated through the CTF card to the VC709 which forwards it to the MMFE8s if none of them are busy. Since the VMM only stores the *Bunch Crossing ID* (BCID) at which the trigger arrives, and the beam is not correlated to this clock, a 25 ns jitter would be added to the time measurement. This would highly distort the reconstruction of clusters based on the drift time of the electrons. Therefore the VC709 was configured such that it only forwards the trigger signal to the VMMs if it occurred within 2 ns of a falling edge of the bunch crossing clock. This procedure was included in the VC709 firmware by Christos Bakalis [79]. For the readout of the data and configuration of the VMMs, the *VMM Embedded ReadOut Software* [80] was used, running on

a PC connected to the network of the MMFE8s. A sketch of the readout system is given in figure 7.4.

7.3. Calibration of the VMM

In order to obtain sensitive results, several quantities of the over 2000 VMM channels in the system need to be individually calibrated, amongst them the conversion of the ADC counts for the charge and time measurements into fC and ns, respectively, as well as the settings of the thresholds before each run. This section first focuses on the calibration of the time component. It is required since the slope of the TAC and the scale of the ADC is different for each channel. First the way the VMM measures time is introduced in detail, followed by a description of two calibration methods for the time measurement. The methodology, results, and the impact on the performance are discussed for both methods. The argument of the ADC scale also applies to the charge measurement, but here the differences between the channels are smaller and the impact on the performance of the DUT can be neglected. Hence the charge calibration was carried out but not applied in the data analysis and is therefore not described here. The last part of the section is devoted to the thresholds. Particular focus is given to the discussion of the impact of the thresholds on the performance of the DUT.

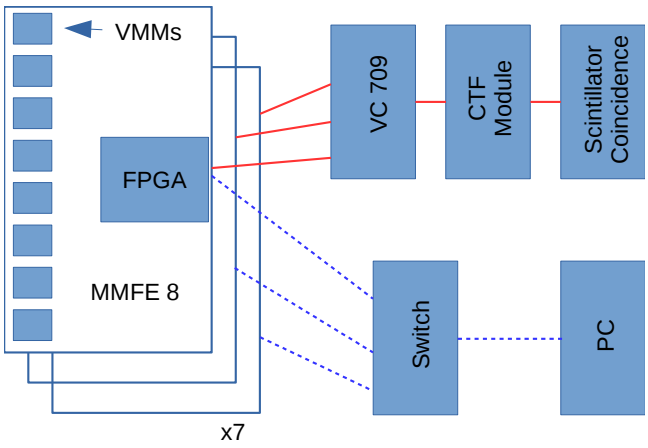

Figure 7.4.: Illustration of the readout system. Eight VMM readout chips are hosted on one front-end board, called MMFE8, which provides the connection of the detector to the VMM. Furthermore the MMFE8 hosts an FPGA which reads the digitized data from the VMM and sends it to a computer via the network. The network connections are indicated by the dashed blue lines. The FPGA also receives commands from the computer and configures the VMM accordingly. Furthermore it distributes the clock, trigger, and busy signals received from an external FPGA board of the type VC709. The clock itself is generated in a custom made CTF card configured to use the external trigger provided by the coincidence of the scintillator signals.

7.3.1. Time Measurements with the VMM

As discussed above, the VMM measures the amount of charge integrated over a settable time period and the time of arrival of the charge. Figure 7.5 shows the measurement principle of the VMM. First the incoming charge is integrated over a time window referred to as the peaking time, converting the charge into a voltage signal which peaks at the end of the integration window. The height of the peak, corresponding to the total amount of collected charge, is saved as *peak detector output* (PDO). At the peak, a TAC is started. It is stopped by the falling edge of an external clock which in ATLAS and the test beams is the 40 MHz *Bunch Crossing Clock* (CKBC). The amplitude of the TAC when it is stopped is referred to as *time detector output* (TDO). The CKBC also drives a counter in the VMM, counting the BCID, and strips with a signal above threshold carry the information of which BCID stopped the TAC. The TDO and PDO values are then digitized, converting the voltage into ADC counts, and filled into a buffer. If the external trigger

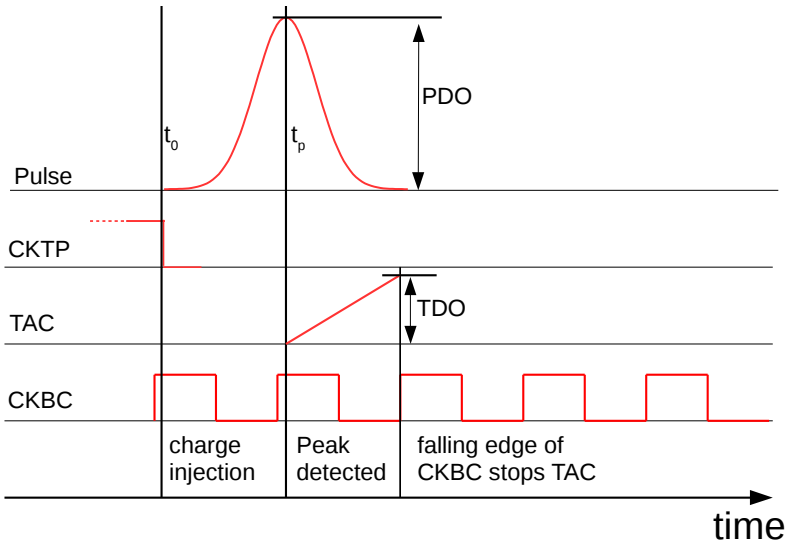

Figure 7.5.: Measurement principle of a VMM channel. The charge, either coming from the detector or induced as a test pulse as shown here, arrives to the channel at time t_0. Then the shaping amplifier integrates the charge, converting it into a voltage for a settable time leading to a peak in the voltage signal at t_p. The peak height, corresponding to the charge integral, gets digitized and stored as PDO counts. The detection of the peak also starts a TAC. It is stopped by the next falling edge of the external bunch crossing clock, provided by the LHC. The amplitude of the TAC is then digitized and stored as TDO counts. Since the TAC slopes and the ADCs of all channels are different, they need to be calibrated individually.

found a coincidence between the scintillators, a trigger signal is sent to the VMM and it outputs all hits in a window of up to eight BCIDs around the BCID given by the trigger. These hits are all marked with the trigger BCID; additionally they carry the information about their BCID relative to the one of the trigger. This information is referred to as the *relBCID*.
Combining the information from the relBCID and the TDO, the time of arrival t of a signal at a strip can be determined as follows:

$$t = \text{relBCID} \times 25\,\text{ns} - \text{TDO}_{\text{calib}} + t_{\text{Latency}}, \tag{7.1}$$

where $\text{TDO}_{\text{calib}}$ refers to the converted TDO counts in ns and t_{Latency} denotes the processing time of the trigger. Details on the calibration of the TDO follow in the next chapter.

7.3.2. Time Calibration of the VMM

For the time calibration of the over 2000 VMM channels, two methods have been used, which will be discussed in the following. The first method relies on the injection of test pulses with an adjustable time into the VMM channels while the second method is based on a data-driven approach.

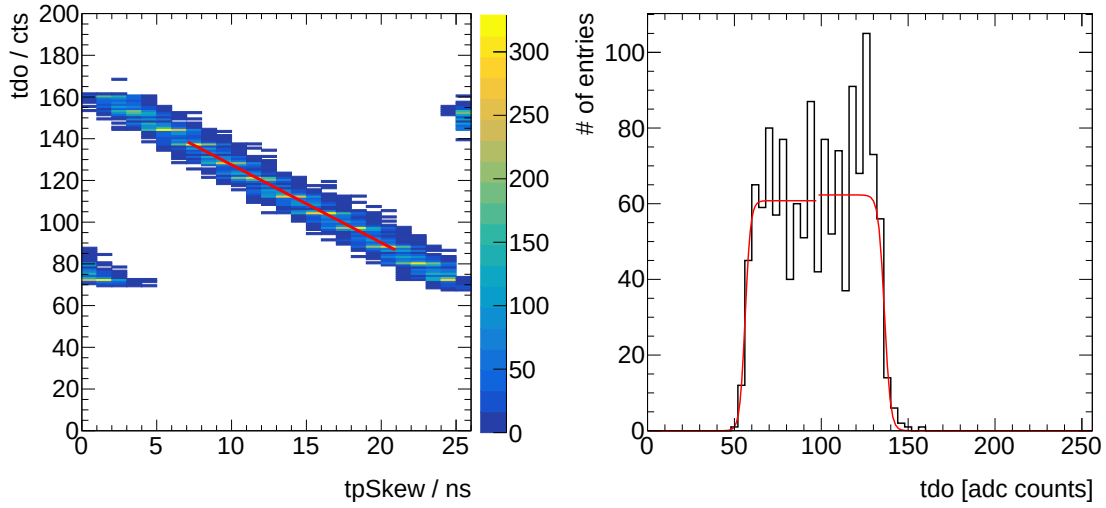

(a) Pulser-driven calibration

(b) Data-driven calibration

Figure 7.6.: Example distributions as employed for the two TDO calibration methods. **Left:** TDO value as a function of the skew between the test pulse clock and the bunch crossing clock. The slope and the intercept are extracted by a linear fit in the central region of the histogram. **Right**: TDO distribution of a VMM channel for a run. A fit with a Fermi function is carried out on both edges. The slope and the intercept are determined using the fact that by construction of the VMM, the left edge is equivalent to 12.5 ns and the right one to 37.5 ns.

Pulser-Driven Calibration

The VMM has the ability to inject test pulses into each of its channels. The timing of the test pulse can be controlled by an external clock, the CKTP (see figure 7.5). For the MMFE8s used in the test beam, the CKTP is provided by the FPGA. Using the fact that the TDO gives the time between the peak and the next falling edge of the CKBC, the TDO can be calibrated by changing the phase between the CKTP and the CKBC. Figure 7.6a shows the TDO as a function of the phase shift between the CKTP and the CKBC. A linear behavior can be observed in the central region while in the outer regions the assignment of the peak to the previous or the following BCID is visible. To extract the slope and the intercept of the TAC, the central region is fitted with a straight line. Figure 7.7a shows the TAC slopes for the 512 channels of an MMFE8. Huge variations of the slope over the channels can be observed. Therefore a different method to calibrate the TAC slope was investigated which is described in the following.

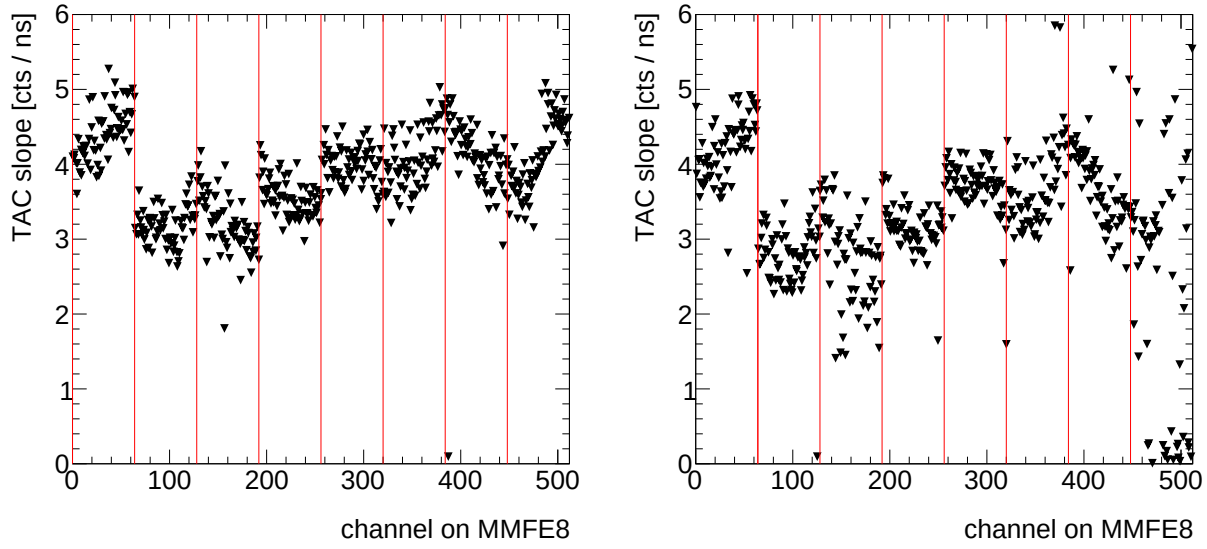

(a) Pulser-driven calibration

(b) Data-driven calibration

Figure 7.7.: Comparison of the TAC slopes for the two calibration methods. The two figures show the TAC slope as a function of the channel number for one exemplary MMFE8, hosting 8 VMMs. The vertical red lines indicate the boundaries of the individual VMMs.

Data-Driven Calibration

The idea for the data-driven calibration method was given in [81]. It is based on the fact that the TAC yields the time until the next falling edge of the CKBC, but only if the peak occurred before a rising edge of the CKBC. Given the CKBC frequency of 40 MHz, these constraints lead to the TAC being limited to a time range of 12.5 – 37.5 ns. Consequentially, the TAC slope can be

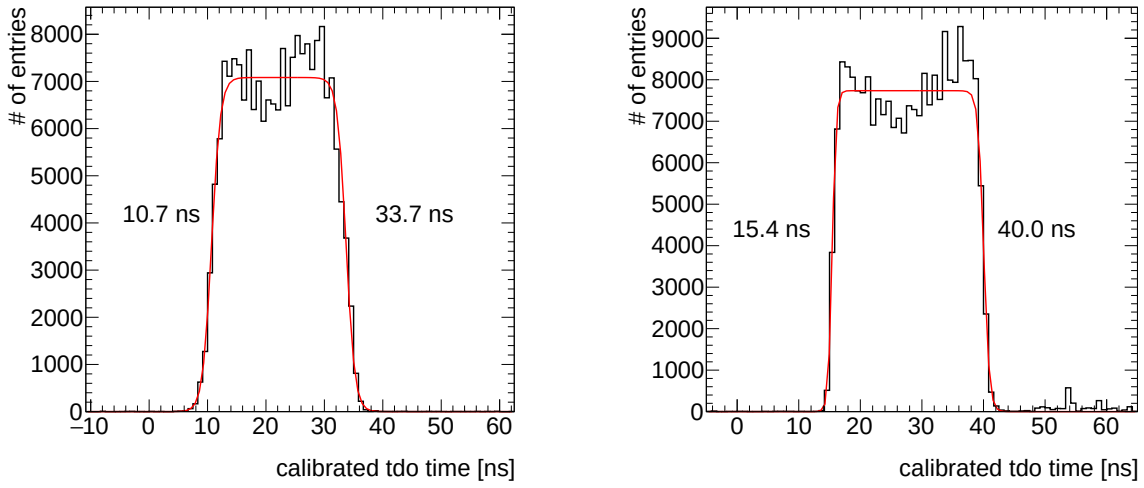

(a) Pulser-driven calibration

(b) Data-driven calibration

Figure 7.8.: Comparison of the calibrated time of the TAC for the two calibration methods. Both distributions are fitted with a double Fermi function. For the data-driven calibration the width of the distribution is in agreement with the expected 25 ns, while for the pulser calibration the distribution is slightly narrower.

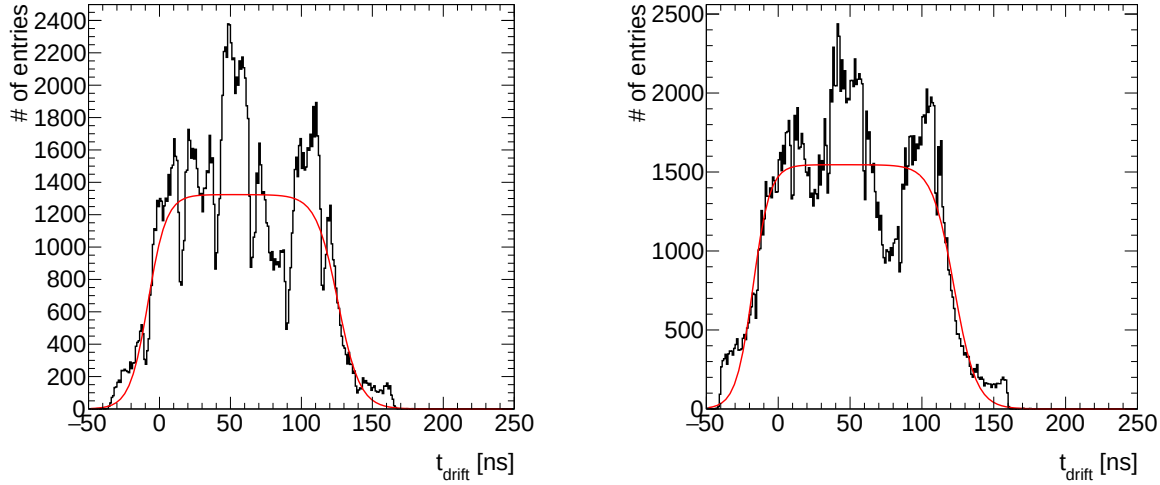

(a) Pulser-driven calibration

(b) Data-driven calibration

Figure 7.9.: Comparison of the drift time distribution for the two calibration methods. Both distributions show a similar overall shape, which is also in agreement with the expectation. The periodic dips in the distribution using the pulser-driven method can be explained by the slightly underestimated TAC slope.

determined using the width of the TDO distributions of a run, while the intercept can be obtained from the position of one of the two expected edges. Figure 7.6b shows the TDO distribution for one run. The two edges are fitted with Fermi functions. The width of the total distribution is determined from the position parameters of the two Fermi functions. Dividing the width by 25 ns then yields the TAC slope which is shown in figure 7.7b for the 512 VMM channels of an MMFE8 obtained with the data-driven calibration method.

Comparison of the Performance of the two Calibration Methods

Figure 7.7 compares the TAC slopes for an MMFE8 obtained with both methods. As can be seen, both methods yield consistent results while the width obtained with the data-driven method, visible in figure 7.8, has the expected size of 25 ns. The pulser-based calibration, on the other hand, shows a slightly smaller width of 23 ns. Figure 7.9 depicts the total drift time, i.e. the combination of the TAC time with the relBCID, for both calibration procedures. The drift time distribution with the pulser-based calibration shows periodical dips with a distance of 25 ns. Those can be explained by the TAC time spectra being too narrow, hence, not filling the full range between two relBCIDs. Apart from the dips, both drift time distributions have the same shape.

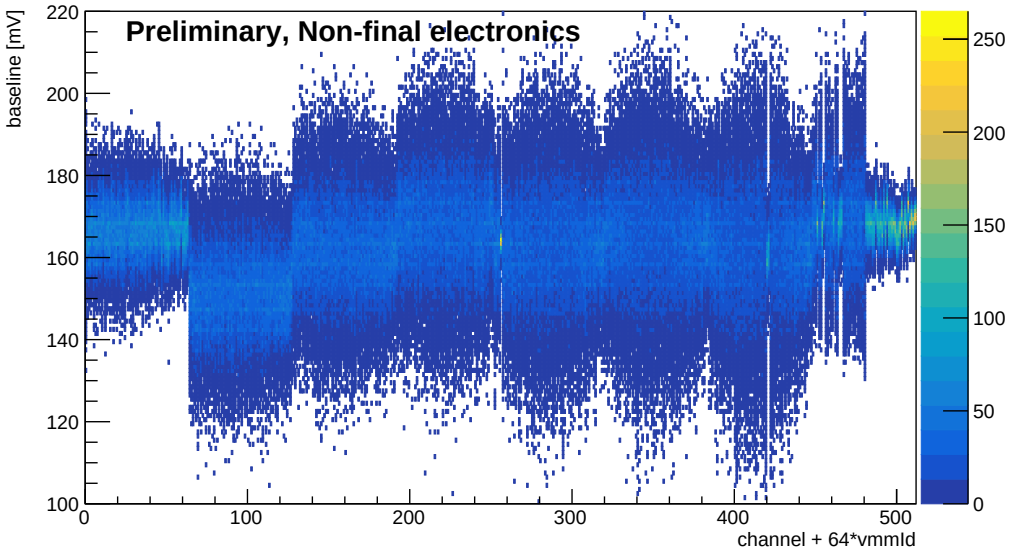

Figure 7.10.: Baseline measurement for all VMM channels on an MMFE8. The baseline is measured by sampling the VMM signal after the amplifier by the external FPGA. It serves as the basis to determine the noise levels, which are extracted as the RMS of the baseline of each channel. The threshold is then set by adding x times the noise to the median baseline, where x is referred to as threshold scale factor.

7.3.3. Noise Levels and Thresholds of the Test Beam Setup

Due to the enormous lengths of the strips in the large Micromegas chambers of up to 2 m, and consequently the high capacity between strips, Micromegas detectors are very sensitive to noise. Therefore it is important to quantify the noise levels before taking data and to set the thresholds on the VMMs accordingly. For the calibration of the VMM threshold, the analog output of the VMM, i.e. the signal after the shaping amplifier, can be sampled by the FPGA. This measurement yields the so-called *baseline*. A typical baseline for an MMFE8 is shown in figure 7.10. The threshold of the channels is determined by adding x times the RMS of the channel baseline to the median baseline, where x is called *threshold scale factor*.
As mentioned before, setting the threshold includes two configuration parameters of the VMM. First a global threshold is set for all channels of a VMM, then the individual channels are trimmed. Since the channel trimming is not functioning in the VMM3[2], only a chip-wide threshold could be applied in the test beam. It was determined using the median and the RMS from the baseline of an entire chip. The noise levels measured in the test beam are shown in figure 7.11 and

[2]This was one of the major reasons to develop the next VMM version, the VMM3a.

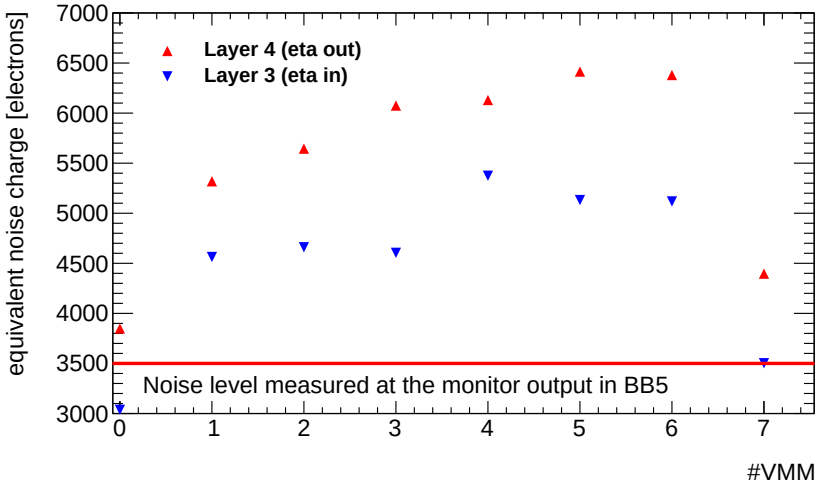

Figure 7.11.: Comparison of the noise level as observed during the test beam and after its optimization in the BB5 integration facility. The data points show the RMS of the eight VMMs reading layer 3 (blue) and layer 4 (red) of the SM2 quadruplet. The red line indicates the noise levels which were achieved by improved grounding measures as investigated after the test beam. The theoretical lower limit for the strip length of the strips used in the test beam is 3300 electrons. VMMs 0 and 7 show lower noise levels since only part of their strips are connected to copper strips of the DUT. The strips which are connected to these VMMs were not exposed to the beam, therefore the biased noise measurement had no impact on the results obtained in the test beam.

compared to the theoretical prediction of the lower limit of noise derived from the strip capacity and the simulation of the VMM. While the theoretically lowest *equivalent noise charge* (ENC) is 3300 electrons, the measurement in the test beam yielded values of 4500 – 6500 electrons depending on the layer and the VMM number. Since the measured noise did not fully follow a Gaussian distribution, thresholds of six times the noise had to be applied in order to properly suppress noisy strips, leading to charge thresholds of 4.3 – 6.2 fC. After the test beam the noise on the detector could be reduced to the theoretical limit by several improvements of the grounding within the quadruplet and for the power supplies. With the imperfect grounding in the test beam, the long strips of the detector worked as antennae, picking up electromagnetic distortions in the test beam hall, where several experiments are running in parallel.
Figure 7.12 shows the percentage of strips lost as a function of the applied threshold. It indicates the importance of keeping the noise levels and consequently the applied threshold as low as possible. For the values used in the test beam the percentage of strips below the threshold is 60 – 70 %. For the small Micromegas prototype detectors with a strip length of only 10 cm, and subsequently a lower capacitance, the noise level is typically in the order of 350 electrons leading to signal losses of below 20 %.

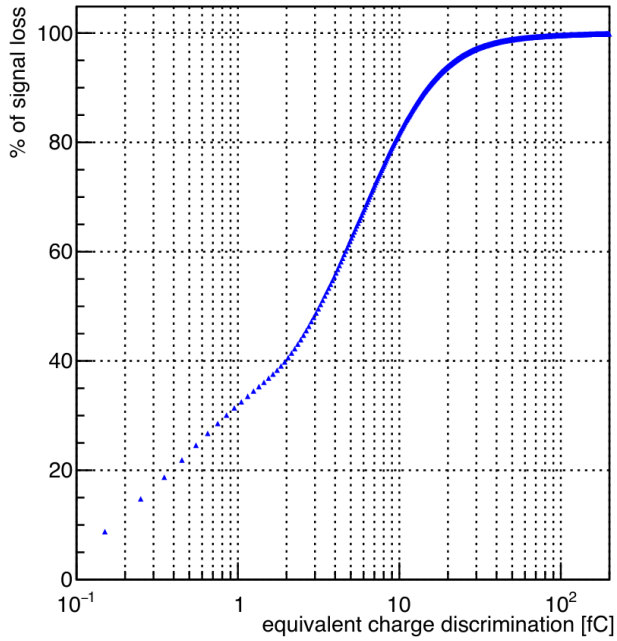

Figure 7.12.: The percentage of the simulated signal loss as a function of the discriminated equivalent charge from a random strip within a cluster. The simulation was performed for incident particles traversing the detector plane under 30° and with a detector gain of $\sim 10^4$. For the thresholds used in the test beam, which are 4.3 – 6.2 fC, about 60 – 70 % of the strips are lost. Plot and parts of the caption taken from [82].

8. Reconstruction Performance

This chapter discusses the performance of the SM2-M1 (DUT), the first SM2 module from the series production, in a test beam carried out in the north area of CERN in 2018. The setup deployed in the test beam was discussed in the previous chapter. It consists of the DUT itself and three smaller single-layer Micromegas detectors which provide an external track used to study the resolutions and efficiencies of the layers of the DUT. In this test beam, the readout chip deployed in the NSW, the VMM, was used for the first time on a full sized Micromegas quadruplet. While the final version of the chip was not yet available, the readout was performed with the pre-final version, the VMM3.
This first section of this chapter introduces the definitions of the quantities relevant to determine the performance of a layer of the DUT, namely the resolution and the reconstruction efficiency, together with a short summary of the general event selection. In the second section, the performance of the DUT is discussed for perpendicuar tracks, which is a benchmark to verify that the VMM is working on the full-sized quadruplets. Furthermore the impact of different measures to improve the HV instabilities of the Micromegas detectors on the detector performance has been investigated. In sections three and four the performance of the DUT is studied for inclined tracks as they will be present in the NSW. The methods for the reconstruction of clusters from those inclined tracks were introduced in section 6.3 and are applied here, in particular the μTPC and the CTP method.

8.1. Definition of Reconstruction Quantities

In this section the quantities relevant to quantify the performance of a detector layer, namely the spatial resolution and the reconstruction efficiency, and the methodology to derive them are introduced. First the selection criteria for events are discussed, where an event is considered good if a well-defined external track is present. The resolution of a layer of the DUT is then obtained by comparing the position of the reconstructed cluster with the position of the external track in that layer. Finally the efficiency of a layer of the DUT is determined by counting events with a cluster close to the external track.

8.1.1. Event Selection and External Tracking

In the test beam setup three small single-layer Micromegas are placed perpendicular to the beam up and downstream of the DUT, providing an external track measurement. In order to reconstruct

the track, the strips above threshold in each of the three detectors are clustered using the centroid method described in section 6.3.1. In case this yields one cluster per tracking detector, and the clusters from the three detectors are roughly on a line, a straight line is fitted through the cluster positions in all three layers and the event is included in the analysis. If any of the layers of the tracking detectors contain no or more than one cluster, or the cluster positions do not line up, the event is excluded from the analysis. Further reasons to exclude events are based on the sanity of the readout system, e.g. events with certain spurious patterns in the data, like duplicated hits, are excluded since these can be traced down to a miscommunication of the VMM and the FPGA on the MMFE8.

8.1.2. Resolution

The resolution of a single layer is extracted as follows. First the cluster closest to the external track is identified. Then the distance between this cluster and the extrapolated position of the external track on the DUT, referred to as *residual*, is stored in a histogram. The residual is extracted for every event in this layer, and the histogram will show a Gaussian distribution with additional symmetric tails. An illustration of such a histogram is depicted in figure 8.1. A fit with the sum of two Gaussians is performed, one to take into account the narrow core of the observed

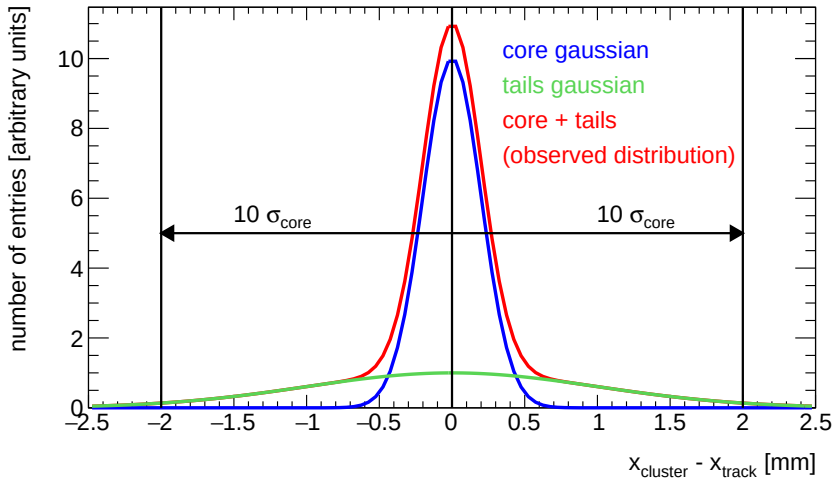

Figure 8.1.: Illustration of the fit to extract the resolution and efficiency of a single layer. The distance of the cluster closest to the track in the layer under study is filled into a histogram for every event. The observed distribution is a Gaussian with additional tails. Therefore a fit with the sum of two Gaussian distributions is performed (red), a narrow one (blue) for the core of the distribution and a wide one (green) for the tails. The efficiency of a layer is determined by the number of events in a window of $\pm 10\,\sigma_{\text{core}}$ around the mean value of the core Gaussian, compared to the total number of events with an external track.

distribution and one to consider the wide tails. The fit range is chosen to be ± 5 times the width of the narrow Gaussian. Two quantities describing the detector resolution are derived from this fit. The *core resolution* refers to the width of the narrow Gaussian while the *weighted resolution* is determined by weighing the widths of the two Gaussians by their integrals as follows:

$$\sigma_{\text{weighted}} = \frac{A_{\text{core}}\sigma_{\text{core}}^3 + A_{\text{tails}}\sigma_{\text{tails}}^3}{\sigma_{\text{core}} + \sigma_{\text{tails}}}. \tag{8.1}$$

In order to obtain the final resolution, the uncertainty of the position of the external track on the probed layer, referred to as *extrapolation error* σ_{extr}, needs to be taken into account. The final resolution can be determined as follows:

$$\sigma = \sqrt{\sigma_{\text{layer}}^2 - \sigma_{\text{extr}}^2}, \tag{8.2}$$

where σ_{layer} is either the width of the core Gaussian or the weighted width of the two Gaussians. The calculation of the track extrapolation error is discussed in [72]. For three layers of external tracking detectors, σ_{extr} can be computed as follows:

$$\sigma_{\text{extr}} = A\sigma, \tag{8.3}$$

with σ being the resolution of the individual tracking detectors and A being:

$$A = \frac{1}{2}\frac{3z_0^2 + z_1^2 + z_2^2 + z_3^2 - 2z_0(z_1 + z_2 + z_3)}{z_1^2 + z_2^2 + z_3^2 - 2z_1(z_2 + z_3)}, \tag{8.4}$$

where z_0 is the position of the probed layer along the beamline and z_{1-3} are the positions of the tracking detectors. Inserting the geometry of the setup and a resolution of the tracking detectors of $100\,\mu$m yields:

$$\sigma_{\text{extr}} \approx 60\,\mu\text{m}. \tag{8.5}$$

8.1.3. Efficiency

Another value that is relevant to quantify the performance of a layer is the reconstruction efficiency, which describes the chance to find a cluster with a given reconstruction method in case an external track was present at the particular location. It is derived from the fit of the resolution illustrated in figure 8.1. A layer is considered efficient if a cluster was reconstructed within 10 times the width of the narrow Gaussian. Therefore the number of entries in the histogram is summed up in a window of ± 10 times the width of the core Gaussian around its mean value. The efficiency is then obtained by dividing the sum of entries in the window by the total number of events where an external track was identified (see section 8.1.1). This is a standard procedure agreed on by the Micromegas community.

8.2. Performance for Perpendicular Tracks

The first goal of the test beam campaign was the validation of one of the first full-sized Micromegas quadruplets from the series production and its readout using the VMM chip for the first time. For this purpose, the quadruplet was set up perpendicular to the beam. For the clusterization, the centroid method was used as described in section 6.3.1. Figure 8.2 shows a typical plot of the residuals for perpendicular tracks for which resolutions of around 100 μm could be achieved. For the characterization of the detector, several parameter scans have been performed, e.g. scans of the high voltage applied on the strips or scans of different parameters of the VMM. Figure 8.3 shows the reconstruction efficiency for perpendicular tracks for different HV values applied to the resistive strips. This study had the goal to validate the new reduced HV working point (570 V) of the Micromegas detectors in ATLAS. At this voltage all four layers show efficiencies above 90 % which is in agreement with the requirements for the operation in ATLAS. Therefore this reduced working point is considered validated.
Since there are studies ongoing which investigate the performance of different gas mixtures with respect to potential improvements of the high voltage stability of the detector, similar efficiency scans have been carried out with different admixtures of CO_2. A higher fraction of the quenching gas CO_2 is desirable as it suppresses sparks and therefore improves the stability of the amplification

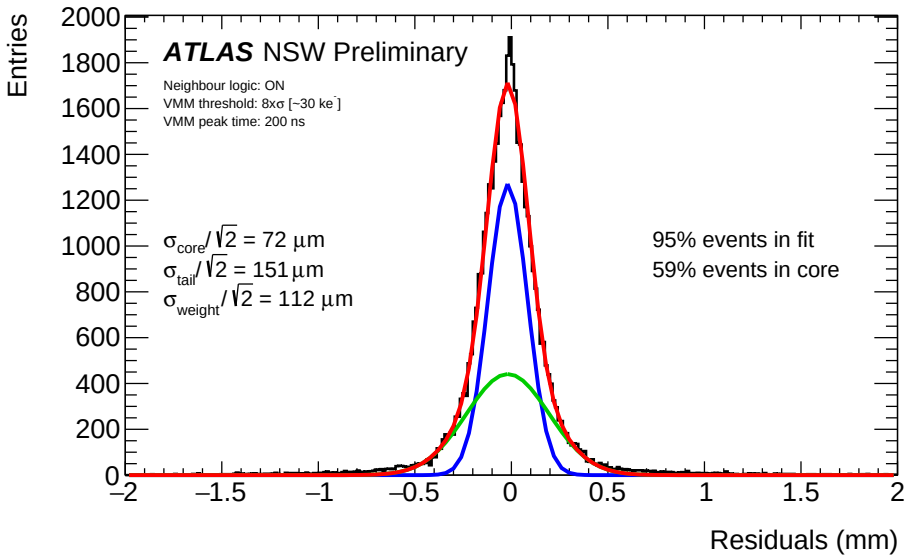

Figure 8.2.: Position resolution of the DUT for perpendicular tracks. The clusters and their positions are reconstructed using the centroid method. The residuals are determined by comparing the cluster positions in two adjacent η layers. Since the fit result corresponds to the convoluted resolution of the two layers and it is assumed that both layers have the same resolution, the single-layer resolutions are obtained from the widths of the Gaussian fits divided by $\sqrt{2}$. Figure taken from [2].

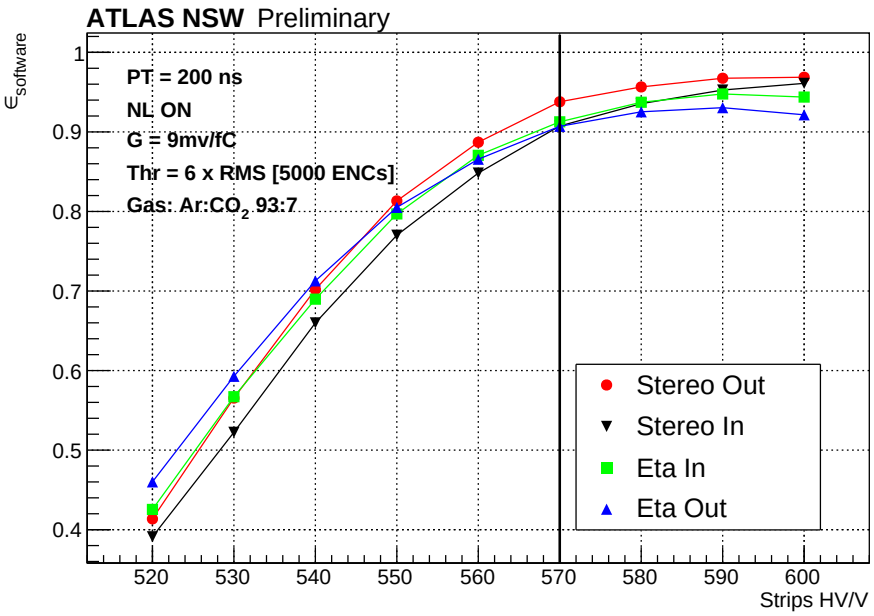

Figure 8.3.: Efficiency scan with perpendicular tracks as a function of the applied voltage on the strips. Due to voltage instabilities the voltage applied on the strips was reduced from 600 V to 570 V indicated by the horizontal line. The plot shows that also at the reduced working point the reconstruction efficiency is above 90 %. Therefore the new working point is considered validated.

field, though it comes at the expense of a reduced gas gain and a reduced number of primary ionizations. The spatial resolution was proven to be stable over all mixtures. Figure 8.4 shows the achieved efficiencies over the different mixtures, all of which are $\geq 95\,\%$.

8.3. The μTPC Method for Inclined Tracks

In ATLAS the NSW detectors will have to handle tracks with an inclination between $8^\circ \leq \theta \leq 31^\circ$ with respect to the detector surface. As mentioned in chapter 6.3, the reconstruction of inclined tracks with the centroid method yields unacceptable resolutions in the order of 500 μm for tracks under an angle of 30° due to non-uniformities in the ionization processes. Therefore more sophisticated clusterization methods using the drift time in addition to the strip positions need to be deployed, amongst them the so-called μTPC method (see section 6.3.3). The performance of this method was assessed in the test beam.

In this section, first the selection criteria and corrections applied in the μTPC method for the test beam analysis are described and typical quantities of the μTPC clusters, like the shape of the cluster, the drift time, and the reconstructed angle, are compared with the expected shapes.

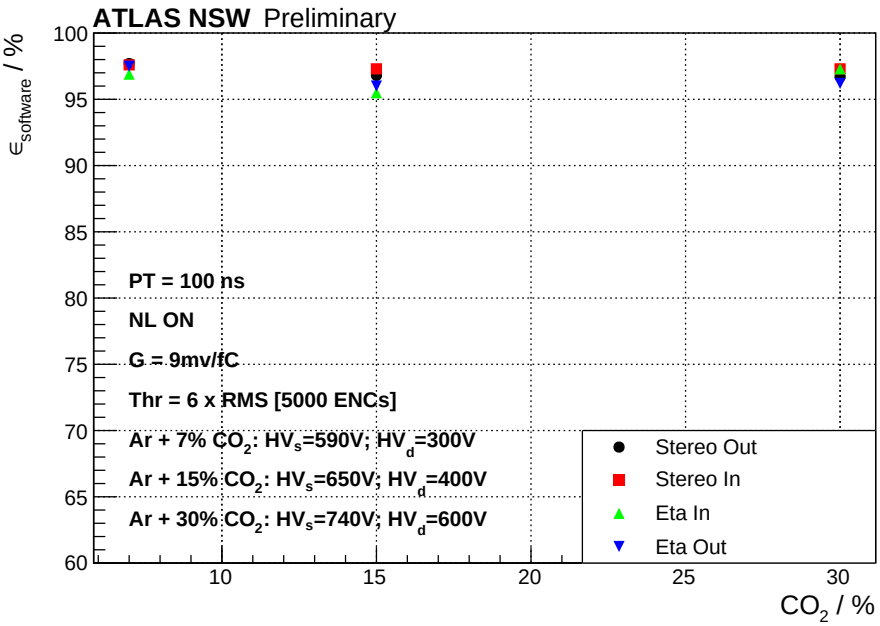

Figure 8.4.: Efficiency scan with perpendicular tracks for different CO_2 fractions in the used gas mixtures. Excellent reconstruction efficiencies above 95 % have been achieved for all three mixtures that were studied.

Then a measurement of the CS between strips, a process with a high impact on the time and subsequently position resolution, is presented. Finally the resolution and reconstruction efficiency of the μTPC method are discussed.

8.3.1. Selection Criteria and Corrections Applied in the μTPC Analysis

For the optimization of the μTPC method several selection criteria and corrections were introduced that are presented in the following. Since the μTPC method uses a straight line fit of the strip position and the drift time, a minimum of three strips are required to be close enough to the predicted line of the HT to be accepted (see section 6.3.3 for details).
Figure 8.5 shows the spectrum of angles reconstructed with the μTPC method. Some unphysical behaviors can be identified in the spectrum. The peaks towards $\pm 90°$ refer to tracks that are parallel to the mesh. They can be traced back to mainly three-strip clusters with bad timing information. To exclude those events, a filter on the absolute value of the reconstructed angle being smaller than 85° is applied. Furthermore the absolute value of the angle is required to be larger than 5° to avoid the peak around 0°. The clusters with the wrong sign of angle are rejected, since this is also unphysical behavior, coming from small clusters with bad timing information. The correct sign of the angle is given by the number of the gas gap. Since in the quadruplets the layers are mounted back-to-back, the electron drift direction in layers zero and two is along

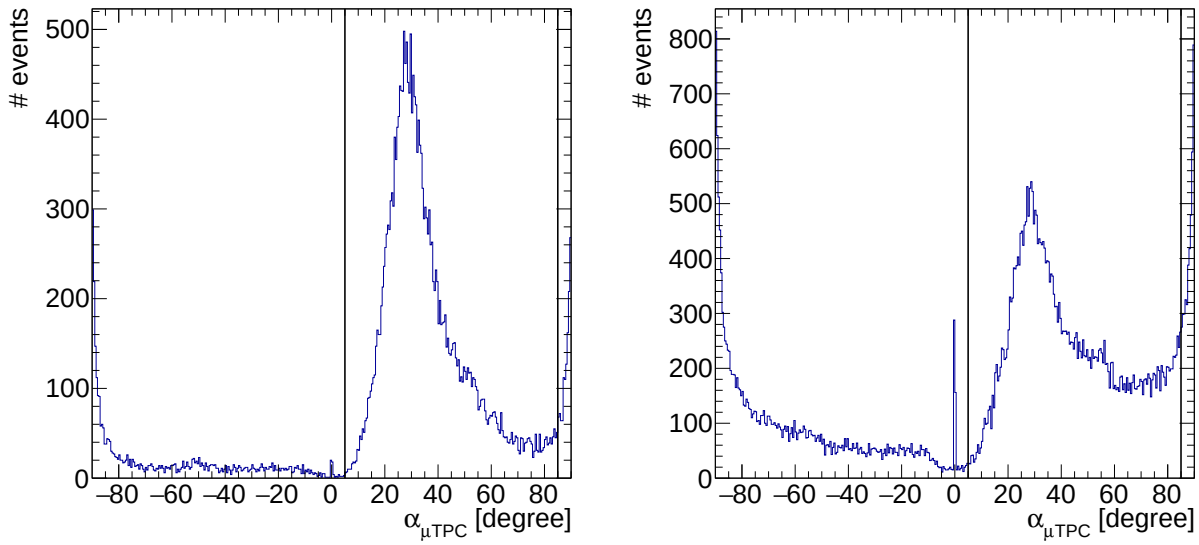

(a) Neighbor logic off

(b) Neighbor logic on

Figure 8.5.: Angles reconstructed by the μTPC method for different settings of the NL. A filter is applied to exclude angles greater than $\pm 85°$ coming from small clusters with bad timing information. A second selection is applied to exclude clusters with a reconstructed angle smaller than 5°. Also clusters where the reconstructed angle has the wrong sign are rejected.

the beam, while it is against the beam direction for the gas gaps one and three. Therefore the reconstructed track angles of the odd gas gaps are expected to be negative while the even gas gaps should have positive angles. These filters on the reconstructed angles are especially relevant for the case of the NL being on, since here the amount of events with unphysical values is higher than for the case of the NL being off. While the NL is meant to increase the reconstruction efficiency of a layer, which is the case as shown later, it also enhances the amount of events where the μTPC method reconstructs the wrong angle. This mostly happens when a single strip is over threshold and the neighboring strips get the charge via the capacitive coupling, therefore having the same timing as the main strip. These kinds of clusters lead to high values for the reconstructed angle since they appear to be parallel to the mesh. A discussion of the non-excluded part of the angular distribution follows in the next section.

Figure 8.6a shows the distance of the closest μTPC cluster to the estimated position of the external track (residual) as a function of the earliest hit in the cluster. Two observations can be made. First, if the earliest hit in a cluster arrives later than 60 ns the residuals become larger. Therefore a filter is applied on the earliest hit time to be less than 60 ns. Second, there is a strong dependence of the residuals as a function of the arrival time of the earliest hit, better visible in the profile[1]

[1]The profile is the mean value in each bin along the x axis.

shown in figure 8.6b. A fit with a second-order polynomial is performed on the projection and used as a correction in the reconstruction software. The time values mentioned here correspond to the raw times which do not yet take into account the corrections for the latency of the system.

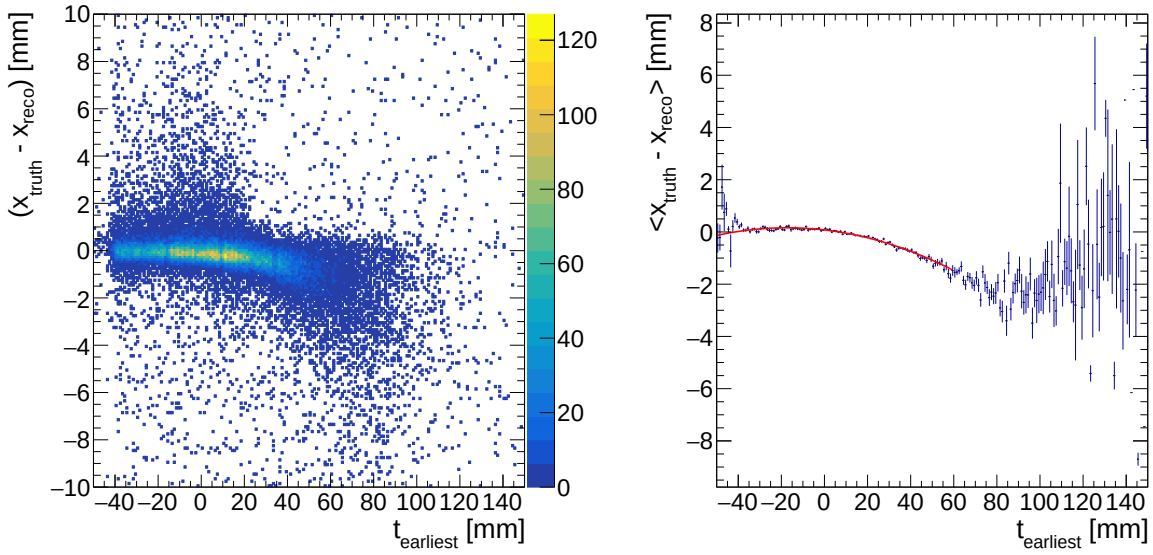

(a) μTPC residuals

(b) Mean μTPC residuals

Figure 8.6.: Dependence of the μTPC cluster position on the time of the earliest hit in the cluster. Since the distribution widens significantly for time values later than 60 ns, clusters that fall into that regime are rejected. Furthermore the dependence of the cluster position on the time of the earliest hit can be identified in the projection in the right plot. This distribution is fitted with a second-order polynomial which is used to correct the cluster position in the reconstruction.

8.3.2. Typical Quantities of μTPC Clusters

In the following, the typical quantities of clusters reconstructed with the μTPC method for a run with the Micromegas quadruplet inclined with respect to the beam direction are shown. Specifically an inclination of 28° was chosen, in order to study an angle close to the maximal one for the tracks in the NSW. The run presented here used a VMM peaking time of 200 ns, a threshold of six times the baseline RMS of 5000 electrons, and the NL of the VMM was switched on. The HV section was operated at 580 V using the default gas composition of a 7 % admixture of CO_2 to Argon. Figure 8.7a shows the number of strips entering into the μTPC cluster. From geometrical considerations a peak at 6 to 7 strips is expected as seen in the histogram. Compared to results obtained with much smaller Micromegas prototypes years before, depicted in figure 8.7b, the distributions show an enhanced population of the bins of lower cluster multiplicity. This is due to the high charge threshold that had to be applied on the VMM as a result of the noisy

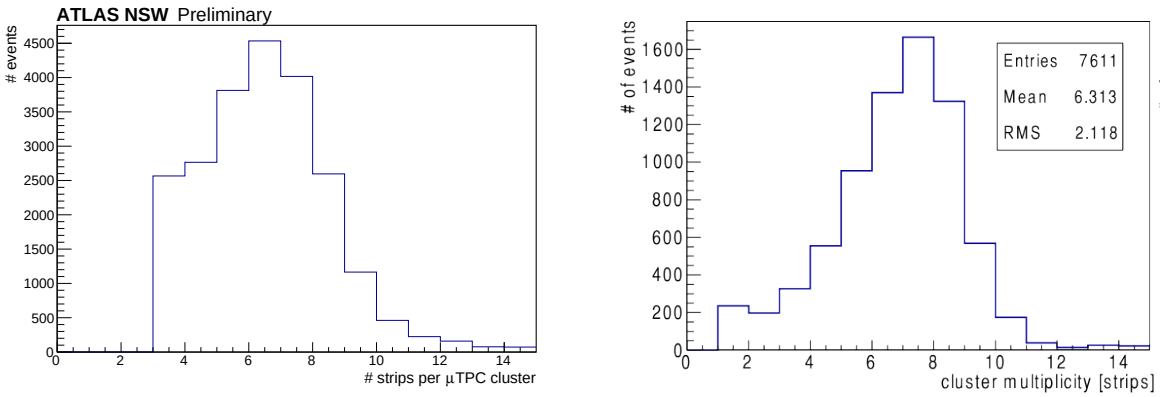

(a) Number of strips in a μTPC cluster in the SM2 module.

(b) Number of strips in a μTPC cluster for a smaller Micromegas prototype in an earlier study [71].

Figure 8.7.: Comparison of the number of strips in a μTPC cluster in the SM2 module used in the test beam (left) and a smaller Micromegas prototype chamber (right). Both distributions show a peak at 6 to 7 strips, as expected. The population towards smaller cluster sizes falls rapidly for the small prototype chamber, but this is not the case for the SM2 module. The difference stems from the much higher charge threshold applied in the SM2 due to the longer strips.

environment in the test beam, leading to 60 – 70 % of strips with a charge below threshold. For the small Micromegas detectors with a strip length of only 10 cm, the noise level is significantly smaller, leading to a loss of only 20 % of the strips. The details on the threshold and its impact are described in section 7.3.3.

The overall drift time distributions of the hits contained in a μTPC cluster are already shown in the context of the VMM calibration in figure 7.9. However, only the calibration is discussed there but not the physics of the observed drift time distributions, which is done here instead. From the thickness of the drift gap of 5 mm and the drift velocity of 47 μm/μs a maximum drift time of 106 ns is expected, which will widen due to diffusion and other effects impacting the time resolution, e.g. CS. As expected, the shape of the distribution is square-like, since the primary ionizations happen uniformly in the drift gap. The little peaks at the beginning and the end of the spectrum can be explained geometrically, i.e. the position of the first and last ionizations do not correspond to the center of the strip they are arriving at (discussed later in section 10.3.7), while on average this is the case for the central ones. The peak in the middle is not expected, but could be caused by the low number of strips in a cluster, since the outer strips with a more extreme timing have a lower charge and therefore a higher chance to be below threshold. To quantify the distribution, a fit with a double Fermi function is applied yielding a width of the distribution of 139 ns for the data driven calibration and of 133 ns for the pulser driven calibration method, which is in agreement with the expectations.

Figure 8.8 shows the incident angle reconstructed by the μTPC method after the selection criteria

were applied. The peak of the distribution corresponds to the actual inclination of the chamber of 28°. A resolution of 7.1° was obtained around the peak, but a long tail towards higher angles can be identified. It stems from clusters with a lower number of strips giving a smaller lever arm for the angle reconstruction. From the distribution of the angle before the filters were applied, shown in figure 8.5, it can be seen that the tails are much more enhanced for the case of the NL being on. Then, small clusters are recovered but the time measured on the strips read out due to the NL is distorted by the CS between strips leading to a deterioration of the reconstruction performance.

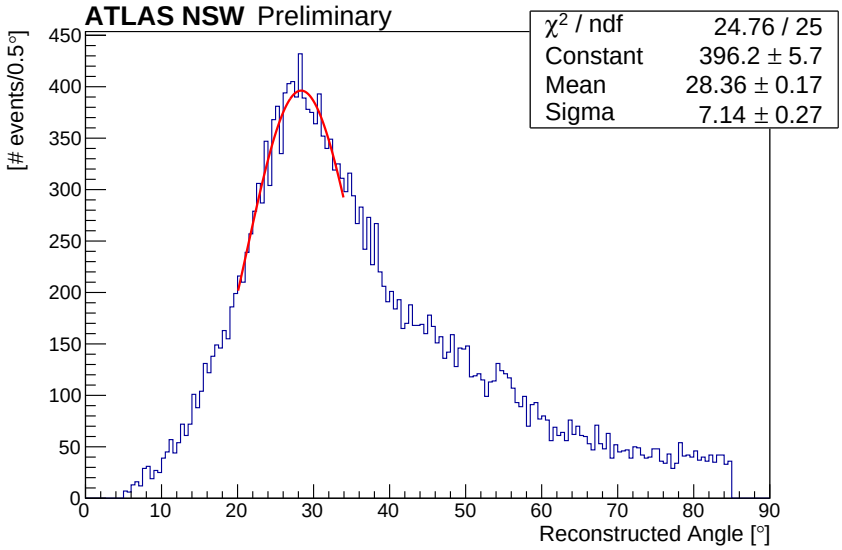

Figure 8.8.: Distribution of the angle reconstructed with the μTPC method after selection criteria have been applied. The NL was not enabled for this measurement. The peak of the distribution corresponds to the actual inclination of 28° of the tested chamber. The large tails towards higher angles are mostly coming from badly reconstructed clusters with a small size but also from the impact of the CS on the time measurement.

8.3.3. Measurement of Charge Sharing

As described in section 6, the Micromegas detectors used in the NSW have a layer of resistive strips on top of the actual copper strips. The charge from the avalanche arrives on the resistive strips and induces a signal on the copper strips via capacitive coupling (see figure 10.5). Given the small strip pitch, the thin gap between two strips, and the very large strip length, the charge signal on a resistive strip is not only coupled to the underlying copper strip but also to neighboring copper strips. This effect is called CS and its amplitude is critical for the time resolution of the Micromegas detectors.
Clusters reconstructed with the μTPC method can be used to measure the magnitude of CS by

comparing the charge on the outermost strip with its neighbor strip, assuming the outermost one only fired due to CS. For this measurement the NL was enabled. Figure 8.9a shows the ratio of the charge between the first strip in a μTPC cluster and its neighbor, while figure 8.9b depicts the charge ratio of the two central strips. For the central strips a charge ratio of 1 can be seen, as expected. For the outer strips the charge ratio peaks at a value of 1.5, indicating CS of 67 %. Similar studies carried out for the Micromegas prototype detectors of the size of 10 cm×10 cm in [72] yielded a value of 16 % while [69, 83] suggest the CS ratio to be around 30 % over the full SM2 module. The differences can be explained as follows: the study presented here was done at the point of the longest strips of the DUT where CS is expected to be larger due to the higher strip capacitance. Furthermore the two aforementioned measurements were carried out with the APV25 [84] readout chip in contrast to the VMM3 used here.

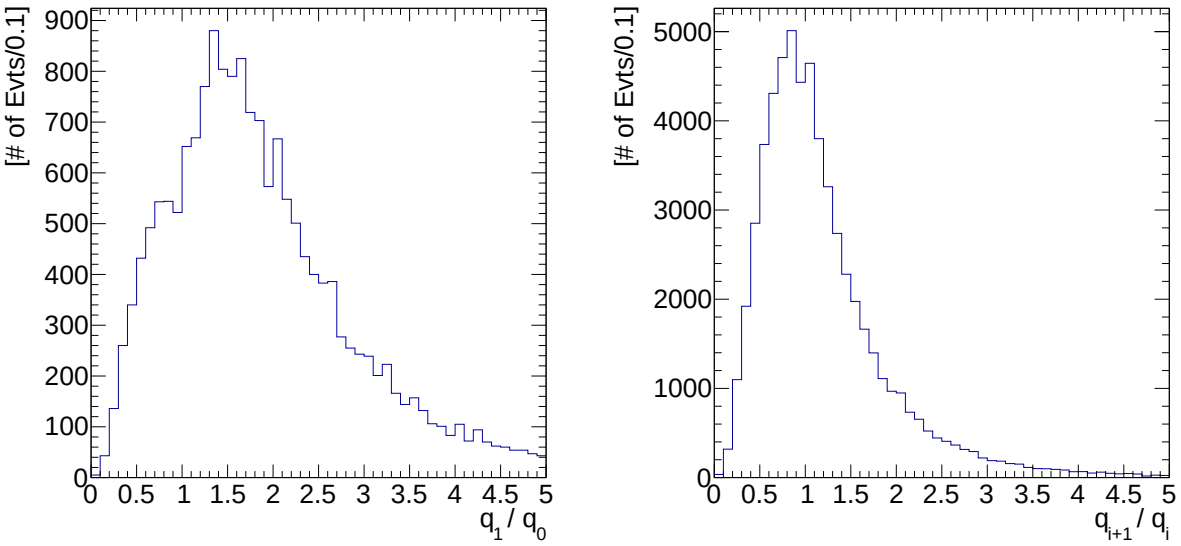

(a) Charge ratio of the first and second strip

(b) Charge ratio of the central strips

Figure 8.9.: Measurement of CS using the charge ratio of neighboring strips. While the distribution for the central strips (right) peaks at 1, as expected, the position of the most probable charge ratio of the first and second strip around 1.5 indicates a magnitude of CS of around 67 %.

8.3.4. Performance of the μTPC Method

Figure 8.10 shows a typical residuals plot obtained with the μTPC method, and figure 8.11 compares the performance of the μTPC method for different settings of the VMM against the centroid and the CTP methods. The latter one is discussed in more detail in the next section. The best results in terms of resolution were achieved for the setup with a peaking time of 100 ns and the NL disabled. Quantitatively, the core resolution is 202 μm and the weighted resolution

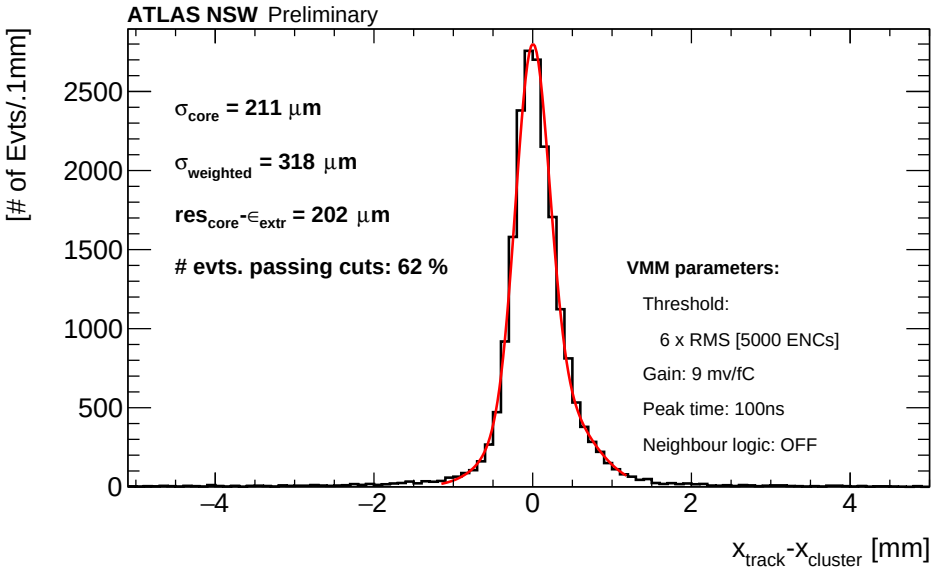

Figure 8.10.: Residuals for the μTPC reconstruction method.

is 312 μm. Switching on the NL worsens the resolution by 23 μm while switching to a peaking time of 200 ns adds 66 μm to the resolution. Enabling the NL at the higher peaking times leads to a core resolution of 285 μm. Similar trends can be observed for the weighted resolution, with a bigger impact of the NL, indicating increased tails in the residual distributions. These trends are in general expected. For the higher peaking time of the VMM, the precision of the peak detection and therefore the time resolution gets worse, leading to a worse performance of the reconstruction. It is expected that the NL worsens the spatial resolution as well, since it leads to the pick up of strips which only contain charge from CS rather than from actual ionizations. Those strips have a time measurement close to that of the neighbor strip, which distorts the fit in the μTPC method.

Figure 8.11 also indicates the ratio of events which pass all the selection criteria, i.e. the reconstruction efficiency. Using the best VMM parameters in terms of resolution, the reconstruction efficiency drops down to 62 %. Enabling the NL or increasing the peaking time raises the reconstruction efficiency up to 81 %. In case of the peaking time this can be explained by the fact that more charge is integrated. The drift time of the ions in the amplification gap is in the order of 150 ns [85]. Hence for a peaking time of 100 ns not all the charge is integrated and therefore the probability of strips not exceeding the threshold is higher compared to a peaking time of, e.g., 200 ns. Enabling the NL also increases the number of events passing the selection criteria, since strips below threshold are recovered.

Figure 8.12 shows the ratio of events passing the different filters applied in the μTPC method for the two scenarios of the NL being on or off and a peaking time of 100 ns. Without the NL it can be seen that 17.4 % of the clusters are not reconstructed since the HT is not able to find more

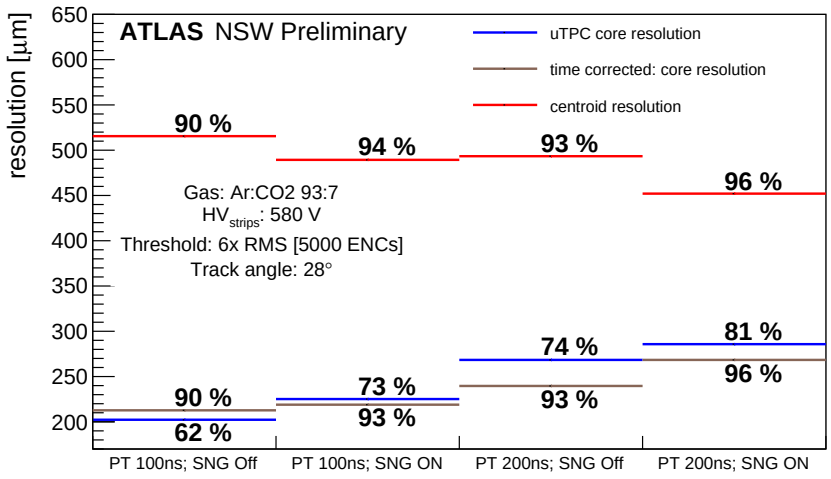

(a) Core resolution

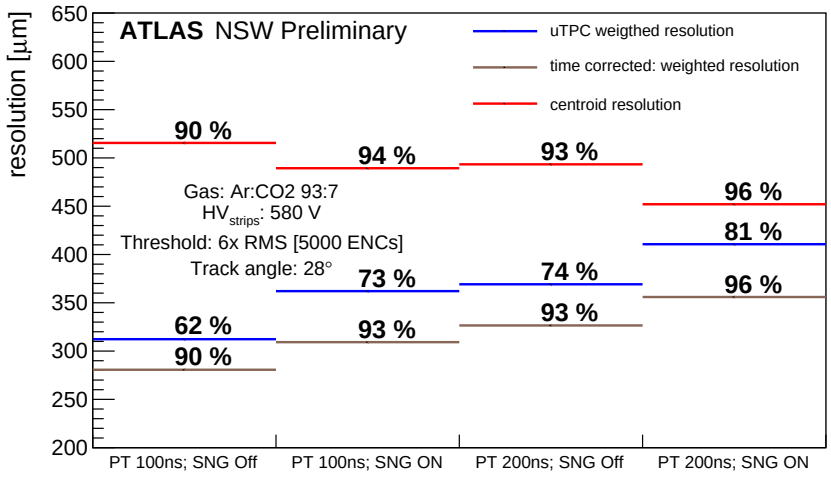

(b) Weighted resolution

Figure 8.11.: Comparison of the performance of the mean Cluster Time Projection method (brown) with the μTPC (blue) and centroid (red) methods for different VMM parameters. PT indicates the peaking time of the VMM, while SNG stands for the NL. The resolution values are extracted using a double Gaussian fit. The width of the narrow Gaussian is referred to as core resolution (a), while the weighted resolution is the mean value of the widths of the two Gaussians weighted by their integrals (b). For the centroid results the observed distribution was not a double Gaussian anymore, since the core was too wide to be separated from the tails. Therefore a fit with a single Gaussian distribution was performed leading to similar values for the resolution in both plots. The percentages indicated in the diagrams refer to the relative number of events passing all selection criteria (reconstruction efficiency).

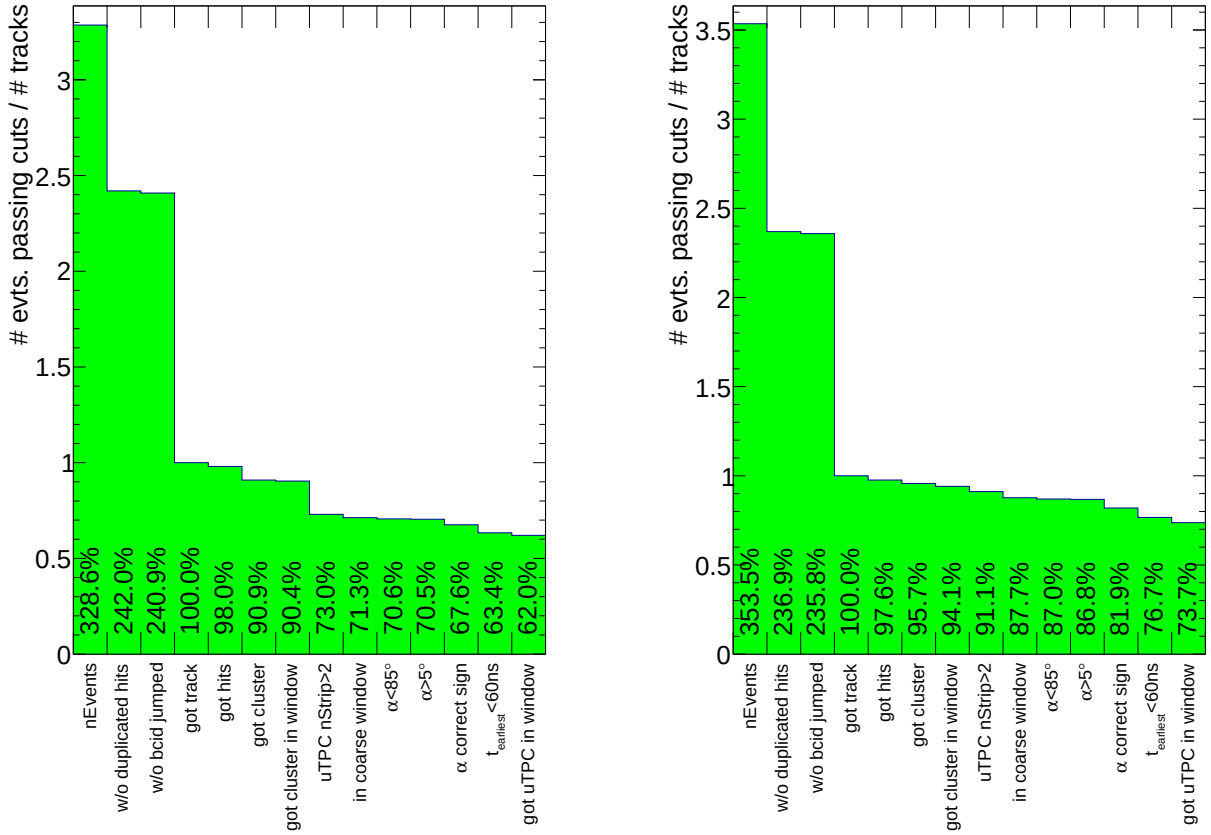

(a) Neighbor Logic Off

(b) Neighbor Logic On

Figure 8.12.: Efficiency of the individual selection criteria applied on top of one another from left to right for the μTPC method with the NL enabled (right) and disabled (left). The x axis displays the criteria which were applied in the μTPC method, while the y axis indicates the ratio of events selected. The ratio is normalized to 1 for the events where a track was found. The first bin indicates the total number of scintillator triggers. The two following criteria are related to malfunctioning of the readout electronics. The "got track" filter is applied based on the criteria discussed in section 8.1.1. While all previous selections were applied on a global level, the following criteria are used for each layer of the DUT individually. The "got hit/cluster" bin indicates the ratio of events where at least one strip or a centroid cluster with at least two hits was found, while the "got cluster in window" filter refers to the number of clusters reconstructed within 10 times the core resolution around position predicted by the external track. The following two selections are made after the HT was performed and require at least three hits being clustered by the HT, and that this cluster is in a coarse window of 20 mm around the predicted position. The following filters refer to the ones discussed in section 8.3.1. The last selection requires the reconstructed μTPC cluster to be within the 10 times the core resolution of the predicted position.

than two strips belonging to a line. With the NL enabled, only 3 % of the events are rejected by that filter. A similar effect is visible between the ratio of events with a reconstructed centroid cluster, consisting of at least two strips, while the ratio of events with at least one strip above threshold is compatible between the two settings. The loss of events in the other filter stages is also compatible between the different settings.
Both the resolution and the reconstruction efficiency are not in agreement with the expectations. For the resolution, values of about 100 μm were expected, while for the reconstruction efficiency values above 90 % are required for an acceptable tracking performance in ATLAS. The differences are due to multiple reasons, the main one being the high noise levels that were present in the test beam setup. As already discussed in section 7.3.3, thresholds of several fC had to be applied since the noise levels exceeded the theoretical limits significantly. The high noise levels lead to about 70 % of the strips being below the charge threshold.
The issue of the noise is mainly seen in the low number of events passing the selection criteria, especially the required number of strips in a cluster as discussed above. Not only were the noise levels high during the test beam, the non-final electronics also prevented a proper equalization of the thresholds of the individual channels. The problem of the noise could be fixed during the integration of the detectors by a dedicated task force such that the theoretical limits are now reached, resulting in a better performance in the final Micromegas modules compared to the test beam setup. The degradation of the resolution can be explained by high noise levels as well, since these reduce the number of strips included in the fit and therefore the precision. Besides the noise problem, also other influences on the resolution of the time measurement must be considered, one of which is CS. The CS does not only induce charge into the outer strips of the cluster which otherwise would not have received charge, it also biases the time measurement of the other strips towards the time measured on the central strips, since those tend to have more charge than the outer ones. A discussion of this effect is offered in the context of the simulation in sections 10.3 and 11.3.3.

8.4. The Cluster Time Projection Method for Inclined Tracks

As discussed before and illustrated in figure 8.11, the centroid method is able to reconstruct clusters from inclined tracks with a high efficiency, but a non-acceptable resolution of over 450 μm which is well above the required value of around 100 μm. Therefore more sophisticated methods are deployed to reconstruct the clusters, taking advantage of the drift time as additional information on top of the strip positions. One of those methods is the μTPC method, whose performance was discussed in the previous section. While the μTPC method is able to provide a core resolution of about 200 μm, still not in agreement with the requirements but well below the resolution from the centroid method, the reconstruction efficiency is worse. While the lower limit for the reconstruction efficiency is in the order of 90 %, the μTPC method shows values between 62 – 81 %. Therefore, the Cluster Time Projection method (see section 6.3.2 for technical details) was studied. Compared to the μTPC clusterization it additionally correlates the time value with

the charge measurement of each strip and uses an external estimate of the incident angle of the track. The idea of the method is to use the charge-weighted time of the strips in a centroid cluster and the estimate of the angle to project the cluster position to the center of the gas gap.

For the test beam, the angle between the detector and the particle tracks is fixed, therefore a simplified version of the method can be applied which serves as a proof of principle. This simplified implementation aims at correcting the dependency of the distance between the external track and the cluster position reconstructed with the centroid method (residual), as a function the charge-weighted strip time. This is achieved by a fit of the observed distribution. Compared to this data-driven approach which implicitly uses the fixed external angle, the actual CTP method relies on the incident angle, which can vary from event to event, to correct the cluster position. Figure 8.13a displays the residuals as a function of the cluster time for the test beam data. As expected, a linear dependency of the residuals on the cluster time can be observed which is even better visible in figure 8.13b, where the profile of the distribution is shown. The results from a linear fit performed in the central region of the profile are used to correct the residuals as a function of the cluster time.

Figure 8.11 compares the performance of the CTP method with the performance of the μTPC and the centroid methods. The spatial resolution of this clusterization is comparable with the one of the μTPC method, while it provides reconstruction efficiencies above 90 %. Like the μTPC method, the CTP procedure achieves the best resolution for smaller peaking times and the NL

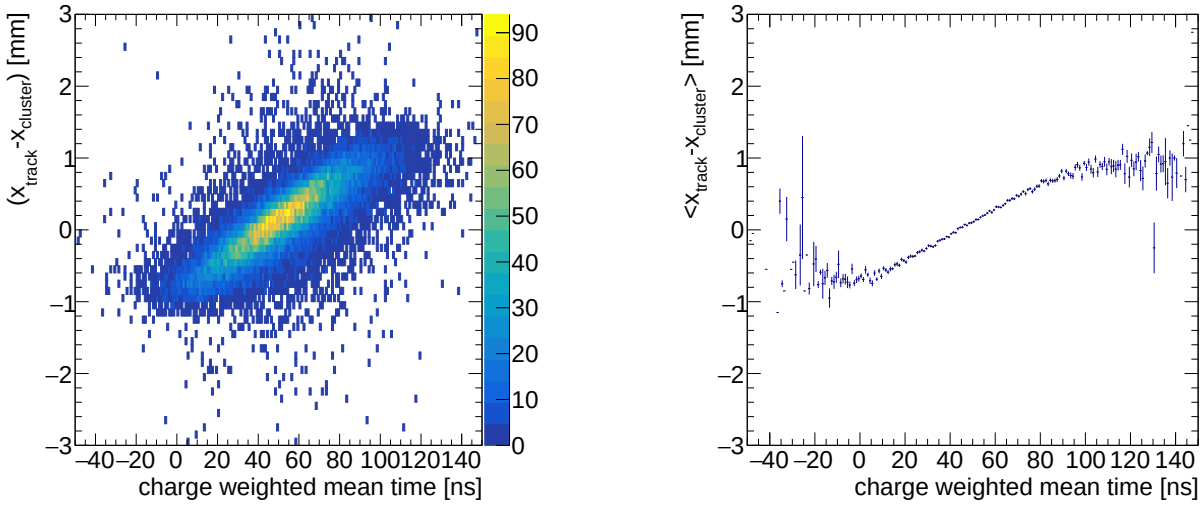

(a) Raw distribution

(b) Profile of the 2d plot

Figure 8.13.: Residuals as a function of the mean drift time of the strips of a cluster. The Cluster Time Projection method aims at making these residual distributions flat. Since in the test beam a fixed incident angle was used, the residuals were corrected by fitting the linear dependency between the mean cluster time and the residuals.

turned off. For longer peaking times it loses precision while it gains in terms of reconstruction efficiency. The good performance especially in resolution has two reasons. First, the incident angle of the particle is taken as an external parameter rather than being reconstructed with a small lever arm in the 5 mm thin gas gaps. This allows a much more precise determination of the angle, e.g. by fitting the track through all eight Micromegas layers in the NSW or even including the sTGC layers as well. The second difference to the μTPC method is the weighting of the time measurement by the charge. This could be a potential future improvement of the μTPC method, e.g. scaling the uncertainties of the strips in the final fit with the charge information.

9. Summary for the Test Beam Studies

In summer 2018 the performance of one of the very first Micromegas quadruplets from the series production, the SM2-M1 (DUT), has been studied in an extensive test beam. In the context of this thesis several major contributions have been made to the operation of the detector in the test beam, the calibration of the readout electronics, and the study of the detector performance under various conditions mainly focusing on the reconstruction of the clusters and their position for the case of inclined tracks.

Before the performance of the detector could be studied, several parameters of the over 2000 VMM channels deployed in the setup needed to be calibrated individually. This included a calibration of the charge threshold as well as time and charge conversion from ADC counts to physical units. Major contributions have been made to the time calibration where two different methodologies have been investigated, one data-driven method and one using the option to inject test pulses into the VMM channels. Eventually, the results obtained with the data-driven calibration were used for the studies of the detector performance and the readout system.

For those studies, two major goals were set. The first one was to verify that the VMM works on a full-size Micromegas quadruplet since it was the first time that this chip was used on a detector with the final dimensions. The second goal was to characterize the detector performance, namely the resolution and the reconstruction efficiency for inclined tracks as they are present in the NSW. The studies targeting the first goal were carried out on data where the DUT was set up perpendicular to the beam axis. As expected, a spatial resolution of about 100 μm was achieved in this configuration together with a reconstruction efficiency of well over 90 %. Considering these results, the readout of a full-sized Micromegas quadruplet by the VMM chip can be considered verified. Further studies that were carried out with the perpendicular tracks targeted the mitigation of the HV instabilities of the detectors in two ways. First, the performance of the DUT was studied for different ratios of Argon and CO_2 in the operation gas, where adding more CO_2 suppresses sparks resulting in a more reliable detector. It was proven that both the resolution and the reconstruction efficiency are stable as a function of the CO_2 fraction. The second measure to mitigate the instabilities is to reduce the voltage applied to the strips from the initially planned 600 V to 570 V which comes with a significant loss of gas gain, since the gain and the voltage are correlated in an exponential way (see equation 3.16). Nevertheless it was proven that with the new working point at 570 V the reconstruction efficiency for perpendicular tracks is still above 90 % for all layers, therefore the lowered voltage is considered validated.

The studies which were the main focus of this part of the thesis were targeting the scenario of inclined tracks as they are present in the NSW. In the data taken for these studies, the DUT was

tilted by 28° with respect to the beamline. At this angle the spatial resolution of the centroid method grows up to 500 μm, which is not acceptable for the use of the Micromegas detectors in ATLAS. Therefore more sophisticated methods, which make use of the information on the drift time of the strips are deployed to achieve a good spatial resolution also at high incident angles. In the scope of this thesis the performance of two such methods has been studied, namely the μTPC and CTP methods.

With the μTPC method, core resolutions of 202 – 285 μm have been reached, depending on the settings of the VMM. The reconstruction efficiency was determined to be 62 – 81 %, where the lower (upper) bound was measured with the VMM configuration which yields the best (worst) resolution. Both the resolution and reconstruction efficiency could not fulfill the expectations, which comprised a resolution of 100 μm and a reconstruction efficiency of above 90 %. These deviations have multiple reasons, the most important one being the high noise levels present during the test beam. Noise levels of up to 5000 electrons have been observed on the strips, consequently requiring a charge threshold of up to 6.2 fC. As shown in figure 7.12 this leads to 70 % of the strip signals being below threshold. This effect is visible in the distribution of the number of strips included in a μTPC cluster, which has a shoulder towards lower values. Since the μTPC is based on a fit of the track in the Micromegas drift gap, a reduced number of strips leads to a loss of information in the fit and therefore a worse position resolution. The reconstruction efficiency is impacted since the minimum number of strips required to fit a track in the drift gap is three. Oftentimes not enough strips with a signal above threshold lining up in the drift gap are present. It needs to be noted that the test beam studies were carried out with the beam position targeting the part of the Micromegas chamber where the copper strips are longest (about 1.7 m), leading to a high capacitance between the strips which subsequently leads to a high noise value. After the test beam, the noise level at this location could be reduced to its theoretical lower limit of 3300 electrons by a dedicated task force, through improving the grounding of the detector. Furthermore the setup in the test beam did not use the final version of the VMM but the pre-final one, namely the VMM3. Therefore it was not possible to equalize the threshold over all strips.

Another effect that impacts the resolution of the time measurement and therefore the resolution of all methods relying on the drift time information, is the sharing of charge between a resistive strip and its neighboring copper strip, an effect that increases with the strip length. A measurement of the CS using the ratio of charge on the outer strips of a cluster reconstructed with the μTPC method was carried out and yielded a CS ratio of about 67 %.

The second method to reconstruct clusters from inclined tracks is the CTP method. It takes an estimate of the external angle as an additional input parameter and then corrects the cluster position reconstructed with the centroid method using the charge-weighted mean time of the strips associated to the centroid cluster. Since the incident angle was fixed for the test beam, a simplified version was applied, which parametrized the correlation between the cluster time and the distance of a cluster to the external track. The cluster position was then corrected based on this parametrization. With this method a spatial resolution of 213 – 268 μm has been

achieved, compatible with the resolutions obtained with the μTPC method, but with much better reconstruction efficiencies of $90-96\,\%$. This high efficiency can be explained by the fact that in contrast to the μTPC method, the CTP method does not need to reconstruct the slope of the track in the drift gap but only the intercept and therefore can run on even a single strip.

Part III.

The Micromegas Detectors within the ATLAS Offline Software

The offline software of ATLAS, called athena, is the central framework for the simulation and reconstruction of events. An introduction to athena was already given in section 4.2.7. In the course of this thesis several components of the software related to the NSW have been developed or improved. New functionalities have been added to the Micromegas digitization in order to better describe the response of the detector and the readout electronics attached to it. Furthermore several parameters of the digitization algorithms have been tuned in order to match the data taken during the commisioning of the final detectors. These developments are discussed in chapter 10. For the reconstruction, multiple components have been introduced within the scope of this thesis, the most significant one being the different clusterization algorithms. Chapter 11 discusses their implementation and performance. Also the other improvements of the reconstruction which were part of this thesis are described. Finally chapter 12 summarizes the contributions that have been made.

10. Micromegas Digitization

In this chapter, the Micromegas digitization is discussed. It refers to a set of algorithms whose purpose is to transform the energy deposits in the individual gaps created by the GEANT4 simulation, covered in section 4.2.7, into actual detector-like signals. This chapter first summarizes the existing digitization algorithms, which is followed by a discussion of the improvements that have been developed in the scope of this thesis. Afterwards the output of the digitization is compared to signals recorded by the detector during commissioning. In this way, the default parameters for the digitization are derived which will be used for the event simulation for the upcoming data taking period.

10.1. Introduction to the Micromegas Digitization

The Micromegas digitization consists of two major parts: the simulation of the physics of the detector in terms of charge creation, transportation, and multiplication, followed by the simulation of the readout electronics. Both parts are introduced below.

10.1.1. Simulation of the Detector Physics

The creation, transport, and multiplication of charge in gaseous detectors according to the principles discussed in chapter 3 is usually simulated by a dedicated software called Garfield++ [86]. Inside Garfield++, the motion of each particle is calculated by solving its equation of motion for a number of discrete time steps. Since this is very expensive in terms of CPU usage, it is not feasible to use Garfield++ in the full digitization of the Micromegas, where billions of events need to be processed and each of which potentially contains multiple muons traversing the detector and ionizing the gas along the way. Instead, the digitization relies on distributions for relevant parameters (e.g. numbers of ionizations, diffusion, or gas gain) which have been obtained prior to the simulation of the muon events by dedicated Garfield++ simulations of minimum ionizing muons in a Micromegas-like setup. Details for these studies are given in [71], including a discussion of the distributions of parameters used in the digitization.
Figure 10.1 depicts the different steps of the simulation of the detector response. A straight line is projected into the drift gap, taking the location and direction information of the charge deposit in a single gas gap from the GEANT4 simulation. Along this line, the primary ionizations are created with an average of 16.04 interactions per mm [71]. For each primary ionization, the number of secondary ionizations is taken from a histogram, which was filled from the Garfield++ simulations.

All electrons originating from primary and secondary ionizations are then displaced to account for diffusion. For the longitudinal component, the displacement is realized by generating a random number according to a single Gaussian distribution with a mean of zero and a width depending on the diffusion coefficient and the drift distance. For the transverse component the underlying distribution, σ_{tr}, is given by the sum of two Gaussians as follows:

$$\sigma_{\mathrm{tr}}(x) = \exp\left(-\frac{x^2}{(\mathrm{D}_{\mathrm{tr}} d)^2}\right) + 0.001 \exp\left(-x^2\right), \tag{10.1}$$

where D_{tr} is the diffusion constant for the transverse diffusion, d is the height above the mesh, and x is the random number to be obtained. The double Gaussian distribution has been chosen in order to match the shape of the transverse displacement of an electron moving through the drift gap as obtained in the studies with Garfield++. In the next step, each electron is projected onto the mesh, taking into account the Lorentz angle due to the magnetic field. The drift time is obtained assuming a fixed drift velocity multiplied by the distance of the projection. The electron multiplication in the amplification gap is modeled by drawing a random number from a Polya distribution and assigning that number as an effective charge to the initial electrons. Finally, the electrons with their effective charge are associated to the strip corresponding to their position after the projection. For each strip, the assigned electrons are stored in a histogram using time bins of 0.01 ns. Before this information is passed on to the simulation of the readout electronics, the CS between the strips is modeled for each time bin.

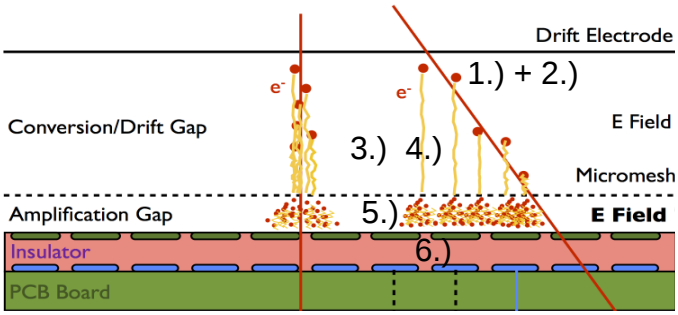

Figure 10.1.: Illustration of an ionization event in the Micromegas detector with the individual steps of the simulation in the physics modeling enumerated. First (1), the primary ionizations along the track through the gas gap are created. In step 2 the number of secondary ionizations for each primary ionization is obtained as a random number drawn from a distribution derived from prior Garfield++ simulations. Steps 3 and 4 consist of modeling the diffusion for each electron and propagating it to the mesh, which determines the drift time. In step 5, the charge avalanche is produced in accordance with the Polya distribution. In the final step 6, the charge induced on the copper strips is determined taking CS into account. Figure modified from [60].

10.1.2. Simulation of the Electronics Response

For the simulation of the response of the readout electronics, the time series of charge on each strip, obtained from the associated electrons in the step before, is folded with the so-called *shaping function* (also *transfer* or *response function*) of the VMM chip, which gives the response of the shaping amplifier to a charge deposit at a given time t. From this, the height and position of the first peak are determined, and the strip signal is kept if the peak height is above threshold and discarded otherwise. Also the NL of the VMM, which refers to strips with a signal below threshold being read out if one of their neighbor signals is above threshold, can be activated in the implementation of the VMM in the digitization. Aside from the "time at peak" also the "time at threshold" mode and the trigger output of the VMM are implemented in the digitization. Since the simulation of the VMM is part of this thesis, further details will be given in the following sections.

10.2. Improvement of the Micromegas Digitization

In the scope of this thesis several key developments could be made to the Micromegas digitization. Major improvements include the implementation of the VMM shaping function, a strip-length-dependent threshold, the thorough simulation of CS between strips, and the contributions made concerning the technical performance of the different algorithms.

10.2.1. Implementation of the VMM Shaper

Originally the transfer function of the VMM shaping amplifier, called *shaper*, was based on a simple RC shaper. It was found, however, that changing the integration time of the shaping amplifier, referred to as peaking time, with the model of the shaper implemented so far, did not preserve the charge measurement but instead scaled the measured charge up by a factor between 2.5 (for a peaking time of 100 ns) and 21 (200 ns). Therefore it was decided to implement the actual transfer function of the VMM shaper into the digitization.

The shaper of the VMM is of third order and has one real and two conjugate poles. The transfer function was kindly provided by George Iakovidis who is one of the developers of the VMM. In the time domain it can be expressed as follows:

$$T_i(t) = q_i\,\alpha^3\,P_0\,|P_1|^2\,\left(K_0\,e^{-(t-t_i)\,P_0} + 2\,|K_1|\,e^{-(t-t_i)\,\Re(P_1)}\,\cos\left(-(t-t_i)\,\Im(P_1)\,\arg(K_1)\right)\right), \tag{10.2}$$

where q_i is the effective charge of charge deposit i, t_i denotes its time, and $P_{0,1}$ stands for the poles. The numeric values of the constants α, $K_{0,1}$, and $P_{0,1}$ can be found in the appendix, table A.1. The peaking time of the shaper is contained in the parameter α. The simulated charge deposits per strip are binned in time and can either come from actual gas ionizations or be produced via

CS between strips. The response of each strip to multiple charge deposits is given by:

$$T(t) = \sum_i T_i. \tag{10.3}$$

Figure 10.2 shows the response of the shaper and its derivative for an exemplary event with two charge deposits on a single strip that are close-by in time, which can be the result of CS among strips. The main deposit with an arbitrary effective charge of 10^4 electrons is placed at a time $t = 50\,\text{ns}$. The second charge cluster is chosen to be 30 % of the first one following the default assumption on CS in the Micromegas digitization. It is located at $t = 0\,\text{ns}$.

The relevant quantities to be derived from the shaper response are the peak height corresponding to the collected charge and its time. In case multiple peaks are present, the first one above threshold is taken. The peak finding algorithm is implemented based on locating the root of the derivative shown on the right side of figure 10.2. Since the peak finding runs with a precision of 0.1 ns for each channel that collected charge, a simple scan of the derivative to identify the root would take too much computing time. Therefore some properties of the response function are exploited to reduce the CPU time on finding the maximum. First of all the scan of the derivative does not start at the time of the earliest charge deposit, but only at 80 % of the peaking time after the first deposit, given that no maximum is expected earlier than that. From this point onwards the search for the root of the derivative is performed with a step size of 0.5 ns. Finally the rough

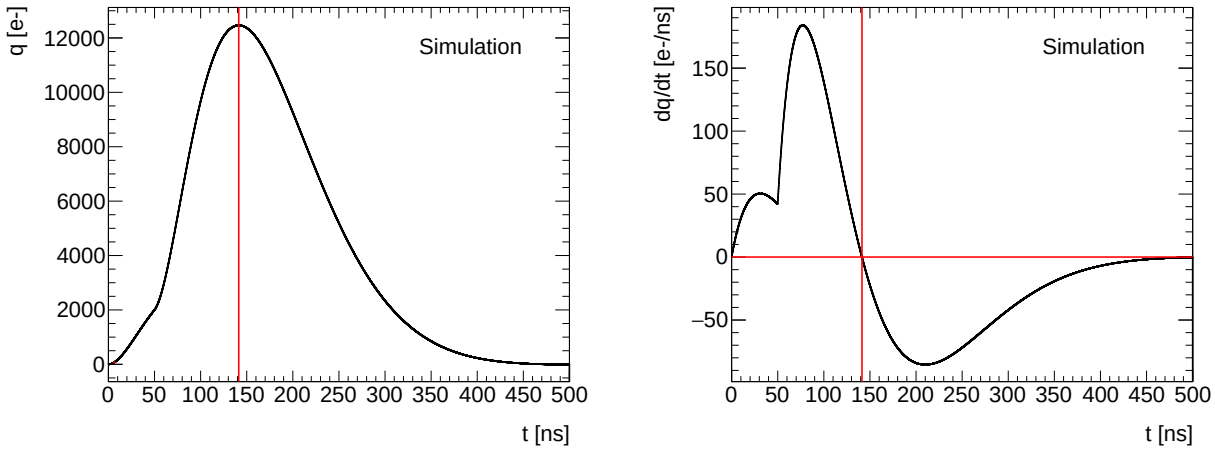

(a) VMM shaper response

(b) Derivative of the VMM shaper response

Figure 10.2.: Response (a) and its derivative (b) of the VMM shaper to two close-by charge clusters. The main deposit with an effective charge of 10^4 electrons is placed at a time $t = 50\,\text{ns}$. The second charge deposit is chosen to be 30 % of the first one according to the default assumption on CS in the Micromegas digitization and is located at $t = 0\,\text{ns}$. The peaking time of the VMM shaper used for these plots is 100 ns.

location of the maximum, that has been found in the previous step, is analyzed more precisely by a second iteration with a step size of 0.1 ns applied in a window of ± 1 ns around the previously found peak position. Once a peak is identified, its height is compared to the charge threshold, and if it exceeds the threshold, the time and peak height are stored and the next channel is processed. If the peak height is below the threshold, the search for another zero-crossing is continued using the procedure described above.
The VMM also allows for a measurement of the time at which the response function exceeds the charge threshold rather than the maximum. This was implemented in the simulation in the following way: A coarse scan of the response function is performed with time steps of 1 ns until 90 % of the peaking time, indicating the position of a first possible peak. If a threshold crossing was identified, its position is refined by a scan with a step size of 0.1 ns around the location found in the previous step. If no threshold crossing was identified so far, the rest of the VMM response function is sampled with a time step of 0.1 ns. In order to guarantee a high performance of the electronics simulation, only signals of strips are processed in the aforementioned way if the sum of all charge deposits on that strip is above threshold. If not, the strip is not processed at all.
The digitization software is written in a way that allows the user to specify a number of parameters, for example the peaking time of the VMM or if the NL is used. The peaking time is part of the VMM transfer function, but other than its impact on the transfer function, it also affects the total charge collected due to the ion drift times in the amplification gap. Since it would be too CPU intensive to process the drift of the ion in the amplification gap, called *ion tails*, with the VMM simulation, a different approach is taken to consider them. The maximum ion drift time in the amplification gap of the Micromegas is about 150 ns [85]. Therefore any peaking time above 150 ns will integrate over the full charge. For any peaking time below 150 ns, it is assumed that the total integrated charge is only a ratio of the peaking time over 150 ns of the full charge. This is implemented by scaling the effective charges put into the VMM simulation by this ratio. The other VMM parameter that is implemented in the new VMM simulation is the NL. When enabled, strips with a signal below the threshold are still read out if the charge on one of their neighbor strips is above the threshold. This is implemented by running the VMM simulation a second time with the threshold of the strip whose signal is too low being set to a negligible level, such that the strip can be read out in this iteration.
One relevant study that can be conducted with the simulation of the shaper is to investigate the impact of multiple charge clusters at different times on the position of the peak in the response function. As shown in figure 10.2, a second charge cluster on a strip does not necessarily create a second peak in the response function if the charge clusters are close enough, but it will have an impact on the time at which the maximum occurs. In the following a typical scenario for Micromegas will be studied, with a main charge deposit of 10^4 electrons induced at a time of 20 ns and an additional fraction of that charge induced at a time 0 ns, e.g. stemming from CS with neighboring resistive strips. Figure 10.3 shows the position of the maximum minus the peaking time as a function of the fraction of the smaller charge with respect to the main one. It can be seen that with an increased fraction of charge, the measured time gets skewed more and

more towards the position of the smaller charge. This effect is also visible in the drift time spectra of the Micromegas discussed in section 10.3.6.

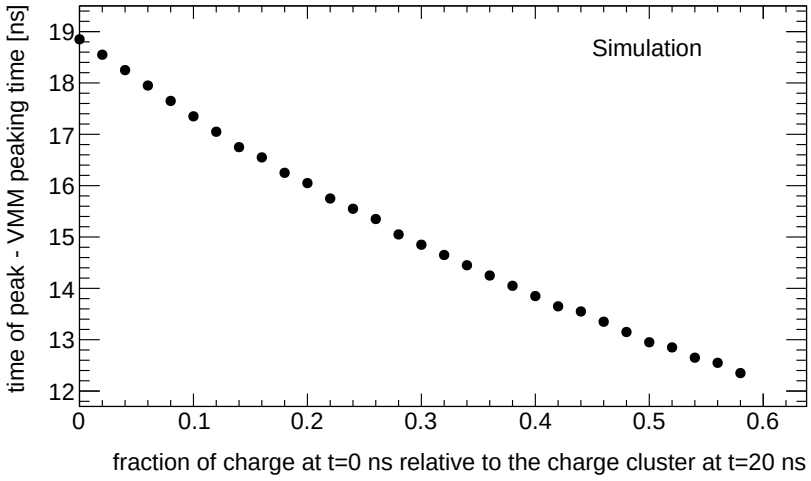

Figure 10.3.: Impact of CS on the VMM time measurement. The plot is based on a scenario where one main charge cluster of 10^4 electrons is placed on a strip at a time of 20 ns and a fraction of that charge, stemming from CS with the neighboring resistive strip, is located at a time of 0 ns. The plot shows the location of the maximum minus the peaking time as a function of the ratio between the two charges.

10.2.2. Strip-Length-Dependent Threshold

Especially for inclined tracks where the charge is distributed on many strips, it is very important to have a good understanding of the charge threshold applied by the VMM. Figure 10.4 shows the measured RMS of the baseline (see section 7.3.3 for the procedure to determine the RMS), referred to as noise, of a Micromegas double wedge at the integration site with the final detectors and electronics installed, as a function of the strip number. Since the strip length and therefore the capacity between the strips increases with the strip number, the threshold applied to each channel is determined as x times the noise, where x is referred to as the threshold scale factor. The default value used during the tests in the integration of the real detector was 9, but also studies with different values are ongoing in order to optimize this threshold scale factor. In the Micromegas digitization two models of thresholds are available. The default method (already present before this thesis) is to apply a fixed threshold to all strips independently of their length. For this configuration, the absolute value for the threshold was adapted to the real detector conditions as discussed later.
In the scope of this thesis, a second model for the threshold was implemented, rendering the actual threshold dependent on the strip length. According to the measured threshold depicted in figure 10.4, a noise level of 1000 electron ENC was assigned to the shortest strip in the simulation

and of 2600 electrons to the longest strip. The noise on the other strips is then derived by a linear approximation between these two extremal points. The value for the threshold is obtained by multiplying the noise with the configurable threshold scale factor, using 9 as the default value. The algorithm that implements the strip-length-dependent threshold also makes it very easy to plug in thresholds as measured separately for each strip in the future, should it be needed. This newly developed model has now become the default in the digitization.

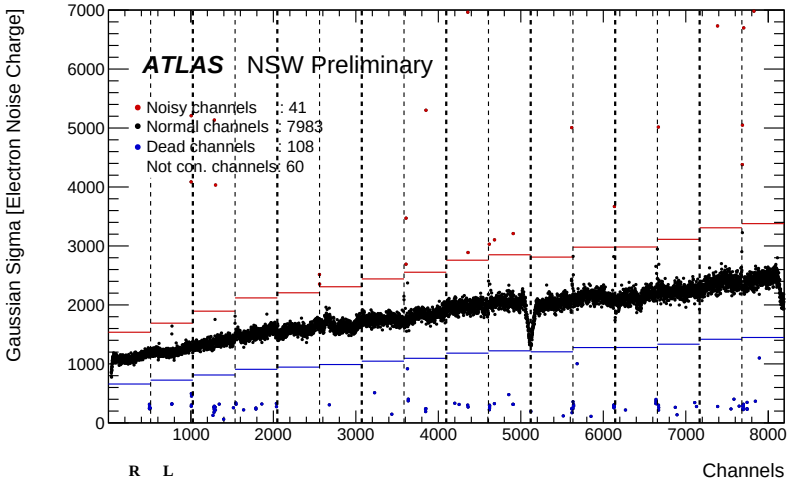

Figure 10.4.: Micromegas noise levels as a function of strip number measured for one layer of a sector during the integration of the detectors. The strip length increases with the strip number and so does the capacity between strips. Therefore the noise on the detector increases with the strip length. The vertical dashed lines indicate the separation between different MMFE8 front-end boards. The horizontal red and blue lines respectively indicate the upper and lower boundaries of the range within which the noise per channel is considered unproblematic. Strips above the limit are called noisy strips, while strips below are referred to as dead channels. Figure taken from [2].

10.2.3. Charge Sharing between the Strips

As already discussed for the test beam results in section 8.3.3, the Micromegas show high CS between strips due to the way they have been constructed combining a resistive layer and long copper strips, which leads to high capacitive coupling between them. This effect has significant impact on the time-of-arrival measurement of the single strips and therefore on time-based reconstruction methods like the μTPC method. Hence it is important to model this effect well in the simulation.

Figure 10.5 shows a sketch of the mechanism of CS. The total charge q_{tot} received by a resistive strip is symmetrically shared among the main (i), the neighboring ($i \pm 1$), and the next-to-

neighboring copper strips ($i \pm 2$) as follows:

$$q_{tot} = q_i + q_{i\pm1} + q_{i_\pm 2} = q_i + 2c_1 q_i + 2c_2 q_i, \tag{10.4}$$

where q_i stands for the charge on the central copper strip after the simulation of CS and $c_{1/2}$ is the CS factor for the neighbor and next-to-neighbor copper strip, respectively. Solving the equation for q_i leads to:

$$q_i = \frac{q_{tot}}{1 + 2c_1 + 2c_2} = \frac{q_{tot}}{f}, \quad \text{with} \quad f := 1 + 2c_1 + 2c_2. \tag{10.5}$$

Using this equation, CS is implemented by dividing the total charge on the main strip by the factor f, which gives the charge on the central copper strip and then assigning the corresponding fractions of charge to the neighbor strips. Charge sharing is applied to the results of the simulation of the detector physics before the VMM simulation. Therefore the procedure is applied to the time-binned charge deposits on each strip, so the actual impact of the shared charge on the peak height and position of the VMM is simulated.

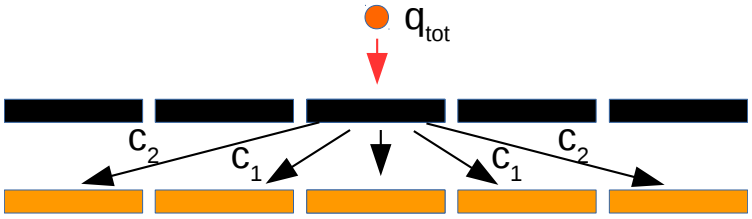

Figure 10.5.: Illustration of CS in Micromegas. The total charge deposit on a resistive strip, shown in black, is transferred to the underlying copper strips, shown in orange, via capacitive coupling. To give a better overview, the insulating layer of Kapton between the resistive and the copper strips is omitted. While the majority of the charge is transferred to the copper strip just below the resistive strip, a fraction of the charge is also coupled to the neighbor and next-to-neighbor copper strips. Their fractions are denoted by c_1 and c_2 respectively.

10.2.4. Improvement of the Technical Performance

Along with the improvements on the simulation of the detector and the electronics response, also the technical performance of the Micromegas digitization has been enhanced in the scope of this thesis. While simulating events in the environment expected for the HL-LHC, it was found that the Micromegas digitization takes a factor of 30 times more processing time per event compared to the digitization of the pixel detector, which otherwise is the largest CPU consumer in the digitization of ATLAS. This is not acceptable, since the analysis of ATLAS physics data relies on billions of simulated events. Following these findings, the CPU time consumption of the different parts of the Micromegas digitization were investigated and two major contributions were identified. The first one accounting for about two thirds of the total CPU time was found

in the simulation of the electronics response. The previous VMM simulation was sampling the full shaper response in time steps of 0.1 ns in a range of about 600 ns. To remedy the situation, a different approach was taken for the new VMM simulation and irrelevant regions in the shaper response pattern were excluded from the iterative searches for the response peak and threshold crossing, as discussed previously in section 10.2.1. Furthermore, the evaluation of the shaper response itself (see equation 10.2) has been optimized by precalculating all parts of the equation that are not depending on the strip charge or time before the event processing.

The second large contribution to the processing time was identified to stem from the generation of random numbers according to the sum of two Gaussian functions for the longitudinal diffusion following equation 10.1. They were generated using *ROOT TF1* [87,88] functions which internally employ the method of inverse transform sampling. These random numbers were drawn for every electron created in the drift gap separately and since the width of the Gaussian depends on the position where the electron was created, this included a numerical integration of the probability density function for each electron. The solution to this can be summarized as follows: first, the normalization factors for both Gaussians as well as a uniform random number y between zero and the sum of the two normalization factors are determined. If y is smaller than the normalization of the first Gaussian, a random number x is determined according to the first Gaussian, otherwise according to the second one. This reduces the problem of drawing x from a custom function for each electron to determine two random numbers from well-known distributions for which optimized random number generators exist, e.g. in the CLHEP library [89]. With this change, the CPU time consumption for random number generation per electron was brought down to almost zero.

The structural improvements related to these two main CPU consumers and additional minor computational issues resulted in a significant reduction of the CPU consumption by a factor of 120, such that the Micromegas digitization now requires roughly a quarter of the processing time of the Pixel digitization, making it compatible with the requirements.

10.3. Optimization of the Micromegas Digitization Towards a Realistic Detector Response

In this section, the impact of optimizing the Micromegas digitization parameters on certain quantities, e.g. the sum of electrons in a cluster, the drift time, or the number of strips in a cluster, is discussed, whose goal it was to match the output of the digitization to cosmic ray data taken with the detectors during their integration. First, the cosmic ray test stand used to verify the general functionality of the Micromegas detectors is briefly introduced. Then the default setup of the simulation in general and more specifically the possible configurations of the digitization are discussed, followed by a comparison of data and simulation output for different sensitive quantities.

10.3.1. The Micromegas Cosmic Ray Test Stand

Figure 10.6 shows the setup of the cosmic ray stand used to test the final Micromegas *double wedges* (DW), which are the Micromegas part of a NSW sector. In the middle the DW can be seen, consisting of four Micromegas quadruplets equipped with the final electronics cards using the final version of the VMM, the VMM3a. In total, a DW consists of 8 detector layers with 8192 strips per layer. To trigger on cosmic rays, which pass through the Micromegas detectors, two scintillators are placed on top of the DW. The event reconstruction in this setup is based on the centroid clusterization method applied to the active strips of the individual layers followed by a reconstruction of the track relying on all eight layers of the DW. From the reconstructed track, the incident angle of the muon is determined. Furthermore the track is used for efficiency studies of individual layers. The standard run configurations employed in this setup are a VMM peaking time of 200 ns and a threshold of 9 times the measured noise level. As discussed before and shown in figure 10.4, the noise level depends on the strip length, and the theoretical limit that is reached in this test stand is between 1000 and 2600 electrons giving thresholds between 9000 – 23 400 electrons. The difference to the theoretical lower limit of the noise of 3300 electrons mentioned in the test beam section can be explained by the different readout electronics that were employed. If not stated otherwise, the NL of the VMMs was disabled in the following studies.

Figure 10.6.: Picture of the Micromegas double wedge cosmic ray test stand, kindly provided by [90].

10.3.2. General Setup of the Simulation

This section shortly summarizes the characteristics of the simulated events that the studies below relied upon. The simulation was done using the ATLAS setup with both NSWs replacing the current Small Wheels, referred to as the *symmetric geometry*. Each event contains two single muons created at the interaction point, one having a direction with a positive η component and one with a negative one, leading to one muon per NSW per event. The momentum of the muons is randomly chosen from a flat distribution between 10 GeV and 100 GeV. Furthermore, the full ϕ range is used. The absolute value of η for the generated muons ranges between 1.0 and 2.7. Both the $|\eta|$ and ϕ directions are generated as random numbers following a flat distribution. With this choice of $|\eta|$ the whole NSW, with a range of $1.3 \leq |\eta| \leq 2.7$, is covered. For the studies of the basic detector quantities and also the studies for the performance of the different reconstruction methods shown later, the magnetic field is switched off in the simulation, allowing for better comparability with data from the cosmic test stand. A detailed discussion of the impact of the magnetic field can be found in section 11.4. The main reason for performing the simulation without the toroid magnetic field is to avoid the distortion of the movement of the electrons in the drift gap by the Lorentz force, which would have a significant impact on the obtained cluster size, all timing measurements, and the reconstructed positions. The different parameters of the digitization are discussed in the following section and are summarized in table 10.1. If not stated otherwise, the default parameters were used for the simulation. For each configuration shown below, 10^5 events were simulated and reconstructed with the centroid method.

10.3.3. Default Parameter Settings of the Micromegas Digitization

The Micromegas digitization has several configurable parameters which are summarized in table 10.1 together with their default values. They can be divided into two categories: parameters related to the detector response and those related to the electronics response.

Detector parameters: For the detector response, an average gas gain of 8000, referring to the corresponding value in the Polya distribution (see equation 3.17), was chosen. The default value for CS to the next neighbor is 0.3 while for the next-to-next neighbor it is 0.09. This amount of CS is a mean value applicable to the whole detector and therefore smaller than the numbers reported for the test beam (see section 8.3.3), because there the measurements were performed at a fixed strip length close to the maximum one. In the future, it is planned to scale the amount of CS as a function of the strip length, since it has a big impact on the measurement of the drift time of the detectors as discussed in section 10.3.6.

VMM parameters: For the electronics simulation, the NL is switched off by default, since this is the most likely option for the operation of the detector. The default value for the VMM peaking time is 200 ns. As discussed in section 10.2.2, two options are available for the simulation of the VMM charge threshold: one having a fixed threshold over the full detector and one with a

strip-length-dependent threshold. For the simulation of events in ATLAS, the default model is the one with the strip-length-dependent threshold with a threshold scale factor of 9. However this mode is not suitable for making comparisons between the data taken in the cosmic ray test stand and the simulation, since cosmic muons do not originate from a single fixed interaction point by which one could align the incident angle to the strip number and subsequently derive a threshold. Therefore the studies presented below use a fixed threshold value of 15 000 electrons, representing the mean threshold of all strips in the cosmic ray test stand.

Parameter	Default value
Charge sharing 1st neighbor	0.3
Charge sharing 2nd neighbor	0.09
Gas gain	8000
Peaking time	200 ns
Neighbor logic	Off
Fixed threshold	15 000 electrons
Threshold scale factor	9
Use fixed threshold	False

Table 10.1.: Configurable parameters of the Micromegas digitization and their default values. The first three parameters are part of the detector response simulation, while the remaining ones are settings of the VMM. The last option allows to decide between the use of a strip-length-dependent threshold (true) or a fixed one (false).

10.3.4. Optimization of the Gas Gain

One of the key parameters in the digitization is the gas gain which can be tuned by changing the mean value of the Polya function (see equation 3.17). One variable that is sensitive to the gas gain is the total sum of detected charge of all strips that belong to a cluster, referred to as *cluster charge*. Figure 10.7 shows the simulated cluster charge as a function of the muon incident angle compared to the data taken with cosmic muons. The simulation was carried out with the default value of 8000 for the gas gain. It can be seen that the cluster charge distributions agree with each other for sector A16, while for A08 the simulation is slightly overestimating the cluster charge. However it is still well within the expected fluctuation of the gain, which can be heavily influenced by, e.g., how precisely the detector is manufactured. Already a deviation of 5 μm from the nominal width of the gas gap can introduce a change of the gain of about 25 % [42]. Also, it can be observed that the NL of the VMM recovers some of the cluster charge which is otherwise lost due to strips with signals below threshold.

10.3.5. Dependence of the Cluster Width on Digitization Parameters.

Another important parameter to assess the performance of the Micromegas detectors is the size of the strip clusters, i.e. how many active strips are included in a cluster. A correlated quantity

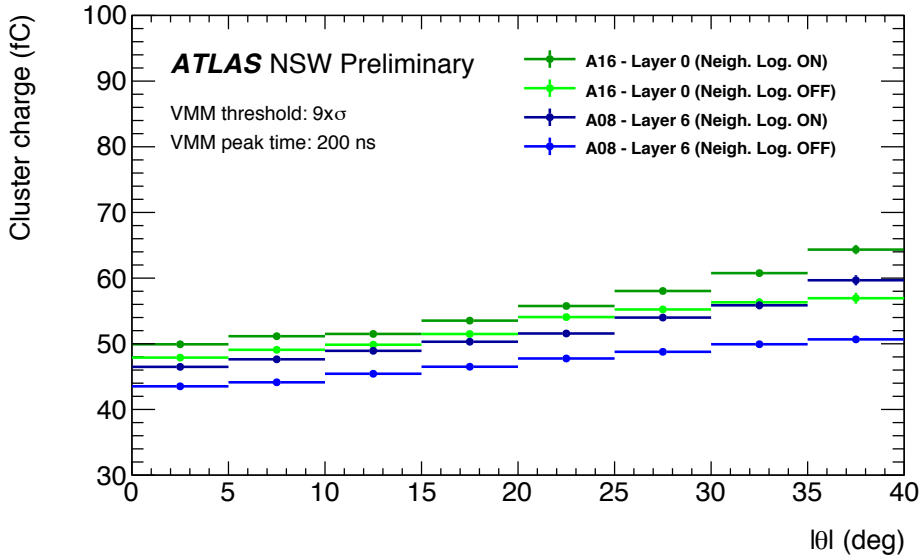

(a) Data

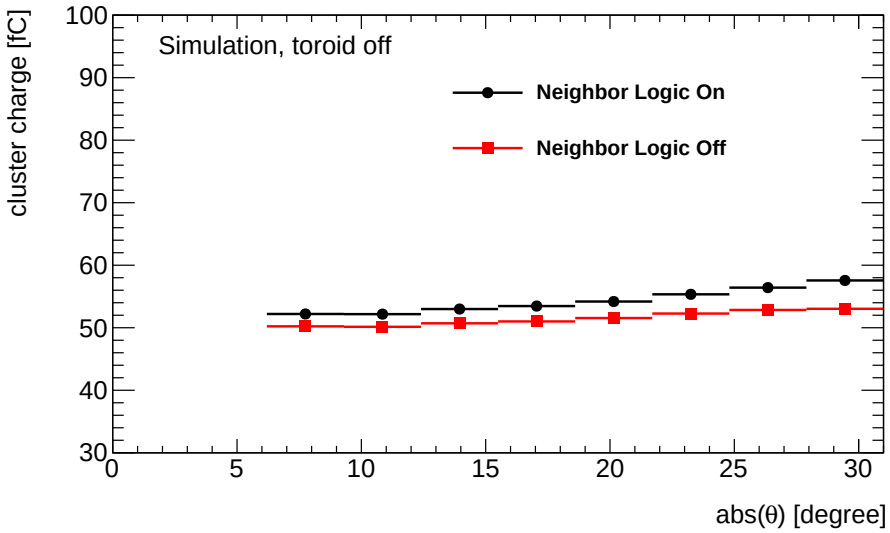

(b) Simulation

Figure 10.7.: Comparison of the cluster charge as a function of the muon incident angle θ between cosmic muon data (a) and the simulation (b) with the VMM NL being switched on or off. The data was recorded with the Micromegas detectors during their integration, using cosmic muons as a source for ionizing radiation. The plot in subfigure (a) is modified from [2].

is the width of the cluster which is the sum of active strips and inactive strips in between the active strips of a cluster. Figure 10.8 shows the cluster width for different configurations of the

digitization, i.e. threshold, CS, and the status of the NL. The structure of this kind of figure is shortly discussed since it is used for several figures in the following. The subfigures in the top (bottom) row correspond to the mean value (upper limit) of the threshold applied in the cosmic data taking with an actual value of 25 000 electrons (25 000 electrons). In the subfigure on the left, the VMM neigbor logic is disabled while it is enabled for the plots on the right. The different amounts of CS are indicated by the color of the markers. Red (green) indicates the default value (upper limit) of CS while the black markers refer to the hyperthetical case of no CS which is deployed to examine the general impact of it.
While figure 10.8 contains simulated events, figure 10.9 displays the cluster width for the cosmic data for different settings of the NL. From the simulation it can be seen that, as expected, both CS and threshold settings have a big impact on the cluster width. Enabling CS substantially increases the width of the clusters, since at both ends of the cluster the strips which did not collect charge before now have a signal induced by CS with the resistive strip, which exceeds the threshold. This effect is more pronounced at lower incident angles, where the charge is collected on fewer strips leading to a higher strip charge and subsequently to a higher signal induced by CS. Comparing the different thresholds in the neighbor-logic-off-scenario, the mean cluster width as a function of the incident angle without any CS flattens out at high angles since the outer strips of the clusters start to be below the threshold. For the higher threshold, this effect is also visible with CS being enabled, while at low thresholds it is not the case. Enabling the NL mitigates this problem since the outer strips of a cluster are recovered. Compared to the data, all the curves with CS enabled show a bigger cluster width for the simulation at low angles. At high angles, the lower threshold curves match well with the data. The distributions for the higher threshold slightly underestimate the cluster width.

10.3.6. Dependence of the Drift Time Distribution on Digitization Parameters

This section discusses the impact of CS, the charge threshold, and the NL on the drift time distribution. First a basic understanding of the shape of the drift time distribution needs to be established. Naively one would expect that the drift time is distributed according to a flat probability density function since the ionizations occur uniformly along the track. With the drift velocity of 47 μm/ns and a thickness of the drift gap of 5 mm, the width of the flat distribution should be in the order of 105 ns. But this naive guess does not take into account the effect of the strip-like segmented readout electrodes illustrated in figure 10.10. The observed drift time distribution for the case of no CS and NL disabled is shown in figure 10.10b in black. While the central part of the spectrum follows the naive guess of a flat distribution, peaks can be observed at low and high drift times. As depicted in figure 10.10a strips in the center of a cluster receive charge from ionizations which on average occur in the middle of the strip, and thus, the square-like part in the center of the drift time distribution. For the outermost strips the ionizations cannot happen centrally above the strip anymore since the initial particle leaves the gas volume. This leads to an asymmetric time distribution on the outer strips, subsequently causing the peaks one

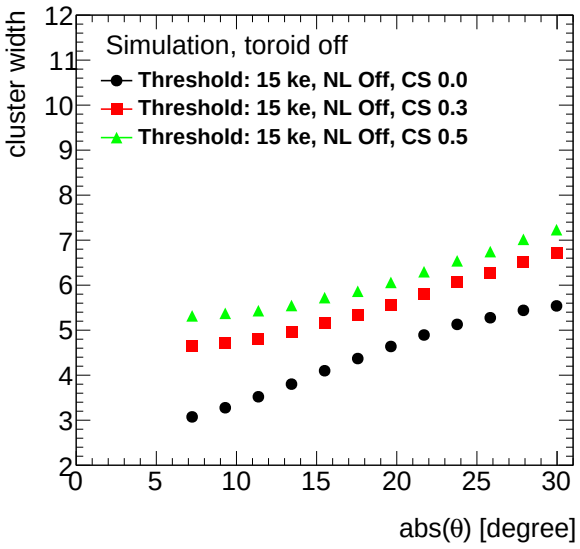

(a) Threshold 15 000 electrons, NL off

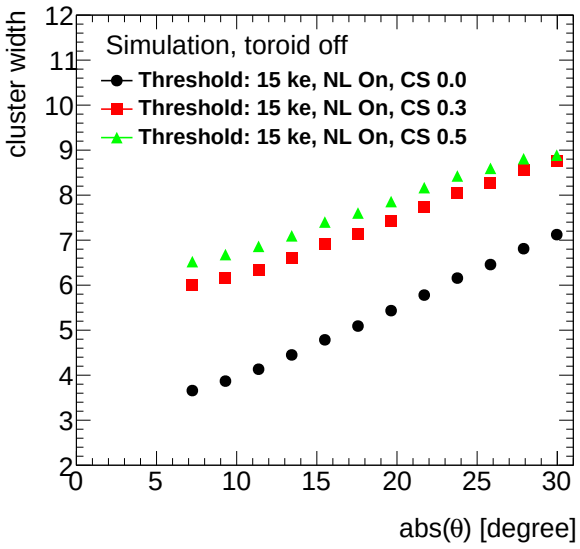

(b) Threshold 15 000 electrons, NL on

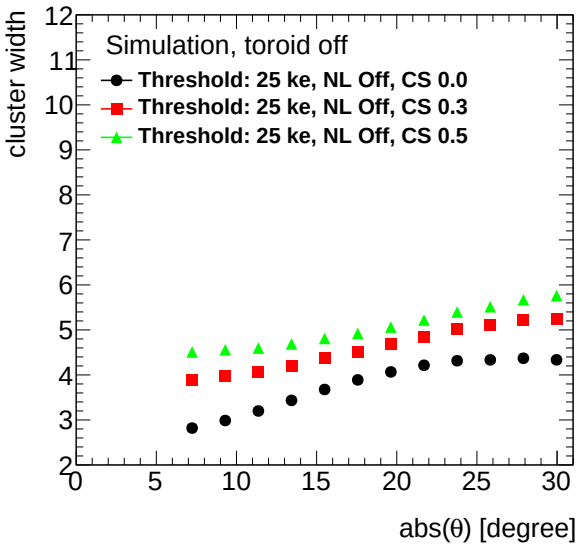

(c) Threshold 25 000 electrons, NL off

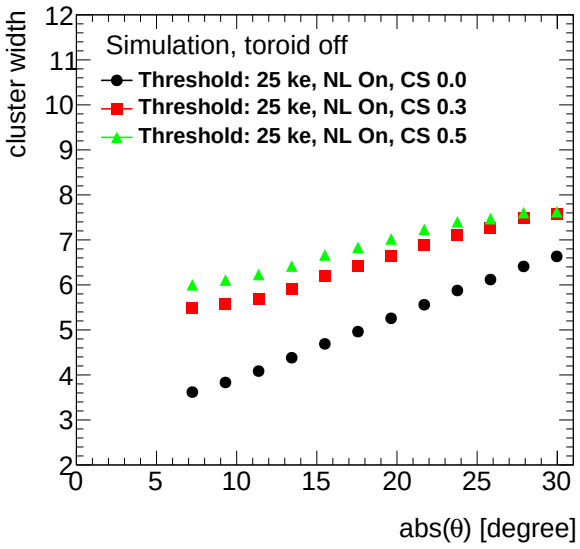

(d) Threshold 25 000 electrons, NL on

Figure 10.8.: Cluster width as a function of the muon incident angle θ for different configurations of the digitization. The value for the CS between the main strip and its direct neighbors is indicated in the legend of each plot. The CS ratio to the next-to-next neighbor strip is the square of this value. Note: the centroid clusterization method allows for one missing strip in between two strips above the threshold.

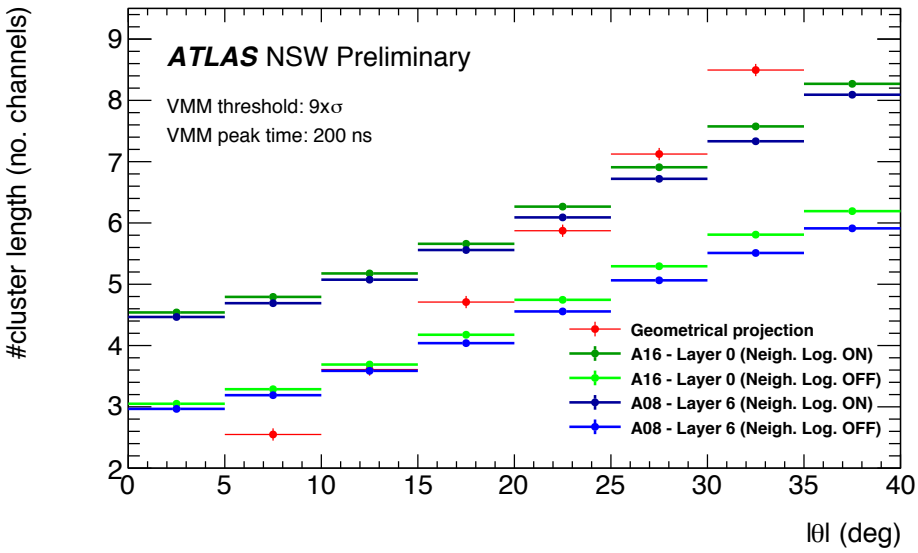

Figure 10.9.: Cluster width as a function of the muon incident angle θ taken from cosmic data. Note: the centroid clusterization method allows for one missing strip in between two strips above the threshold. Modified from [2].

sees at the beginning and the end of the drift time spectrum. The tails towards high drift times in the spectra of the central strips stem from the fact that also clusters with less than 7 strips are included in the plot. The width of the core distributions of these strips is influenced by diffusion effects and ionization statistics.

Figure 10.11 shows the drift time distributions for different settings of the NL, the threshold, and the CS for muons whose track is inclined by more than 20°. For the cosmic data, the measurement of the drift time is ongoing but not yet finished, so no comparison between data and simulation is shown. For the simulation alone, the width of the time distributions perfectly matches the value of about 100 ns that one expects by design. Furthermore it is independent of the configuration, while the shape of the time distribution strongly depends on it. The configuration without CS (black markers) follows the shape discussed above quite well for all values of the other parameters, where the NL (right column) enhances the peaks at the beginning and end of the spectrum. Adding CS pulls the time measurements more towards the mean time. This can be explained as follows. By sharing the charge among the strips, the overall time measurement of a strip is influenced by all 4 neighboring strips. Since the central strips of a cluster tend to have more charge than the outer ones (see figure 10.10c), the time measurement of the outer strips gets biased towards the time of the inner strips. This effect is less pronounced for the case where the NL is switched off since the strips next to the outer strips, which are only active due to CS and more often read out with the NL being enabled, have a similar arrival time as the actual unbiased outer strip would

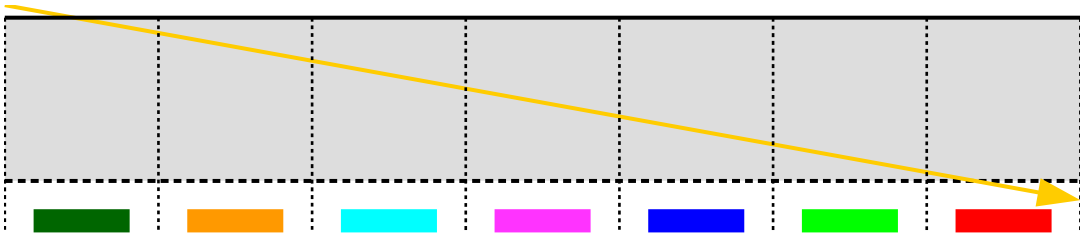

(a) Ionizing particle crossing the drift gap

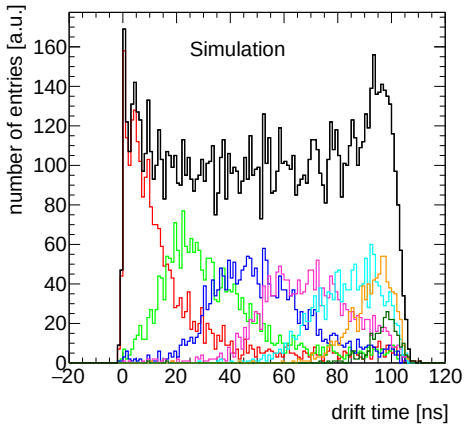

(b) Drift time distribution

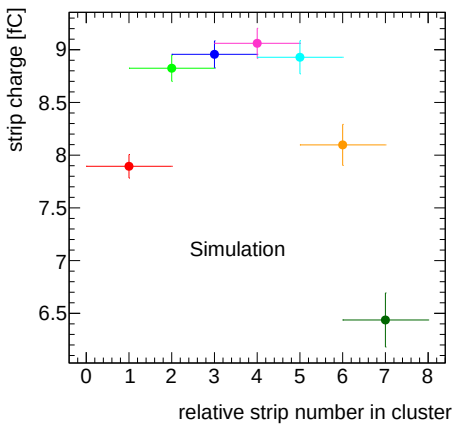

(c) Mean strip charge

Figure 10.10.: Illustration of the drift time distributions at each strip of a cluster that stem from the ionizations induced by a particle traversing through the detector at an angle. **(a):** The ionizing particle (orange arrow) crossing the drift gap of a Micromegas (light grey area) uniformly generates ionizations along its path. While these ionizations happen symmetrically over the central strips, this is not the case for the outer two strips. While the rightmost strip (red) only receives charge from ionizations very close to the mesh and therefore with a very small drift time, the leftmost strip (dark green) only receives charge from ionizations very close to the drift cathode leading to the maximum drift time of around 100 ns. **(b):** Total drift time distribution (black) for tracks crossing the detector under an angle of more than 25° and the drift times for each individual strip in the cluster color-coded according to figure (a). As expected the first and the last strip have asymmetric time distributions since the ionizations do not happen centrally on the strips. This leads to the peaks at the beginning and the end of the total drift time distribution. For the strips in the center of the cluster, the time distributions are more symmetric since on average the ionizations occur over the center of the strip. The tails towards long drift times can be explained by the clusters with less than 7 strips, e.g., due to the high charge threshold. **(c):** Mean charge collected on a strip as a function of the relative strip number inside a cluster for particles crossing the detector under an angle of more than 25°. It can be seen that the central strips of a cluster receive more charge compared to the outer ones. This explains why a stronger CS makes the drift time distributions more narrow, i.e. the times are skewed towards the ones of the strips with more charge.

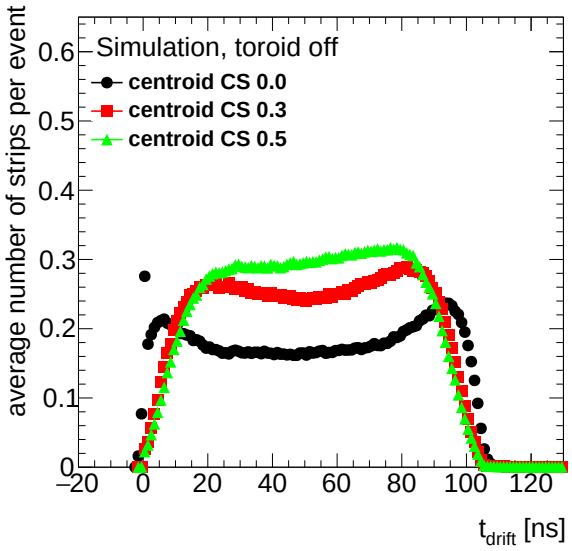

(a) Threshold 15 000 electrons, NL off

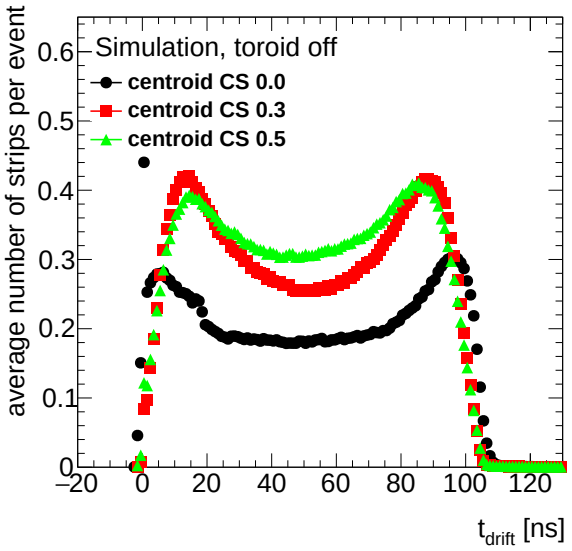

(b) Threshold 15 000 electrons, NL on

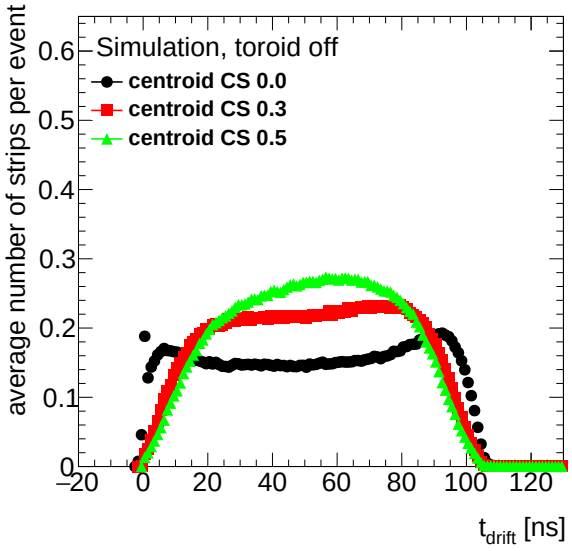

(c) Threshold 25 000 electrons, NL off

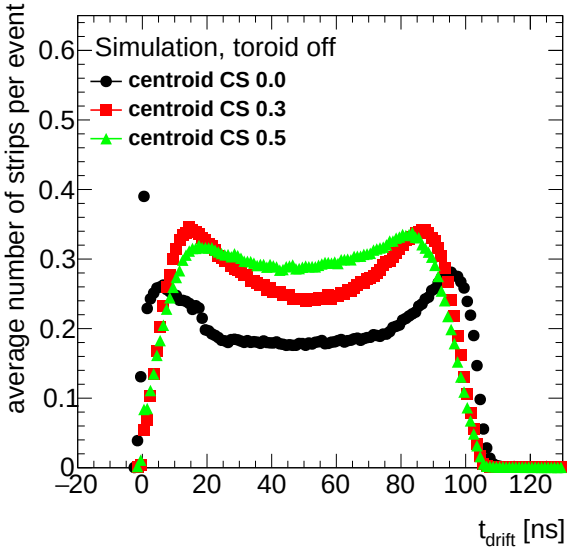

(d) Threshold 25 000 electrons, NL on

Figure 10.11.: Drift time distribution for different settings of the charge threshold, the NL, and the CS in the digitization. Only muons whose track is inclined by more than 20° are selected for these plots. The drift time refers to the time of arrival of the charge measured for each strip by the VMM. The histograms are normalized to the total number of generated events. Consequentially, the vertical axis gives the average number of strips per time value and the integrals of the distributions correspond to the total number of active strips in each case. Each of the two muons of the event passes through eight layers of Micromegas, all of which are included in this figure.

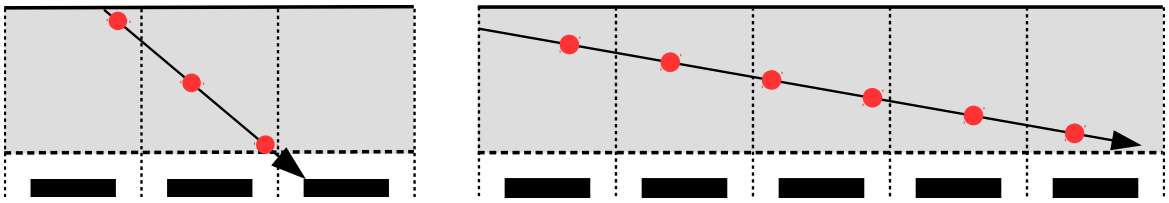

(a) Small angle (b) Large angle

Figure 10.12.: Illustration of the impact of the incident angle on the time distribution of the first hit. For a small angle (a) between a track and the detector, the electrons from multiple ionizations will be collected by the same strip (pile-up). The time measurement of that strip will be biased towards the time of the charge deposit with the highest charge, which is not necessarily the earliest one. For larger angles (b), single ionizations become resolvable on a strip leading to a better time resolution.

have. Increasing the threshold (bottom row) for the case without CS shows no significant impact on the distributions. In the case with CS on, the higher threshold cuts away the outer strips of a cluster, leading to a reduction of the difference in height between the peaks and the plateau in the central part of the distributions.

10.3.7. Dependence of the Time Resolution on Digitization Parameters

Another important parameter to be studied is the time resolution of the detector and its modeling in the simulation, since it has a direct impact on the reconstruction performance using the μTPC or the CTP methods. One way to extract the time resolution of the Micromegas detectors is to consider the time of arrival of the first hit in a layer and then take the width of the distribution as the time resolution. Since the trigger of the Micromegas is based on the VMM's ability to send out the address of the first hit in real time, this way of measuring the time resolution is relevant for the trigger as well. As discussed in the section above and depicted in figure 10.10, the time spectrum of the first hit is not Gaussian since there is a steep rise at 0 ns and tails towards higher times. Therefore both the resolution and the mean value are extracted from the histograms containing the time of arrival of the first hit for specific incident angles and not by a fit of the histograms.

Figure 10.13 shows the mean value of the time of arrival of the first hit for different configurations of the VMM and the CS. In general, the time of arrival depends heavily on the incident angle, the reason being illustrated in figure 10.12. For a small incident angle the charge from multiple primary ionizations ends up on the same strip but at different times. This effect is referred to as *pile-up*. As discussed in section 10.2.1, in case of pile-up, the time measurement is biased towards the highest charge deposit which does not necessarily come from the first ionization. Therefore the mean time of the first strip is pulled towards higher values. The larger the angle becomes the less pile-up of primary ionizations appears on the individual strips. At larger angles, the first ionization starts to be resolvable and therefore the time of the first strip decreases. As already

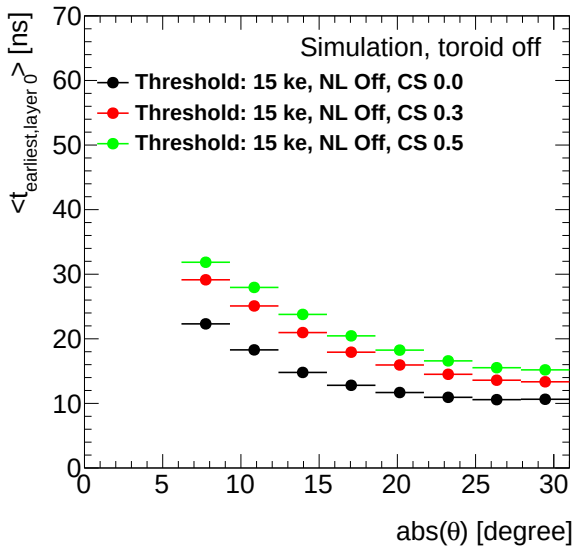

(a) Threshold 15 000 electrons, NL off

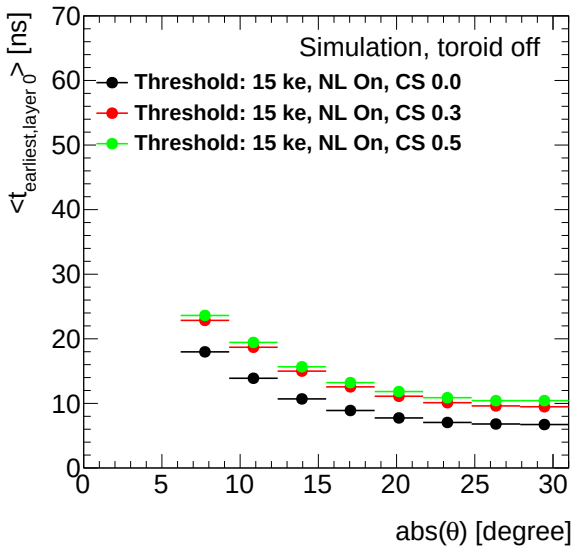

(b) Threshold 15 000 electrons, NL on

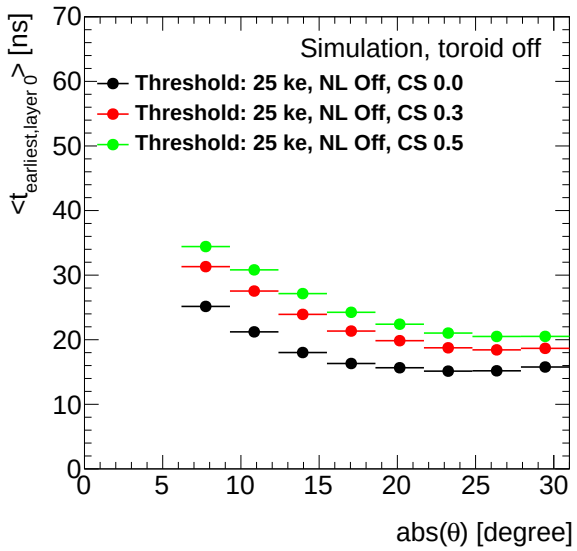

(c) Threshold 25 000 electrons, NL off

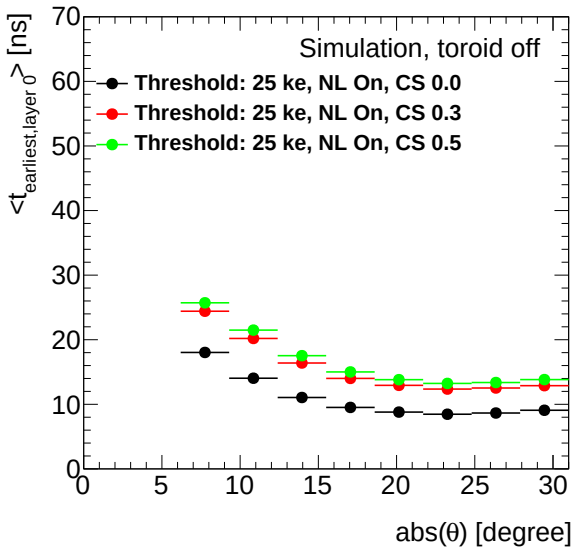

(d) Threshold 25 000 electrons, NL on

Figure 10.13.: Mean value of the earliest hit time as a function of the muon incident angle θ for different configurations of the digitization. The value for CS between the main strips and its direct neighbors is indicated in the legend of each plot. The CS ratio to the next-to-next neighbor strip is the square of this value.

discussed for the drift time distributions, CS leads to the first hit appearing significantly later since additional pile-up is introduced by charge induction from the adjacent strips. For the NL disabled (left column), the highest CS values (green markers) also lead to the latest arrival of the

first hit; this is not the case for the scenario with the NL enabled (right column). Here the values are almost the same with CS of 0.5 yielding slightly smaller times of earliest arrivals compared to the case of a value of CS of 0.3. This can be explained by the fact that with the higher charge value a few more strips are above threshold induced by CS and therefore their neighbors are read out as well which are less influenced by the central strips. The different thresholds mainly impact the distributions at higher incident angles. Here the charge is distributed over more strips and therefore the charge of the individual strips is lower leading to a higher chance to be cut by a larger threshold. This leads to the time of the earliest hit increasing with a higher threshold (bottom row) since the chance to miss the first hit increases. The same effect can also be observed for the NL being on. When the NL is on, the time of arrival is almost 10 ns smaller than for the NL being off since the first hit is recovered.

Figure 10.14 shows the time resolution for different settings. In general, one can observe that the time resolution improves up to incident angles of $15-20°$. For larger angles it either remains constant or gets worse, depending on the parameter settings. This can be explained by the effect described above. For lower angles, the pile-up on the strips from the different primary ionizations is large and the first strip starts to be more resolvable the higher the incident angle is. For large angles, the first strips start to be cut off by the charge threshold, which then again increases the time resolution. Therefore the rise at large angles is also more pronounced for high thresholds. While CS has nearly no impact on the time resolution with the NL disabled (left column), the time resolution gets worse the more CS is applied with the NL on, especially for the higher threshold (bottom right figure). In general, enabling the NL improves the time resolution. This can be explained as follows. Looking at the earliest hit, which is the outermost strip of the cluster, two neighboring strips obtain some charge from CS. The timing of the induced charge deposits is the same as for the original charge. Therefore the charge and time of the second outer neighbor are only correlated to the initial earliest hit, while the time measurement of the first strip from CS is distorted by the second outermost strip of the original cluster. Since only the first strip, which fired due to CS, is likely above the threshold, the case of NL off does not lead to an undistorted time measurement. With the NL on, the second CS induced strip is read out, which has the pure time and charge information. This is also the reason why the value of the time resolution improves in general for the NL enabled, especially for the case of the higher threshold.

For the cosmic data, the measurement of the time resolution is still ongoing. First results indicate a time resolution of around 25 ns. The values obtained in the simulation are better than that. Therefore the option of applying a Gaussian smearing on the time resolution was introduced to the simulation. The default value of the smearing width is set to 20 ns. The intrinsic time resolution as yielded by the digitization is 15 ns averaged over all settings. Adding the squares of the intrinsic resolution and the smearing, and taking the square root leads to a resolution of 25 ns, compatible to what was measured for the detector.

In general it is desirable that the simulation is a bit more optimistic than the data since this can be corrected by a smearing of the digitization as done here. Nevertheless, in the future, the reason for the simulation being too optimistic will be studied to optimise the modeling of the detector.

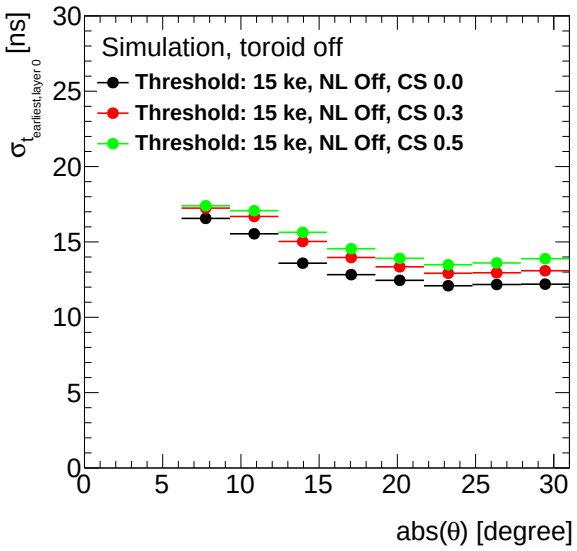

(a) Threshold 15 000 electrons, NL off

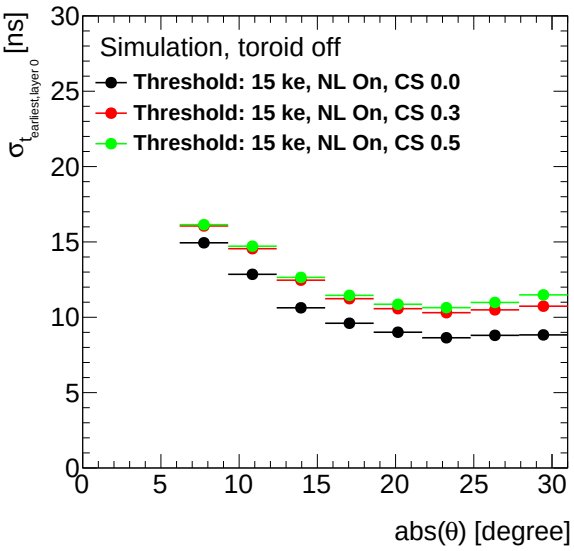

(b) Threshold 15 000 electrons, NL on

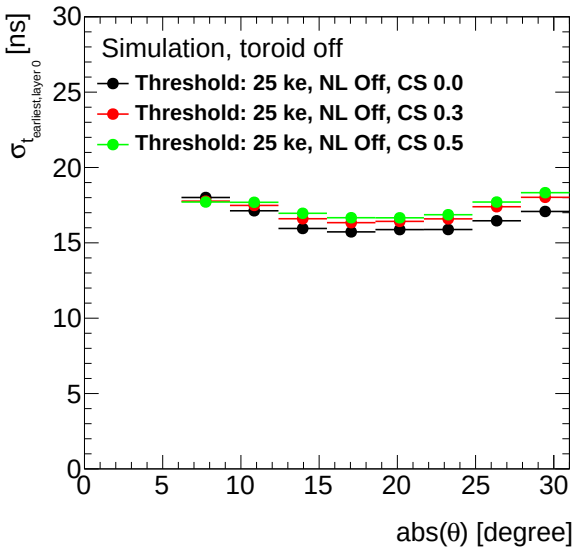

(c) Threshold 25 000 electrons, NL off

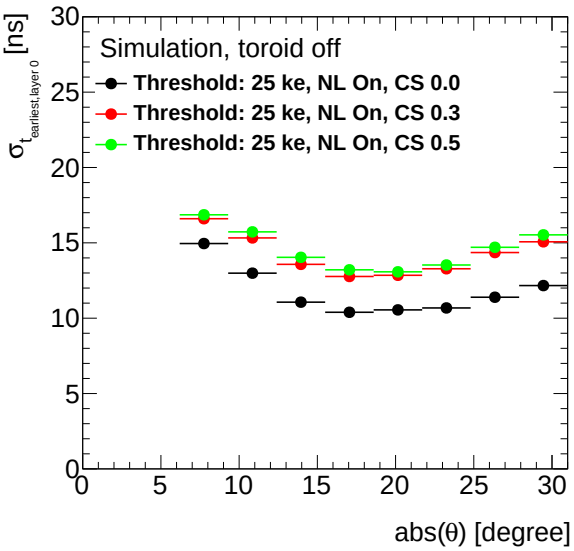

(d) Threshold 25 000 electrons, NL on

Figure 10.14.: Time resolution as a function of the muon incident angle θ for different configurations of the digitization. The value for CS between the main strip and its direct neighbors is indicated in the legend of each plot. The CS ratio to the next-to-next neighbor strip is the square of this value.

For example, the modeling of CS only includes the same-sign CS between the resistive and the copper strips, while there is also the opposite-sign scenario between the copper strips themselves, which can have an impact on the VMM time measurement.

10.3.8. Modeling the High Voltage Map with the Digitization

Some high voltage sections of the Micromegas detectors can only be operated at lowered HV applied to the strips to avoid sparking in the amplification gap caused by, e.g., a low resistivity of the resistive strips and mechanical non-uniformities of the thin amplification gap. To study the impact of these sections with reduced high voltage and subsequently lower gain and reconstruction efficiency on the overall performance of the NSW, a simulation of this effect has been added to the digitization. It is based on a parametrization of the cluster charge as a function of the applied voltage on the resistive strips. Figure 10.15 shows an exemplary distribution from the cosmic test stand. The cluster charge which corresponds to the gain was modeled as follows:

$$G = e^{a+bx}, \tag{10.6}$$

with

$$a = -8.87971 \quad \text{and} \quad b = 0.0224561\,/\,\mathrm{V},$$

and x being the actual value of the strip voltage. The parametrization and the parameter values were provided by [90]. In the digitization, the nominal gain of 8000 corresponds to the nominal strip voltage of 570 V. A different voltage is simulated by calculating the fraction of the cluster charge compared to the value at 570 V and then scaling the gas gain by this ratio. In the digitization, a map of the high voltage with the granularity of one PCB corresponding to 1024 strips is applied. For the verification of the impact of this gain scaling, multiple datasets with

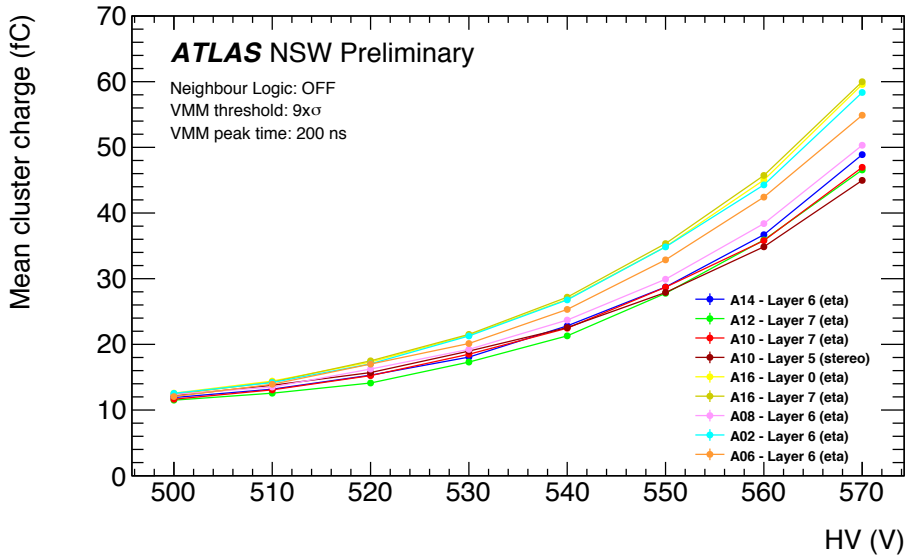

Figure 10.15.: Cluster charge as a function of the voltage applied on the resistive strips measured in cosmic data. Modified from [2].

different gain values were produced and the reconstruction was performed using the centroid clusterization.
Figure 10.16 shows the efficiency of reconstructing a cluster as a function of the voltage applied to the resistive strips. The definition of the efficiency for the simulated data is described later in section 11.3. It is given by the presence of a cluster in a gas gap since only single-muon tracks are simulated. The red line corresponds to the efficiency measured in the cosmic data. Since noisy hits are present in the data, a layer is considered efficient not just based on the presence of a cluster but only if the cluster can be assigned to a track determined by the other layers. From figure 10.16 one can conclude that the efficiency of the data and the simulation match well, especially for medium angles. For small and large angles there are discrepancies, which can be explained by the fact that the measurement in the data is the average over all angles. But in general, this plot shows nicely that, after tuning all the parameters, the simulation is able to reproduce the data.

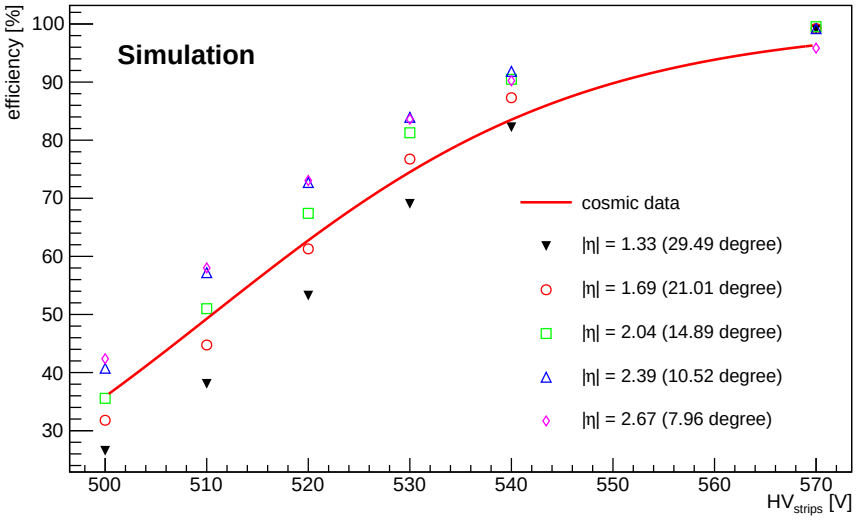

Figure 10.16.: Reconstruction efficiency as a function of the voltage applied to the strips.

10.3.9. Verification of Charge Sharing

The implementation of CS in the simulation can be verified by the same method used to measure it in data (see section 8.3.3). This method compares the charge deposited on the first or last strip of a cluster to that of its direct neighbor. Figure 10.17 displays the ratio of the charges deposited on the first and the second outermost strips of a cluster. The cluster was reconstructed using the centroid method. The figure nicely shows that for CS ratios of 0.3 and 0.5 the distributions peak at the corresponding values. Therefore the implementation of CS is considered verified.

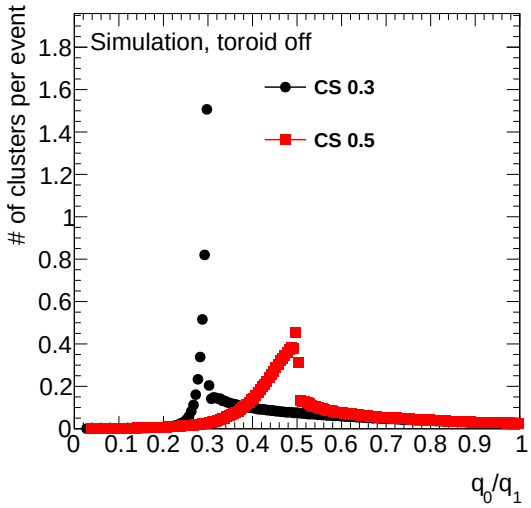

Figure 10.17.: Verification of the CS implementation. The plot shows the ratio of the charges deposited on the first and second outermost strip of a cluster formed with the centroid method. The peaks at the values corresponding to the individual CS values indicate that the simulation of the CS is working as expected.

10.4. Summary of the Work on the Digitization

In the scope of this thesis, major improvements have been made to the Micromegas digitization algorithms. Amongst them is the implementation of the actual response of the VMM shaping amplifier, a strip length-dependent threshold, and the modeling of CS. Furthermore, the technical performance of the digitization code has been significantly improved, which was critical to meet the computing requirements of ATLAS. With the new features, the output of the digitization has been compared to the quantities obtained from the cosmic data test stand used in the integration of the modules, equipped with the final electronics and the final detector modules. Based on these comparisons, the different parameters of the digitization were optimized to match the results of the cosmic test stand. Amongst the tuned parameters are the gas gain and the CS. Also, the impact of the different settings of the electronics was investigated. With the set of optimal parameters, the digitization matches the cosmic data nicely in almost all relevant parameters, with a tendency to be a bit too optimistic for some of them. One example for that is the time resolution, where the digitization shows values well below 20 ns while the ongoing analysis of the cosmics data suggests values of around 25 ns. Therefore, a smearing of the time measurement is applied to the digitization. The set of default parameters determined in this thesis will be used in the first Monte-Carlo sample production for the upcoming ATLAS data taking period.

11. Reconstruction with the Micromegas Detectors

As already discussed in section 4.2.7, the reconstruction of muon tracks in the Muon Spectrometer consists of multiple steps. First the raw data coming from either simulation or from the real detector needs to be calibrated. Then a clusterization of detector channels with signals exceeding the threshold is performed on each layer if the detector layout allows for it, which is the case for all detectors with strip-segmented electrodes. Afterwards, track segments are built and finally these are combined into the complete track through the full detector. For the Micromegas, methods for the calibration of the raw data and single-layer drift time based reconstruction algorithms have been developed and implemented into athena within the scope of this thesis. They are discussed in the following sections. First the calibration and the technical implementation of the clusterizations will be described. Then the performance of the reconstruction will be discussed for different digitization parameters. Finally the calibration of the cluster position against the magnetic field will be introduced.

11.1. Calibration of the Raw Data

The first step of the reconstruction for the Micromegas is the calibration of the raw data coming either from the detector or the simulation. For the raw data coming from the detector, a calibration of the ADC counts needs to be applied to convert the charge and time information to physical units like fC and ns, respectively. This calibration must be done per channel and is the same one as described in section 7.3.2. In a second step which is necessary for both data and simulated events, the time of flight of the muon and the peaking time of the VMM are subtracted from the measured time. The time of flight is determined by the distance between the strip under calibration and the center of ATLAS where the particle collisions happen, and it is assumed that the muon is traveling at the speed of light. The time of flight is in the order of $24-27\,\text{ns}$, depending on the radial position in the NSW and the z position of the layer. The peaking time of the VMM needs to be subtracted from the time measurement, since not the time at the peak but the time of arrival of the earliest charge at each strip is the relevant quantity. For raw data coming from the detector a third step in the calibration is done, taking into account the various signal delays for different regions in the detector due to, e.g., different cable lengths. In the final step of the calibration the errors in longitudinal and transverse drift directions discussed in equations 6.5 and 6.6 are computed.

11.2. Technical Implementation of the Clusterization Algorithms

In section 6.3 different methods to reconstruct clusters and their positions in Micromegas detectors are presented and their input parameters are summarized in table 6.1. These algorithms are briefly reviewed in the following.

The centroid reconstruction method (see section 6.3.1) is the simplest of those discussed. It groups adjacent strips with a signal above threshold into clusters and reconstructs the cluster position as the mean value of the strip positions in the cluster, weighted by their respective charges. The centroid method works well for particles penetrating the detector perpendicularly, but loses the precision in the reconstructed position for inclined tracks, as will be shown later in this chapter and is also visible in figure 8.11 for the test beam. A way to maintain good resolution also for inclined tracks is to rely on the μTPC method. Here the grouping of the strips is done using the HT, a standard algorithm in computer vision applications. The cluster position is obtained from a linear fit of the strip positions and the time of arrival of every strip, which corresponds to the drift distance of each primary electron in the drift gap. The μTPC method (see section 6.3.3) works very well in an environment with little noise, but cannot cope with high strip charge thresholds that are the result of higher noise levels, as was shown in section 8.3.4. While the precision of the reconstructed position is still almost in the required range, the major impact of the high thresholds is on the reconstruction efficiency. In order to get a good resolution together with a good reconstruction efficiency for inclined tracks, as they are present in the NSW, the additional information of an external estimate of the angle of the particle track with respect to the Micromegas is employed. In ATLAS this estimate can be determined in two ways, where the simpler one calculates the angle from the assumption that the track comes from the center of the ATLAS detector and therefore the angle can be obtained from the strip positions. The second way is to fit a track segment with the 16 layers of the NSW detectors and take its slope as the estimate for the angle. The external angle is then used in two different clusterization methods, the Cluster Time Projection (see section 6.3.2) and the constrained μTPC method (see section 6.3.4). The CTP method relies on the angle together with the drift time measurements to project the position of the centroid clusters to the center of the gas gap. The constrained μTPC method is similar to the unconstrained one, but the external angle estimate is used as a constraint on the final fit and in the clusterization step. For all results presented in the following, the first method to obtain the estimate of the external angle was deployed, i.e., relying on the strip position relative to the interaction point, since only muons coming from the interaction point are studied. However the method is not applicable anymore for cosmic data taking or proton-proton collision where, e.g., long-lived particles could be produced which decay at a secondary vertex that is displaced with respect to the IP. For this reason the second method to estimate the angle will be used in the future and the necessary developments in the software infrastructure are ongoing.

The sections referenced above describe the general idea and methodology of the individual cluster reconstruction methods. However, especially for the use in the context of the full geometry of the ATLAS detector, several optimizations have been applied in order to, e.g., save CPU time

or to cope with the high rate of background particles that is expected. In the following, a short recap of the technical implementation of each method is provided together with the modifications applied for the usage of the algorithms in ATLAS.

11.2.1. Centroid and Cluster Time Projection Methods

The centroid and the CTP methods were introduced in sections 6.3.1 and 6.3.2, respectively. In both methods the clusterization is done by combining adjacent strips. In their athena implementations they allow for a maximum of one strip with a signal below threshold between two active strips. For the centroid method the cluster position is determined as the charge-weighted mean position of the strips assigned to the cluster. The CTP method refines the position obtained with the centroid method by using the drift time information to project it to the center of the gas gap. In the current implementation, the angle is determined from the charge-weighted mean azimuthal angle of the individual strips with respect to the center of ATLAS. As discussed in the introduction of this chapter, this will be changed later in order to use the angle of the track segment reconstructed with the NSW detectors. The estimated angle together with the charge-weighted mean drift distance is then used to correct the centroid position according to equation 6.7 with the uncertainty given in equation 6.8. One aspect to be considered while applying the correction is that the drift direction of the electrons in the drift gap is antiparallel to the direction of flight of the muon for every second gas gap. Therefore the correction needs to be subtracted from the centroid position for all even gas gaps, while it needs to be added for all odd gas gaps.

11.2.2. μTPC Method

As discussed already in section 6.3.3, the clusterization part of the μTPC algorithm is based on the HT. Its purpose is to filter the strip position and drift time measurements for strips whose position and time coordinates form a line in the drift gap. This transformation is applied in the coordinate system spanned by a vector orthogonal to the strips and a vector antiparallel to the drift direction in each Micromegas drift gap. In a second step the selected points are fitted and the cluster position is reconstructed at half of the height of the gas gap. For the usage in the ATLAS geometry this general procedure was refined in the following way in order to reduce the amount of memory and CPU time spent within athena.
First a coarse reconstruction of clusters is performed according to the centroid method but with up to three adjacent strips allowed to have a signal below threshold. This is relevant to account for two effects: noisy hits and the gas ionization by background radiation, like neutrons. In the second step, the pattern recognition is performed on each of these coarse clusters, but rather than using the actual position of the strips, the positions of the strips assigned to the coarse cluster are centered around their mean value. This allows to keep the range and therefore the number of bins for the distance parameter in the HT small. The parameter is given by the squared sum of the maximum drift distance and the maximum of the strip position. With primary coarse clustering, the latter gets reduced from several meters to a few mm depending on how many strips are in

the cluster. The maximum drift distance was chosen to be 6 mm according to the Micromegas geometry, including 1 mm of margin to account for, e.g., time offsets. The second advantage of centering the strip positions around their mean value is to reduce the extrapolation error due to the binning of the angle in the HT which therefore simplifies the strip selection. The strip selection itself is done taking the residuals in drift distance compared to the line predicted by the HT. Then, hits with a residual within a given window around the median of all residuals are selected, where the median is applied to suppress shifts of the predicted line due to binning effects from the HT. The window is configurable and its default value was set to 1 mm.

A reduction of the parameter range is also applied to the angle used in the HT. Since the Micromegas layers are built in a back-to-back way, the drift of electrons in the drift gap follows the direction of flight of the muon for odd gas gaps and is opposite for even gas gaps. This translates to the reconstruction of negative incident angles for even gas gaps and would require the HT to take into account the full spectrum from $-90°$ to $90°$. The parameter range is reduced by flipping the sign of the difference between the strip position and its mean value for all even gas gaps, allowing to perform the HT in an angular range of $0°$ to $90°$. If the HT was not successful in finding strip signals on a line, all strip signals are forwarded to the final fit to keep the signal information of that layer for further steps of the track reconstruction. This will be dropped once the idea for an improved cluster reconstruction combining the different methods, which is discussed at the end of this section, is implemented. The centering of the strip positions around their mean value is also applied in the final fit of the μTPC line, which is the last step in the reconstruction procedure. This is done to remove the extrapolation error from the uncertainties obtained for the fit parameters which are subsequently used to determine the final resolution of the reconstructed position. Otherwise the uncertainty of the position would grow with the distance to the center of the chamber which is the origin of the local coordinate system (see section 5.4). After the fit and the calculation of the μTPC position, which is done by evaluating the fit at half the height of the drift gap, the mean value is added to the obtained cluster position to get the position in the chamber coordinates.

The final fit itself is done in a two-step procedure. First the points yielded by the HT are fitted using the package *TLinearFitter* [91] provided by *ROOT*, which performs the linear fit analytically, only employing the uncertainties in the drift direction. The fit parameters are then used as the seed for a χ^2 minimization relying on the uncertainties in both directions. The second fit is done via *MINUIT* [92], and it restricts the slope parameter to a range between $5°$ and $81°$. This prevents the fit from going to unfeasible angles while still keeping a wide acceptance window. The angles expected in the NSW are $7-31°$, so well within the limits given to the fit. Finally a cluster is only accepted if the fit succeeded and if none of the slope values are equal to the limits applied in the fit. As discussed for the CTP, the limits on the angles need to take the orientation of the gas gap into account, since the drift direction is inverted for every other gap. Therefore negative angles are applied as limits to the even gas gaps and positive ones to the odd gas gaps.

11.2.3. Constrained μTPC

As described in section 6.3.4, a reconstruction algorithm similar to the μTPC method but with a constraint on the angle has been developed in the scope of this thesis. Compared to the CTP method, not only the angle of the incoming muons θ is used, but also the information on its uncertainty. This constraint enters into both the pattern recognition and the final fit. As discussed in the previous section, the pattern recognition consists of two major steps. First, neighboring strips are grouped to coarse clusters, allowing up to three missing strips between two strips that fired. The position of the strips forming a cluster is then used to estimate θ in a similar way as described for the CTP method. Based on this estimate the next step in the pattern recognition is to filter the strips associated to the coarse cluster based on the additional information on their drift time. This procedure is described in detail in section 6.3.4 and depicted in figure 6.6. Here a short overview over the procedure is given and the details of the athena implementation are discussed.
For the filtering of the strips based on the drift time and the strip position, two lines with slopes corresponding to the estimated ($\theta \pm \sigma_\theta$) form an acceptance corridor. Then the intercept of the lines is varied by a configurable width around the ideal value of 2.5 mm, which is the same for all clusters. This assumption can be made since the strip positions are centered around their charge-weighted mean value, which also leads to the cluster being centered time wise. The sign flipping of the strip position is implemented similarly to the μTPC method, in order to remove the different signs of the angle per gas gap. For each intercept in the scan, those strips and times that are within the acceptance corridor given by the two aforementioned lines are counted and the intercept with most of the strips is selected. Strips outside the corridor by less than three times the error on the drift distance, given by equation 6.6, are counted as well. The scan is performed in an intercept window of ± 2 mm around the ideal value in steps of 0.1 mm. The strips belonging to the best intercept value are then fitted by minimizing the likelihood function given in equation 6.10, relying on the *MINUIT* algorithm interfaced with *ROOT*. The fit is performed using the centered strip positions. The position of the cluster is determined by evaluating the fit at half the height of the gas gap. Then the mean strip position is added to that value.

11.2.4. Outlook: Preclustering and Combination of the Different Methods

As already described for the test beam and as is discussed in section 11.3 for the simulation, different clusterization methods are better suited for different incident angles in terms of either resolution or efficiency. Therefore it will be necessary to combine the different clusterization methods to assure the best performance of the event reconstruction. A first skeleton for this combination has been implemented in the scope of this thesis and is sketched in the following. For technical reasons the combination is not yet used inside athena.
First the strips with a signal above threshold are sorted by layer. Then clusters are created, based on the centroid clusterization but allowing a larger number of strips with a signal below threshold between two active strips. The default value for the number of missing strips is three for now,

but will be optimized in the future. After the coarse clustering a more precise clusterization is applied on each coarse cluster in a staged system, aiming for a refined strip selection and position reconstruction. First the reconstruction is run with the μTPC method. If it builds at least one refined cluster out of a coarse one, the refined clusters are accepted and the algorithm moves on to the next coarse cluster. If the μTPC method fails, the coarse cluster will be processed with the centroid method. This second reconstruction method has a worse resolution for high muon incident angles but an excellent reconstruction efficiency which helps to recover the signals from layers which would be lost due to reconstruction inefficiencies of the μTPC method. With this possibility for the recovery of clusters, the procedures of efficiency recovery added to the standalone μTPC method, which worsen the resolution, can be removed. One of them is that in case the HT did not find enough strips, all available strips are fitted. Furthermore the minimum number of strips in the fit can be increased from 2 to at least 3 or even higher values.
In the future, further criteria can be added to the decision which reconstruction method is used, e.g. the number of active strips assigned to the coarse cluster or its radial position which correlates to the incident angle. The primary and secondary reconstruction methods are fully configurable such that any, potentially new clusterization method can serve as primary or secondary algorithm. Also the possibility to force the usage of a single method is foreseen, which can be useful for, e.g., performance studies.

11.3. Performance of the Single-Layer Position Reconstruction

In this section the performance of the single-layer reconstruction methods are discussed for different configurations of the digitization, namely the settings of the CS, the NL of the VMM, the charge threshold, and the time smearing. The samples used to study the performance were produced with the setup discussed in section 10.3.2. They consist of pure di-muon events with a transverse momentum in the range of $10-100\,\mathrm{GeV}$. The simulation was performed with the toroid magnetic field switched off, which allows to study the performance without any impact of the non-uniform toroid field on the reconstructed cluster position. Results with the toroid field on and the cluster position being corrected are shown later in section 11.4.
In the following, the procedures to determine the resolution and the efficiency are introduced first. Then the performance of the different reconstruction algorithms is presented based on the nominal digitization settings, followed by a discussion of how the performance depends on the various parameter settings. First the impact of the detector and electronics settings, e.g. the charge threshold, the NL and CS, are discussed. Then the effect of the time smearing (see section 10.3.7) is presented, which is necessary since the time resolution obtained with the digitization is too optimistic compared to what has been measured on the detectors. The former study is only carried out with the μTPC and the centroid methods, since those can run directly on the raw signals obtained from the detector or simulated events, and do not impose the need for an iterative reconstruction procedure. In constrast, the CTP and constrained μTPC methods rely on a fit of the previously extracted cluster position in the different layers in order to obtain the estimate of

the incident angle. Since the centroid and the μTPC procedures perform well in the case without the time smearing, the CTP and the constrained μTPC methods were only taken into account for the study with time smearing applied.
In order to guide the reader through the presentation of the results below, table 11.1 summarizes the expected behavior of the different cluster reconstruction methods.

Reco. method	Expected behavior
centroid	• high precision @ low incident angles • very poor precision @ high incident angles • very high reconstruction efficiency over all angles • res. and eff. insensitive to variations of CS • res. and eff. insensitive to time smearing • resolution sensitive to threshold variations • efficiency not sensitive to threshold variations
μTPC	• good resolution at high incident angle • large negative impact of CS on resolution • large negative impact of time smearing on resolution • efficiency and resolution highly dependent on threshold
constrained μTPC	• more stable against time smearing than μTPC • otherwise similar behavior as μTPC • requires external estimate of angle
CTP	• excellent resolution at small angles • good resolution at large angles • excellent efficiency over full angular range • able to cope with time smearing and CS • requires additional information of the incident angle

Table 11.1.: Expected behavior of the different cluster reconstruction methods. The expectations are derived from their behavior in the test beam, and from the information exploited in the reconstruction method which are summarized in table 6.1.

11.3.1. Definition of Resolution and Efficiency

Given that the samples employed for the performance studies below were produced with the toroid field off, the standard reconstruction methods to fit the muon track cannot be used. The resolution is therefore extracted by comparing the reconstructed cluster position with the truth position of the energy deposit generated by the GEANT4 simulation. The distance between these two positions is calculated along the precision coordinate, which is perpendicular to the strips and corresponds to the radial direction in the wheel. Due to the very clean samples, containing a single muon per detector side, a simple matching of the clusters to the truth hit can be performed, only requiring the two objects to be in the same gas gap. In case there are multiple clusters or truth hits in one gap, e.g. through radiated particles or clusters that are split in two by too

many consecutive strips being below threshold, the combination of cluster and truth hit with the smallest residual is chosen. The residuals are then filled into a histogram and the resolution is determined following the same recipe as for the test beam, discussed in section 8.1.2. According to the observed shape of the residual distributions, a fit is performed using the sum of two Gaussian functions, one accounting for the core of the distribution and one for the tails. The seed for this fit is obtained from a fit with a single Gaussian distribution carried out beforehand. The figures of merit from the fit with the double Gaussian distribution are the mean value and the width of the core Gaussian σ_{core}, and the weighted width of the two Gaussians σ_{weighted}. The weighing is done using the integral of the individual distributions in a range of $\pm\,\sigma_{\text{core}}$ (fit range), which is slightly different to what was done for the test beam[1]. The resolution plots shown below only contain the residuals of the even η layers. This has multiple reasons among which the two most relevant are mentioned. First, only the η layers are included since the stereo layers are expected to have a worse resolution in the precision coordinate given their rotated strip geometry. Second, even and odd layers need to be separated since the drift direction is opposite. So any effect with an impact on the position of the cluster in the time coordinate, which would impact the mean residual, would cancel out if the residuals would be collected over all gaps.
For the calculation of the efficiency the pureness of the samples is exploited. Given that there is only one muon per detector side, the efficiency is determined as follows. First it is checked if the generated muon on a detector side is within the NSW acceptance of $1.3 \leq |\eta| \leq 2.7$. Then each of the eight Micromegas layers of a side is searched for a reconstructed cluster. If a cluster is found, the layer is declared efficient, otherwise not. It was also tested if a matching of the reconstructed cluster to the energy deposition from GEANT4 changed the results. Since the effect was below 1 % and only present at very low angles, the truth matching was not used in the following plots. In the future, the efficiency calculation will be carried out using the reconstructed track information, but this was not possible for the samples without the toroid field. For the plots of resolutions and efficiencies as functions of the track incident angle, the information of the angle is obtained as the truth angle under which the muon was generated.

11.3.2. Performance of the Centroid and the μTPC Methods for the Default Digitization Settings

In this section the reconstruction performance is discussed for the samples produced with the nominal settings of the digitization, summarized in table 10.1. Figure 11.1 shows the weighted resolution for this configuration for the μTPC (red points) and the centroid (black points) methods. As expected the centroid method reaches resolutions in the order of 100 μm for low incident angles, but the resolution grows for larger incident angles to 500 μm at 30°. This is compatible with the results obtained in the test beam. The resolution obtained with the μTPC algorithm behaves the other way around. For high angles, where more strips have signals exceeding the

[1] For the test beam, the weighing of the widths was done according to equation 8.1. The impact of the difference to the procedure used in this chapter on the results was checked and found to be negligible.

threshold, the resolution reaches the expected 100 μm. For lower angles the μTPC method starts to lose precision, since fewer strips are firing and therefore less information is available for the fit. At the lowest angles the resolution deteriorates to almost 500 μm. One important quantity that can be obtained from figure 11.1 is the turn-over point where the μTPC method becomes better than the centroid algorithm. For the standard configuration this is around 16°. This angle can become one criterion in the combination of clusterization algorithms discussed in section 11.2.4. The other important parameter to be assessed is the reconstruction efficiency. Figure 11.2 displays the reconstruction efficiency for both methods. Exemplarily only layer 0 is depicted, but the results are the same for the other layers. The centroid method shows an efficiency close to 100 % for most of the angular range. The slight drop and the gap around 24° are consequences of the transition between the inner and the outer modules. For very low angles the efficiency starts to drop to 96.7 % due to geometrical reasons, e.g. if the muon is still in the acceptance of the NSW but has already missed the first layer. The efficiency for the μTPC method is in the order of 98 % in the plateau region. For lower angles it decreases down to 92 %. The reason for that is the lower number of strips in a cluster, which reduces the amount of information included in the fit. Furthermore the resolution of the time measurement of a single strip gets worse for lower angles as discussed in section 10.3.7. This leads to a bad reconstruction of the angle. The efficiency for the μTPC is determined using the recovery method described in section 11.2.2, hence, a layer can become inefficient if either the μTPC method has reconstructed an unreasonable angle or the fit has failed. Another reason for a non-efficient layer would be the presence of only a single strip exceeding the threshold.

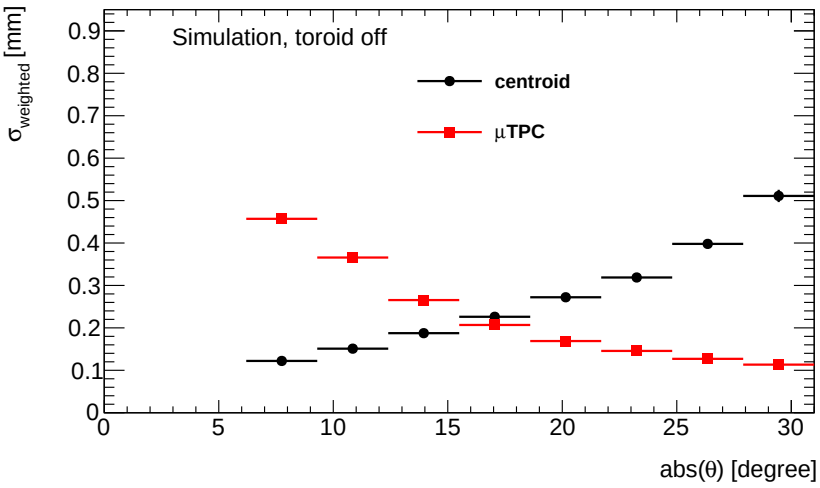

Figure 11.1.: Weighted position resolution for the centroid (black) and μTPC (red) methods as a function the incident angle θ using the nominal settings of the digitization. The resolution is extracted via a double Gaussian fit on the residuals in each angular bin and then weighing the standard deviations with the integrals of the individual Gaussians.

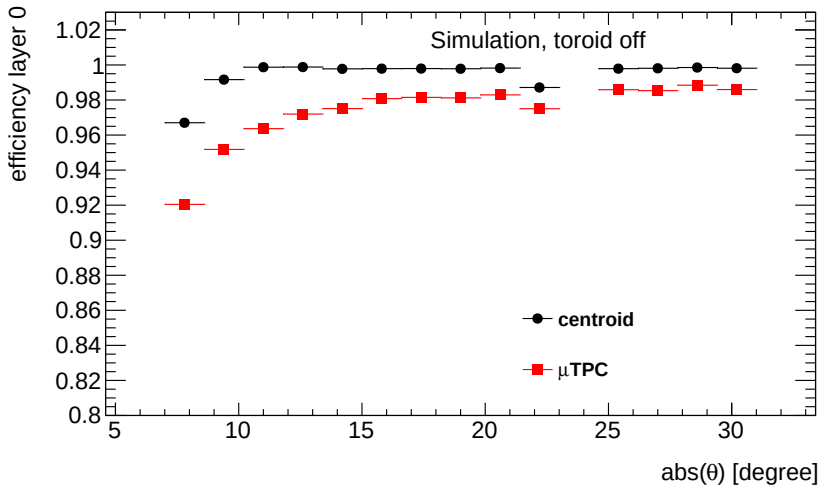

Figure 11.2.: Single layer reconstruction efficiency of the centroid (black) and the μTPC (red) methods as a function the incident angle θ using the nominal settings of the digitization.

11.3.3. Performance Depending on Charge Sharing and the VMM Settings

As already shown for the optimization of the digitization in section 10.3, CS has a significant impact on the performance of the Micromegas, especially on the time resolution. Also settings of the VMM, like the threshold or the NL, can make a difference.

In this section, the impact of these settings on the performance of the cluster reconstruction methods is discussed. Three values for the CS ratio are considered: 0, 0.3, and 0.5, where the first one serves as a benchmark for the reconstruction methods on a hypothetically perfect detector. The second value represents the mean value for CS over all strip lengths and the last value covers the region of the longest strips. For the charge threshold, two settings are included: a threshold of 15 000 electrons and one of 25 000 electrons. Again the first value corresponds to the mean value for all strip lengths, while the second value covers the region of the longest strips.

Figure 11.3 (11.4) shows the resolutions (efficiencies) for the different cluster reconstruction methods and parameters as a function of the track incident angle θ. In the plots on the left (right) the NL of the VMM is disabled (enabled). In the upper (lower) diagrams a charge threshold of 15 000 electrons (25 000 electrons) referred to as lower (higher) threshold is applied. The results obtained with the centroid reconstruction method are shown in black, the ones with the μTPC method are indicated by the colored markers where the color depends on the amount of CS that was applied in the simulation. The results with a CS ratio of 0.0, 0.3, and 0.5 are indicated in red, green, and blue, respectively. Charge sharing also impacts the resolution and efficiency of the centroid method but only at very high angles and independently of the amount of charge that is

shared. Therefore only the results for a CS ratio of 0.3 are included here for the centroid method[2]. In the following the impact of the different parameters on the performance of the reconstruction is discussed, referencing the relevant diagrams in figures 11.3 and 11.4 when needed. First the impact of the variation of the threshold and the influence of the NL on the performance of the centroid method are presented. Then the effect of CS, the threshold, and the NL on the performance of the μTPC method are discussed individually for each of those three parameters.

Performance of the Centroid Method: As expected, the centroid reconstruction method yields a weighted resolution of about 100 μm at low incident angles independently of the threshold and the NL. For higher incident angles the resolution rises to values of about 400 – 540 μm. A higher threshold increases the resolution at large angles, while the NL is able to recover it. The reconstruction efficiency with the centroid method is independent of the NL since already a single strip counts as a centroid cluster. For lower thresholds, the efficiency is almost 100 % over the full angular range. For higher thresholds, the efficiency drops as a function of the incident angle but only by about 2.5 %.

Impact of Charge Sharing on the μTPC Method: For the case of no CS (red points) the μTPC method yields resolutions of around and below 100 μm. This hypothetical scenario serves as a benchmark to verify that the μTPC method itself and its implementation within athena are working fine. Enabling CS increases the resolution, especially at low incident angles where fewer strips are included in the cluster formation. For smaller angles, a CS value of 0.3 (0.5) increases the resolution to about 400 – 500 μm (630 – 800 μm) as indicated by the green (blue) markers. At high incident angles the impact of CS is less pronounced. For a CS ratio of 0.3 (0.5) the resolution obtained at 30° is in the order of 120 – 140 μm (160 – 200 μm). The loss of spatial resolution due to CS can also be observed in the distribution of the track angle as reconstructed by the μTPC method compared to its true value, as shown in figure 11.5. In the plot only events with muon incident angles above 25° are included. For the case of CS disabled, the distribution is symmetric around a peak value of 7° while in the case of a correct angle reconstruction a peak position at 0° would be expected. This offset most likely stems from the positions of the first and last ionizations above the corresponding strips. However it will be subject to further investigation. With CS enabled, the peaks of the distributions move towards higher angles while the distributions alse become asymmetric towards higher angles. This behavior matches the angular distributions observed in the test beam, shown in figure 8.8. The more charge is shared, the more asymmetric the distribution becomes and also the more the peak moves to larger angles. Both can be explained by the fact that CS biases the time measurement of the outer strips towards the time values of the inner strips which receive more charge, as is discussed in section 10.3.6.
The efficiency of the μTPC method as a function of the incident angle, shown in figure 11.4, also depends a lot on the amount of CS. For the case of no CS the efficiency reaches values of

[2]The resolution and efficiency plots for the centroid method for different values of the CS ratio can be found in the appendix in figure A.1.

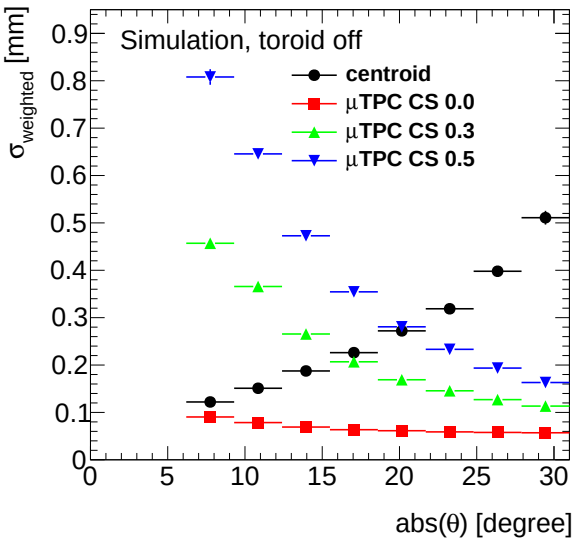

(a) NL Off, Threshold 15 k e

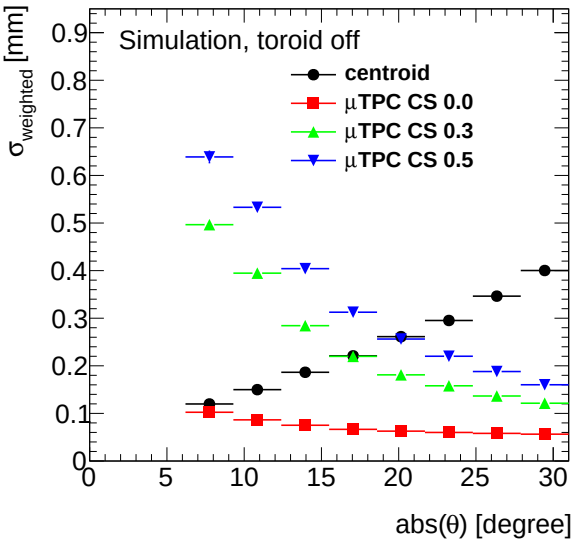

(b) NL On, Threshold 15 k e

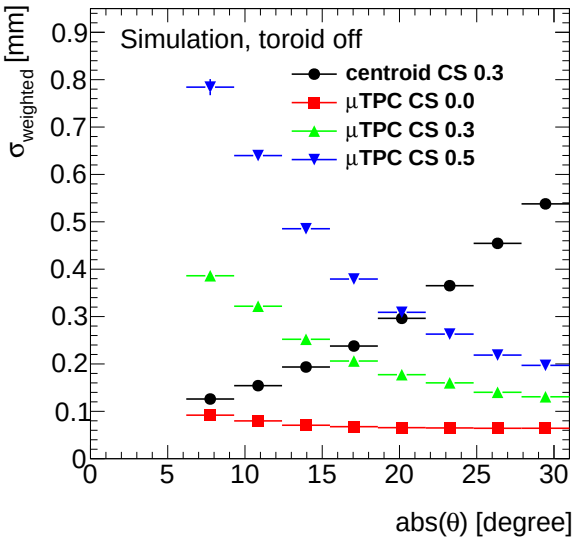

(c) NL Off, Threshold 25 k e

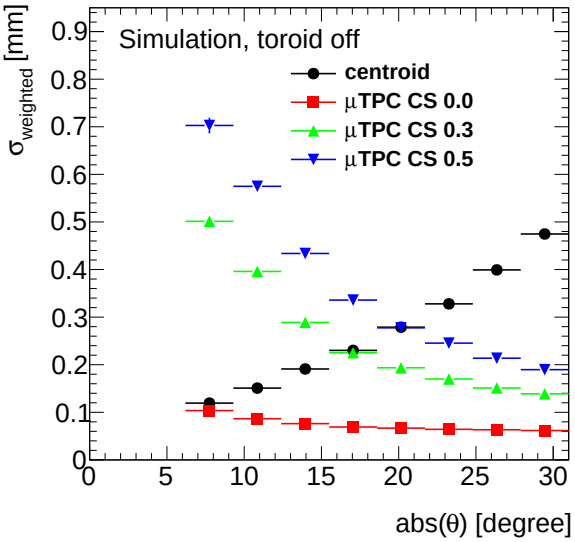

(d) NL On, Threshold 25 k e

Figure 11.3.: Weighted resolution of the μTPC and the centroid methods for different magnitudes of CS and different settings for the threshold and the NL. The CS values indicated in the legends refer to the ratio of charge shared with the next neighbor; the corresponding ratio for the next-to-next neighbor is the square of that value. For the centroid method the weighted resolution for the default value of 0.3 is shown.

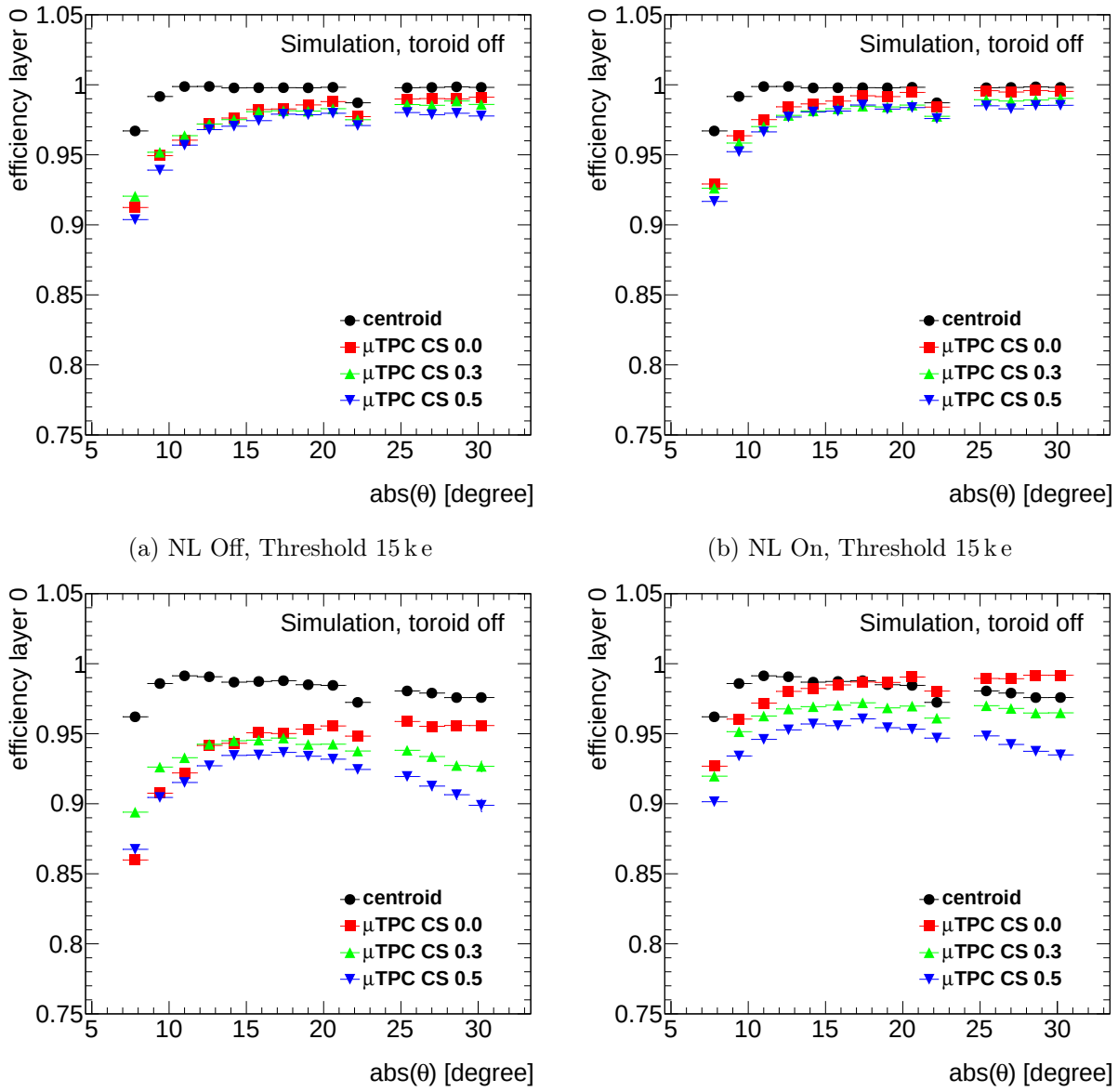

(a) NL Off, Threshold 15 k e

(b) NL On, Threshold 15 k e

(c) NL Off, Threshold 25 k e

(d) NL On, Threshold 25 k e

Figure 11.4.: Reconstruction efficiency for the μTPC and the centroid methods for different magnitudes of CS and different settings for the threshold and the NL. The CS values indicated in the legends refer to the ratio of charge shared with the next neighbor; the corresponding ratio for the next-to-next neighbor is the square of that value. For the centroid method the efficiency for the default value of 0.3 is shown.

95.5 – 99.5 % at high angles, and then decreases towards lower values of θ. With CS enabled, the efficiency reaches a plateau at an incident angle of about 18° and then either stays constant or starts to decrease again towards higher angles, depending on the threshold. The decrease is much more pronounced for the higher value of CS indicated by the blue points.

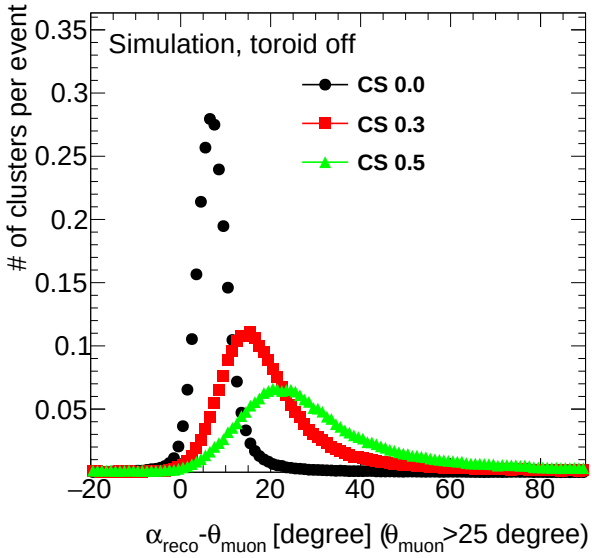

Figure 11.5.: Difference between muon incident angle and the angle reconstructed by the μTPC method for different levels of CS. The plot is produced with a threshold of 15 000 electrons and the NL disabled.

Impact of the Threshold on the μTPC Method: The charge threshold impacts the spatial resolution of the μTPC method mainly at low incident angles. A higher threshold (bottom row of 11.3) has the tendency to improve the resolution at low angles for the medium CS value (green markers). For a high CS ratio (blue points) the situation is vice versa. At large incident angles the resolution is barely impacted by the threshold setting used in the simulation ($\leq 20\,\mu$m difference). For the reconstruction efficiency of the μTPC method as a function of the incident angle, the threshold plays an important role. At lower thresholds (upper row in figure 11.4) the reconstruction efficiency reaches a plateau at an angle of roughly 18° and then stays constant towards larger angles. For higher thresholds (bottom row) the plateau is also reached, but then the efficiencies start to drop drastically towards larger angles, especially for the case of high CS (blue points). This can be explained by the fact that at higher angles the total charge is spread over more strips, leading to less charge on an individual strip which reduces the chance of exceeding the threshold. For higher CS the charge is spread over even more strips which further reduces the chance of each individual strip to cross the charge threshold.

Impact of the Neighbor Logic on the μTPC Method: The impact of the NL on the resolution of the μTPC method can be seen by comparing the left column (NL off) in figure 11.3 with the right column (on). As for the threshold, the main effect can be observed at low incident angles. Here the NL has a negative (positive) impact on the resolution for lower (higher) CS indicated by the green (blue) markers. This brings the two curves with low and high amounts of CS closer together when the NL is enabled. At larger incident angles the impact of the NL on the resolution is below 10 μm for all different cases and therefore negligible. In terms of efficiencies, the NL has no impact on the general shape of the plots shown in figure 11.4 but increases the value of the efficiency by a few percent.

Summary: It can be concluded that CS and also the parameters of the readout electronics have a significant impact on the precision and reconstruction efficiency of the different reconstruction methods. The performance of the centroid method is mostly insensitive to the different settings of the digitization, especially in terms of the efficiency, but by construction fails to provide reasonable position resolutions at high incident angles. The μTPC method has a reasonable resolution at very high angles, but at lower angles it is highly dependent on the amount of CS and the threshold value. Furthermore the reconstruction efficiency of the μTPC method suffers at higher thresholds, which is to be expected for the longest strips in the NSW. Therefore a combination of the different methods, as suggested in section 11.2.4, will need to be deployed in order to improve the overall reconstruction performance.
The results obtained with the μTPC method on simulated events are a lot better than those for the test beam data (see section 8.3.4), especially in terms of efficiency but also for the precision. The main reason for that is the very high noise levels that were present in the test beam, exceeding 25 000 electrons which was chosen as the upper threshold value for the simulation since the noise levels could be improved after the test beam. Also, as discussed in section 10.3.7 already, the simulation generally yields too optimistic results for the time resolution compared to measurements carried out at the actual detectors. Furthermore it needs to be noted that the results for the efficiency are not fully comparable, since some recovery methods for the efficiency were implemented for the μTPC method in athena after completion of the test beam studies as a result of the impact of the noise levels that have been observed.

11.3.4. Performance with Time Smearing

As shown in the previous section and also discussed in section 10.3.7, the simulation of the Micromegas yields too optimistic values for the time resolution. This has a direct impact on the performance of the reconstruction. Therefore a smearing of the hit time needs to be applied in the digitization. In the following, the performance of the reconstruction with time smearing will be discussed. Figure 11.6 shows the reconstruction performance where a Gaussian smearing with a width of 20 ns is applied on the time measurement. Together with the intrinsic time resolution of 15 ns obtained with the digitization, this yields an overall time resolution of 25 ns, compatible

with the measurements on the final detectors in the cosmic ray test stand. For all other settings the default parameters of the digitization were applied, i.e., a CS ratio of 0.3, a threshold of 15 000 electrons, and the NL disabled.
By construction the time smearing has no impact on the centroid reconstruction method. Therefore the same samples as for the plots above are used for the results of the centroid method. However, the μTPC reconstruction method is heavily impacted by the time smearing. The resolution at low angles is comparable to the case without time smearing, but rather than quickly dropping towards higher angles, the resolution slowly decreases up to an angle of 20° and then starts rising again, barely improving the resolution of the centroid at high angles. In terms of efficiency, the shape is similar to the case without time smearing but with lower efficiency values. The efficiency at the plateau drops from 98 % to 94.5 %. The decrease in efficiency towards lower angles is stronger compared to the case without time smearing. While in the latter case the efficiency stays above 90 % even for the lowest angles, it drops to below 80 % with the time smearing applied, still including the recovery mechanisms.
This degradation of the μTPC performance together with the results from the test beam made it advisable to develop and implement different reconstruction methods which ideally have the efficiency of the centroid method and the precision of the μTPC method. An effective way to achieve this is to use the information on the incident angle in the reconstruction algorithm. This information is used in the CTP (see section 6.3.2) and in the constrained μTPC (see section 6.3.4) methods, which are also included in the plots shown in figure 11.6. At low angles the CTP method yields resolutions of 100 μm compatible with the centroid algorithm. But with a rising angle, the CTP method improves the resolution drastically compared to the values obtained with the centroid or μTPC procedures. At 30° a resolution of 250 μm is reached, improving the centroid method by almost 250 μm. For the settings without time smearing applied, the CTP method yields resolutions well below 100 μm, over the full angular range. Since this is assumed to be too optimistic given the underestimated time resolution, the CTP algorithm was not included in the plots shown in the previous sections. For the efficiency the CTP method shows the same values as the centroid one, since the way of grouping strips into clusters is the same. The CTP method differs from the μTPC one in two major points which explain the improvements. As discussed, the incident angle is an external parameter to the former algorithm allowing its determination in a more precise way than with a fit of a 5 mm short track segment in a Micromegas drift gap, since it can be taken from a track segment reconstructed by all 16 layers of the NSW. The second major difference is the weighing of the time value by the measured charge. In the future, one could try to scale the uncertainties of the strips entering the μTPC fit according to the measured charge.
The constrained μTPC method does not take a fixed input angle but constrains the angular parameter in the final fit, which determines the position of the cluster, to the input with a customizable width. For the results shown in figure 11.6 a narrow constraint of 3° has been chosen. In this case, with the time smearing applied, the method is able to reduce the resolution at angles above 25° compared to the centroid method and improves it at 30° by 100 μm. Furthermore it

yields better results than the unconstrained μTPC method over the full angular range. Efficiency-wise the constrained method has a plateau for high angles at a value of 97 %, but the efficiency is dropping much quicker at angles below 15° compared to the unconstrained μTPC method. Since the results obtained with the CTP method look much more promising, any further optimizations of the constrained μTPC algorithm, e.g. changing the width, were not performed.
For both the constrained μTPC and the CTP methods, the incident angle was determined by assuming that the muon comes from the interaction point. This assumption holds true for the samples used to produce these plots but it is not always the case for the actual data from proton-proton collisions. Therefore both methods will not be applicable in the first step of the clusterization. But given the robustness of the CTP method against a bad time resolution it is a good candidate to be employed at a later stage of the track reconstruction where the incident angle can be obtained from the combination of the NSW layers, i.e., the segment.

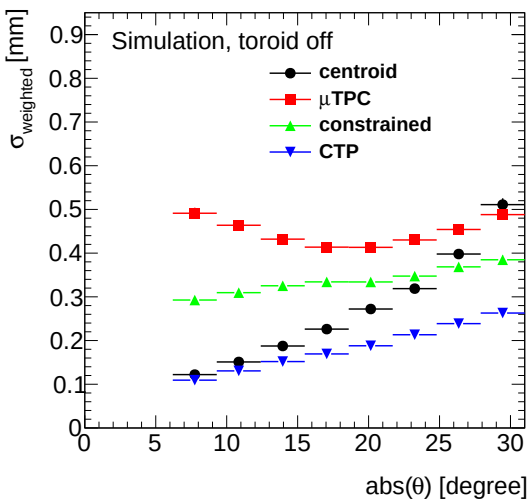

(a) Weighted resolution

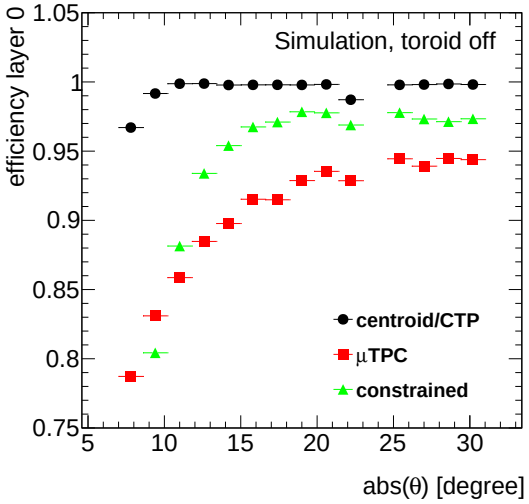

(b) Reconstruction efficiency

Figure 11.6.: Reconstruction performance with a smearing applied to the time measurement. The sample used for these plots was produced with the nominal parameters of the digitization, i.e. a CS ratio of 0.3, a threshold of 15 000 electrons, and the NL being disabled, but adding a Gaussian smearing of 20 ns to the time measurement. Since the centroid and the CTP methods use the same technique to form a cluster, i.e. combining adjacent strips with a signal above threshold, they have the same efficiency and only the curve for the efficiency of the centroid algorithm is shown (black).

11.4. Correction of Magnetic Field Effects on the Cluster Position

For all figures discussed up to now, the simulation was performed without the magnetic field of the toroid magnet. This was done to be able to compare the results with those from cosmic data

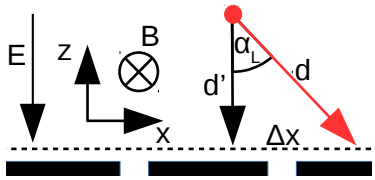

Figure 11.7.: Sketch of the correction of the magnetic field. The red dot indicates the location of a primary ionization from where the electrons would drift along the black arrow. But due to the magnetic field they drift under the Lorentz angle α_L(red arrow). This increases the drift time and changes the position where the electrons arrive at the mesh. The corrected drift distance d', corresponding to the case of no magnetic field, and the offset in position Δx can be determined knowing α_L and the measured drift distance d.

taking, but also to analyse the reconstruction performance without any distortions due to the non-linear field. The field impacts the cluster shape and position by deflecting the electrons that drift through the gas gap towards the mesh. The magnitude of the deflection is proportional to the Lorentz angle. The correlation between the magnetic field and the Lorentz angle was determined using the gas simulation software Magboltz [93]. The digitization uses a fourth-order polynomial to parametrize it which was implemented prior to this thesis in [71].

For the Micromegas the two components of the magnetic field orthogonal to the drift field are relevant. Since the position of a cluster is reconstructed in the orthogonal direction to the strips, the field component parallel to the strips has the biggest impact on the resolution. The component orthogonal to the strips only deflects the drifting electrons along a strip which is less relevant since the resolution in that direction is worse by design of the detector. Up to now only the impact of the parallel component is included in the simulation but it is planned to add the second direction as well. In the scope of this thesis the general concept for the correction of the magnetic field effects was introduced. An illustration of the correction principle is shown in figure 11.7. The red dot indicates the position of a primary ionization. The electrons drift under the Lorentz angle α_L with respect to the electric field, indicated by the red arrow. The calibration needs to recover the difference between the position where the electrons arrive at the mesh, denoted by Δx, and the original drift distance d', which is needed for all time-based reconstruction methods. Knowing the drift distance d extracted from the time measurement of each strip and the Lorentz angle α_L computed from the field strength parallel to the strip, the two relevant quantities can be obtained as follows:

$$d' = d\cos(\alpha_L) \quad \text{and} \quad \Delta x = d\sin(\alpha_L). \tag{11.1}$$

This makes the corrected position of the strips and therefore all the reconstruction methods, including the centroid method, time-dependent.

Figure 11.8 displays the distribution of the magnetic field component parallel to the strips in a

large Micromegas sector for the outermost gas gap. The field is non-uniform both in x and y directions. In the center of the sector the strongest field strength can be observed while at the outer positions it gets weaker or even flips polarity. While most of the field is dominated by the end-cap toroid, the very outer part of the sector is also under the influence of the field from the toroid coils in the barrel region. This leads to a strong field with the polarity opposite to the central part. These non-uniformities of the field strength, especially along the strips, referred to as the x direction herein, does not allow to perform the calibration in the initial clusterization. The reason is that the position along the strip cannot be obtained from a single layer. Therefore an algorithm has been developed, which allows to recalculate the cluster positions during the fit of the segments and the fit of the full muon track through ATLAS using the track position along the strip. The segment employs all 16 layers of the NSW and obtains the position along the strips by combining the stereo and the η layers of the Micromegas and the wires of the sTGC detectors. In addition the fit of the muon track through the full ATLAS detector receives additional information on the second coordinate by other detectors, e.g. the TGCs on the Big Wheels or the inner detector. For the recalculation of the cluster position the magnetic field is taken at the 3D position of the track on the surface of the detector layer. This allows the use of the coordinate along the strips.

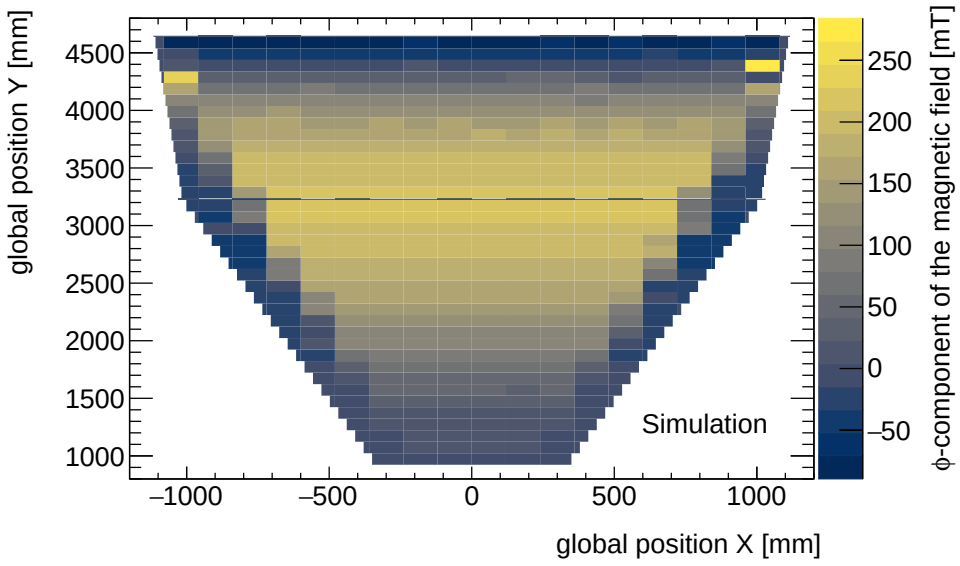

Figure 11.8.: ϕ - component of the magnetic field in a large Micromegas sector. The color coding indicates the magnitude of the field in units of mT. The plot was created by filling the magnetic field at the position of the reconstructed cluster and then taking the mean value of all entries per bin. Missing bins are due to the lack of a particle traversing that particular region of the sector. The plot is exemplarily done using layer 8 of the large sector number 5 mounted at the 12 o'clock position.

Figure 11.9 shows the mean residuals for all even gas gaps in large Micromegas sectors for the A-side of ATLAS ($\eta > 0$) with and without the correction applied. The selection of gas gaps included in the plot is based on the polarity of the magnetic field compared to the direction of the drift field, which is the same for the selected gaps. Without this selection the mean residuals would cancel each other out. It can be seen that the mean residuals as a function of the incident angle without the correction of the field follow the shape of the magnetic field. A maximum deviation of the mean residuals of 130 μm can be observed. With the correction enabled the residuals get closer to zero for the full range. Therefore it can be concluded that the correction of the magnetic field is sufficiently effective. The remaining small variation of the mean residuals as a function of the angle and the field are subject to further investigations.

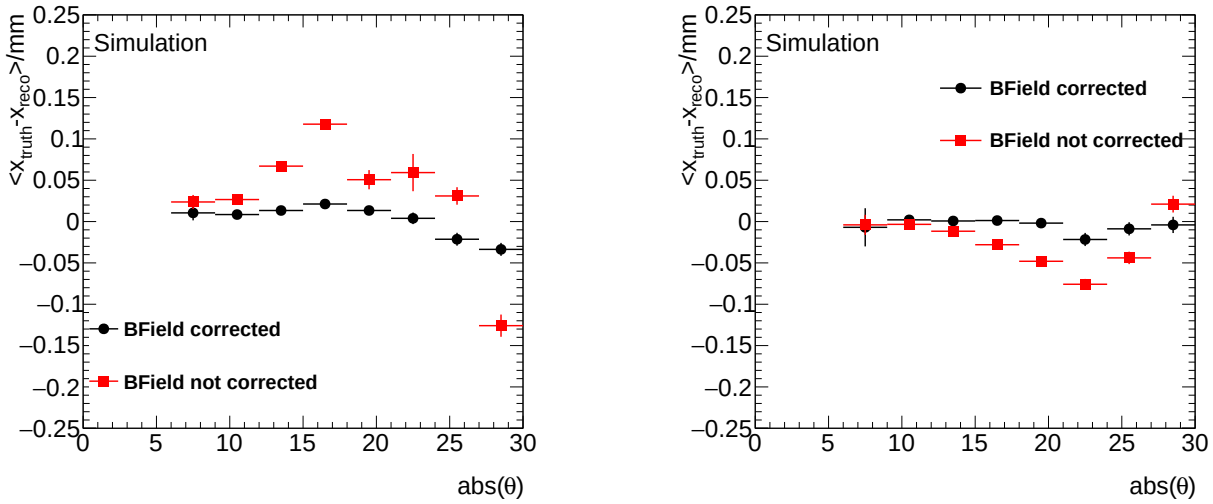

(a) Large Micromegas sectors

(b) Small Micromegas sectors

Figure 11.9.: Mean track residuals with and without the correction of the magnetic field. The plot is done using all even gas gaps on the A side ($\eta > 0$) of ATLAS, with large (a) and small (b) sectors separated. Without the magnetic field correction the shape of the mean residuals follows the magnetic field, while with the correction enabled the mean residuals get closer to zero. The remaining small variations of the mean residuals are subject to further investigations.

11.5. Summary of the Work on the Reconstruction

In the scope of this thesis, significant contributions have been made to the part of the ATLAS reconstruction software which processes the signals from the Micromegas, reconstructs the clusters together with their positions on the individual layers, and uses these clusters in the track fitting of the full ATLAS detector.

First, different methods to build clusters and determine their positions on the individual Micromegas layers have been integrated into the software. The focus was laid on those methods that exploit the drift time measurement for the cluster reconstruction, which is crucial to achieve the required spatial resolution for the inclined particle tracks present in the NSW. Amongst the methods under study were the μTPC algorithm and two methods aiming for the recovery of performance in non-ideal detector conditions, the CTP and the constrained μTPC methods. Following their integration into the software, the performance of the different algorithms has been evaluated for different settings of the readout electronics, including the threshold and the NL, but also detector parameters like the CS ratio between strips. Furthermore, a scenario was studied where an artificial time smearing was applied to the simulated drift time measurements. This has been introduced since it was evident that the detector simulation yields a resolution that is too good compared to the actual value measured for the detectors (see section 10.3.7). Especially in that last scenario, it turned out that neither the μTPC nor the centroid methods alone would yield sufficient performance since they either suffer from an unacceptable resolution in particular ranges of incident angles or a degraded efficiency, or both. Therefore an algorithm which combines both methods has been implemented. For technical reasons it is not yet employed in the event reconstruction and will be finished after this thesis.
In addition to the centroid and μTPC methods, two more algorithms for the reconstruction of clusters have been implemented, namely the CTP and the constrained μTPC methods, where the latter one was developed as part of this thesis. Both methods exploit the information of an external estimate of the incident angle to improve the cluster position reconstruction. But since the estimate for the angle first needs to be obtained by a fit of the cluster positions in the Micromegas layers, these two methods can only be employed in a second clusterization step. Especially the CTP algorithm shows very promising results in terms of resolution and efficiency in the scenario with the time smearing applied. A weighted resolution of 100 μm (260 μm) was achieved for small (large) incident angles, constituting an improvement of the resolution at high angles by more than 200 μm compared to the results obtained with both the μTPC and the centroid methods. In terms of efficiency the CTP algorithm yields values close to 100 % for the full angular range present in the NSW. Therefore it will be used as the main cluster reconstruction algorithm in the upcoming data taking period of ATLAS and beyond, playing a key role for the precise reconstruction of muons which is crucial for the physics program of the ATLAS collaboration.
Following the performance studies, a procedure to correct the cluster positions from the impact of the magnetic field has been developed. Furthermore the algorithms to calibrate the raw data were introduced to athena within the scope of this thesis.

12. Summary for the Software Part

In the scope of this thesis, major contributions have been made to two key components of the ATLAS offline software framework, the first one being the simulation of events, i.e. the physics of a hard scattering of protons, the subsequent propagation of the final state particles through the detector, and the detector response and the readout electronics. The second component is the reconstruction of the final state particles given the signals produced by either the actual detector or its simulation. The contributions made in this thesis mainly targeted the processing of Micromegas data in both of these components of athena.
On the side of the first component, most of the work was carried out on the simulation of the detector and electronics response of the Micromegas, also referred to as digitization. First, several important improvements have been developed which help to better mimic the detector response, amongst them the implementation of the shaper response function of the VMM readout chip, a strip-length-dependent threshold, and the effect of CS between a resistive strip and the copper strips. Furthermore contributions to the technical performance of the Micromegas digitization have been made, without which the technical requirements necessary to simulate millions of events would not have been matched. In a second step, several quantities of Micromegas strip clusters obtained from simulated events have been compared to data taken with the cosmic ray test stand, which was used to verify the functionality of the final detector modules during their integration. Amongst the studied quantities were the charge and width of the cluster as well as the drift time distributions, especially the time resolution. The goal of this study was to optimize the different parameters of the digitization, e.g. the gas gain, the charge threshold, or the ratio of CS. With the optimized set of parameters obtained in these studies, the digitization describes the detector response well in general, but is a bit optimistic for certain parameters like the time resolution. In this specific case, and since the time resolution is of great importance for the performance of the position reconstruction with Micromegas detectors, an additional smearing of the time measurement is applied to the simulated data in order to match the results obtained with the actual detectors. The final configuration of optimized parameters will be used starting from the first round of large-scale event simulation for the upcoming data taking period of ATLAS.

On the side of the reconstruction, the main contribution was the development and integration of several drift-time-based clusterization algorithms into athena. Those are crucial in order to maintain a good spatial resolution for tracks that pass the detector under an angle, which applies to all particle tracks penetrating the NSW detectors in ATLAS. Afterwards the impact of different settings of the digitization, like the CS ratio, the threshold, or the NL, on both the resolution

and the efficiency of the different reconstruction algorithms was studied. Also the impact of the smearing of the time measurement on the reconstruction performance was investigated. Especially in the latter case it became evident, that none of the two reconstruction methods under study, i.e. the centroid and the μTPC algorithms, perform well enough to satisfy the requirements in terms of both reconstruction efficiency and position resolution to be applicable over the full range of track angles expected for the NSW. Therefore, two mitigation strategies have been applied. The first one is to combine the μTPC and the centroid method in order to exploit the positive aspects of both. The second mitigation strategy is the refinement of the cluster position by employing the additional information of an external estimate of the track angle obtained, e.g., by a fit of the centroid cluster positions in the NSW layers. This additional information is used in the CTP and the constrained μTPC methods. Like for the test beam, the CTP method shows most promising results even for the setting with the time smearing applied, i.e. a weighted spatial resolution of $100-260\,\mu$m depending on the incident angle and a reconstruction efficiency of close to 100 % over the full angular range. Therefore it will be the algorithm applied to reconstruct clusters in Micromegas detectors for the upcoming data taking period and beyond. Apart from the developments and studies of the cluster reconstruction methods, also the general workflow for the calibration of the raw data and the correction of the cluster positions for the impact of the magnetic field have been developed in the scope of this thesis. All these developments are key in the precise reconstruction of muon tracks, which are of fundamental importance for the physics program of the ATLAS collaboration.

13. Conclusion

The LHC is continuously improved with the goal to eventually provide a sevenfold luminosity increase in the year 2027, compared to its design value. This upgrade targets an improved sensitivity for the measurement of rare processes, which are predicted by the SM but have not yet been discovered, to further increase the precision in the measurement of known processes, and to potentially discover physics beyond the SM. In order to maintain their current excellent performance in the increased luminosity scenario, the experiments surrounding the four interaction points of the LHC undergo major refurbishments as well. One of the main upgrades of the ATLAS detector already targeting the upcoming data taking period starting in 2022 is the replacement of the inner-most end-cap of the Muon Spectrometer by the NSW. The NSW deploys two detector technologies, Micromegas and sTGCs, where the former mainly targets at maintaining the excellent tracking of the current SW at the substantially increased particle rates, while the latter technology focuses on the identification of events with high-momentum muons in the final state in real time. Both the excellent tracking and the fast event selection at trigger level are essential for the ATLAS physics program.

The objective of this dissertation was to characterize the tracking performance of the Micromegas, being one of the key parameters of the NSW. Special focus is set on the reconstruction of inclined particle tracks as they will be present in the NSW, since it covers an azimuthal angle of $8-31°$.

In a first step, the tracking performance of a Micromegas module from the early series production was studied during a dedicated test beam campaign as discussed in part II of this thesis with the results being summarized in chapter 9. The first of the two major goals was to validate that the VMM readout chip works well on a full-sized detector module, since it was the first time that a final detector module was read out with this chip. The second aim was to fully characterize the module's reconstruction performance for inclined tracks. For the general proof of function, the chamber was aligned perpendicular to the beam and the expected resolutions of around $100\,\mu$m were achieved together with reconstruction efficiencies of well above $90\,\%$. Therefore the readout of the module with the VMM is considered validated. Further studies carried out with the detector in the same orientation were targeting the mitigation of voltage instabilities in the amplification gap. First, the impact of different ratios between Argon and CO_2 in the operation gas were studied where an increased amount of CO_2 stabilizes the amplification field. It was proven that both the position resolution and the reconstruction efficiency reach the aforementioned values for all investigated gas mixtures. Second, the impact of a reduction of the amplification voltage

applied on the resistive strips from 600 V to 570 V was explored. Although the signal gain scales exponentially with the voltage also the reduced working point still showed the above-mentioned resolutions and an efficiency of 90 %. Based on this important study, the NSW community decided to accepted the loss of signal strength at 570 V in favor of the substantially more stable detector performance.
For the study of the reconstruction performance with inclined particle tracks, the detector module was tilted by 28° relative to the beam axis. Two algorithms were explored for the reconstruction of strip clusters, both exploiting additionally the time of arrival measured for each strip together with the position of the strips. Focus was laid on the μTPC method, since it was known to be able to reconstruct clusters from inclined tracks without any external information. Also it was proven to yield excellent spatial resolution on small-scale Micromegas detectors with strip lengths of about 10 cm. The situation during the test beam studies was different in so far as strips with a length of 1.7 m were examined, which are almost the longest strips present in the NSW. Additionally, due to non-perfect grounding of the test beam setup, significantly higher noise levels were observed, which the μTPC method was not resilient against. Core (weighted) resolutions of $202-285\,\mu$m ($312-411\,\mu$m) were achieved depending on the settings of the VMM, but especially the reconstruction efficiency deteriorated to values of $62-81$ % as a result of the noise levels. After the test beam had ended, the non-perfect grounding was resolved and the noise levels could be significantly reduced down to their theoretical lower limit. Another effect that impacts the μTPC performance is the CS between the copper and the resistive strips which negatively influences the precision of the time measurements. In the data obtained from the test beam, a CS ratio of up to 67 % was measured. In order to mitigate the shortcomings of the μTPC method, the CTP method was investigated as well. Compared to the μTPC it uses an external estimate of the incident angle together with the charge measured on each strip as additional information. Core (weighted) resolutions of $213-268\,\mu$m ($281-356\,\mu$m) were achieved, which are compatible with the results of the μTPC method. However, in terms of reconstruction efficiency the CTP method outperforms the μTPC one significantly by reaching values of $90-96$ %.

The second half of this thesis was dedicated to the simulation of muon events in the Micromegas detectors and the reconstruction of muon tracks with the ATLAS offline software athena. This work is described in part III of this document, and summarized in section 12. First, several major improvements were made to the simulation of the Micromegas chambers and electronics response, which are very critical in terms of mimicking the actual detector response. Amongst the new developments are the implementation of the actual VMM shaper response function, a strip-length-dependent threshold, and the modeling of CS between resistive and copper strips. Also the technical performance of the Micromegas digitization was significantly enhanced, which is critical for it to be included in the full simulation of billions of events in ATLAS. In order to take into account the voltage instabilities of individual Micromegas sections, a scaling of the gas gain according to the applied voltage was integrated into athena as well. After all the improvements were in place, the output of the simulation was compared to data obtained with the final detectors

and the different parameters of the digitization were optimized such that the simulation models the detector response in the most realistic way. Good agreement was observed in almost all examined quantities, except for the time resolution, where the digitization yields too optimistic results. Therefore a correction in the form of a Gaussian smearing will be applied on the simulated time measurements in the future.
For the reconstruction of real and simulated muon events, several drift-time-based cluster reconstruction methods have been integrated into athena. These are critical to maintain a high spatial resolution at large incident angles. Achieving the best possible resolution over the full spectrum of track angles is key for the precise reconstruction of muons, being a major ingredient to the physics program of ATLAS. The performance of the various reconstruction algorithms was studied as a function of different physics scenarios provided by the digitization. It was found that especially for the case of the time smearing applied, the CTP method outperforms all other algorithms, reaching a weighted resolution of 100 μm (260 μm) at low (high) angles with a reconstruction efficiency close to 100 %. These values correspond to what was observed in the test beam. Furthermore they are mostly in agreement with the requirements imposed by the physics motivation of the NSW, especially in terms of the reconstruction efficiency, demanding an excellent performance of the track reconstruction in order to ensure a high precision of the momentum measurement of muons. Due to the great performance of the CTP algorithm, it will become the default cluster reconstruction method for the upcoming data taking period and beyond. In addition, the general concepts for the correction of cluster positions as a function of the magnetic field and the calibration of the raw signal data, coming either from simulation or the detector, were introduced to athena.

With the work presented in this thesis, major contributions have been made to the understanding of the tracking performance of the Micromegas chambers deployed in the NSW. The cluster reconstruction algorithms developed together with the improved digitization will be used for all events processed from the start of the upcoming data taking period and therefore have a direct impact on all future physics analysis conducted in ATLAS.

Part IV.

Additional Material

A. Additional Material for the Software Part

A.1. Parameters of the VMM Shaper Response Function

Paramter Name	Value
K_0	1.584
K_1	$-0.792 - 0.115\,i$
α	$(PT\ 10^{-9})\,/\,1.5$
P_0	$1.263\,/\,\alpha$
P_1	$1.149\,/\,\alpha\ -\ 0.786\,i\,/\,\alpha$

Table A.1.: Parameters of the VMM shaper response function given in equation 10.2. The parameter PT refers to the configurable peaking time of the VMM given in ns. The parameters were kindly provided by [85].

A.2. Centroid Reconstruction Performance with Charge Sharing

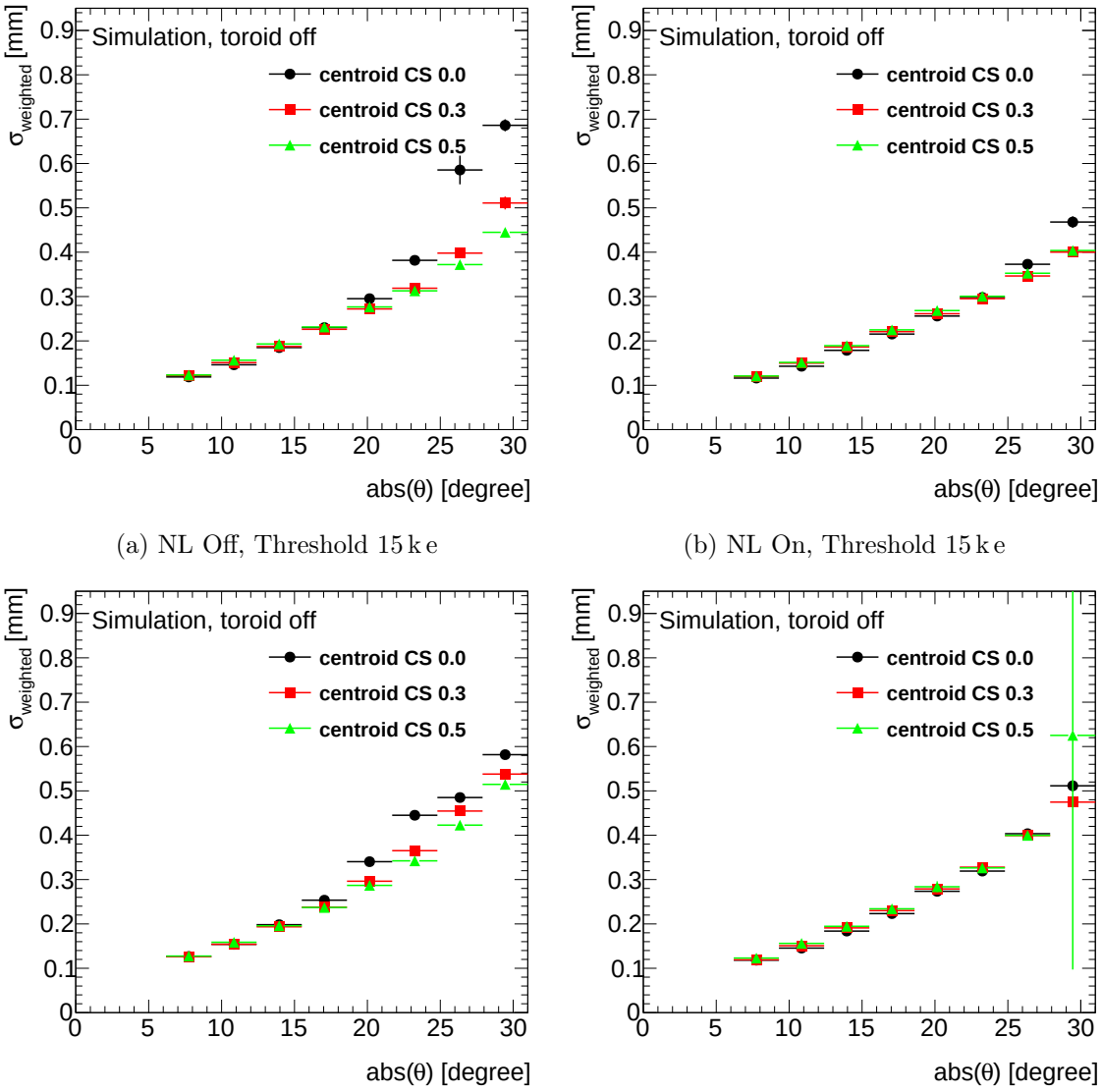

(a) NL Off, Threshold 15 k e

(b) NL On, Threshold 15 k e

(c) NL Off, Threshold 25 k e

(d) NL On, Threshold 25 k e

Figure A.1.: Weighted resolution of the centroid method for different magnitudes of CS and different settings for the threshold (top-bottom) and the NL (left-right). The resolution is extracted using a double Gaussian fit on the residuals and weighting the two widths of the Gaussians by their integrals. The CS indicated in the plots refers to the ratio of the charge shared with the next neighbor, the CS to the next-to-next neighbor is the square of that value.

A.3. μTPC Reconstruction Performance with Charge Sharing

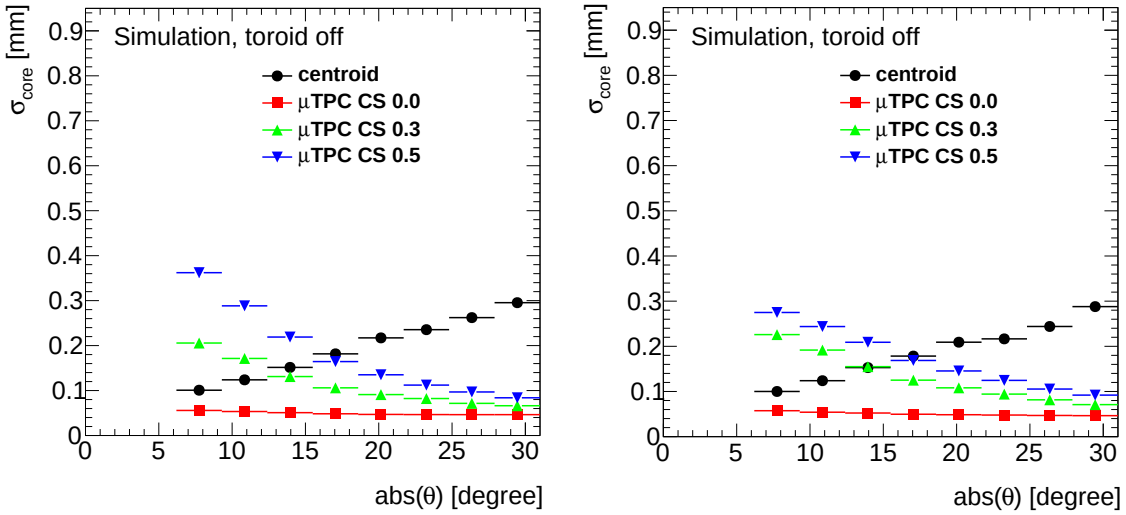

(a) NL Off, Threshold 15 k e

(b) NL On, Threshold 15 k e

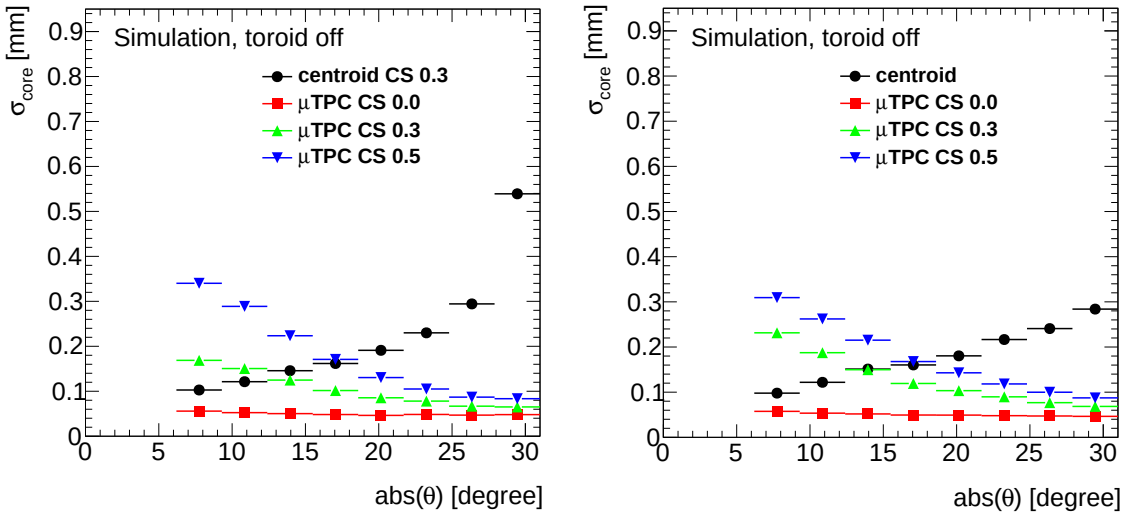

(c) NL Off, Threshold 25 k e

(d) NL On, Threshold 25 k e

Figure A.2.: Core resolution of the μTPC and the centroid methods for different magnitudes of CS and different settings for the threshold (top-bottom) and the NL (left-right). The resolution is extracted using a double Gaussian fit on the residuals and weighting the two widths of the Gaussians by their integrals. The CS indicated in the plots refers to the ratio of charge shared with the next neighbor, the CS to the next-to-next neighbor is the square of that value. For the centroid the core resolution for the default CS of 0.3 is shown.

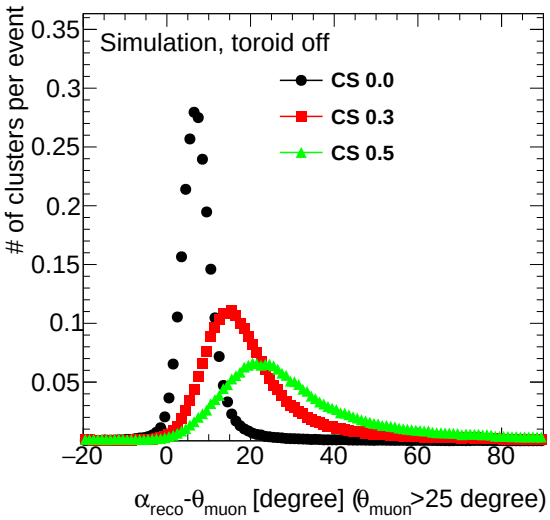

(a) NL Off, Threshold 15 k e

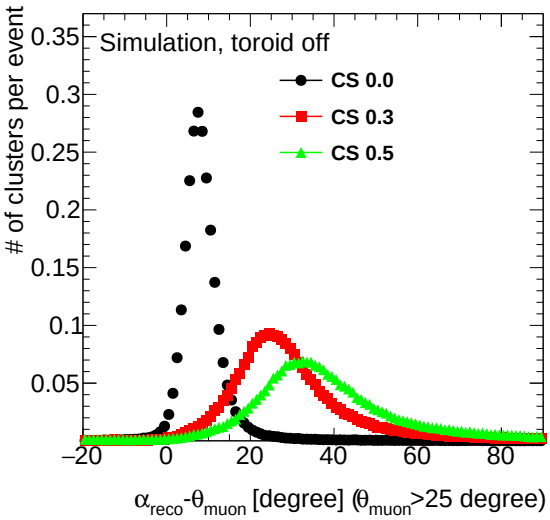

(b) NL On, Threshold 15 k e

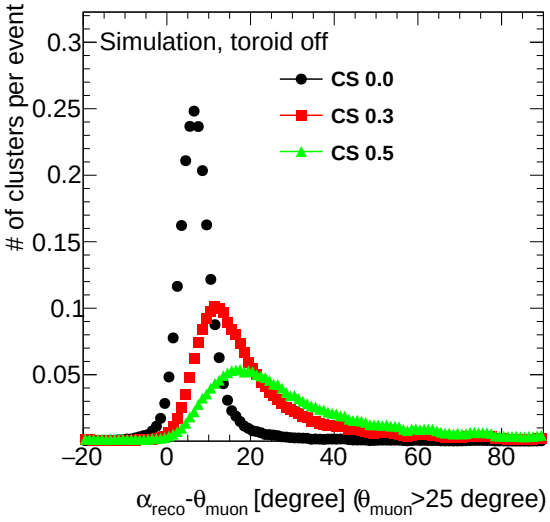

(c) NL Off, Threshold 25 k e

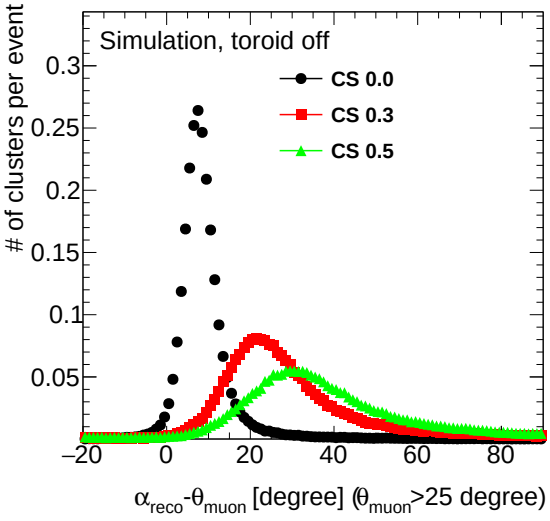

(d) NL On, Threshold 25 k e

Figure A.3.: Difference between muon incident angle and the angle reconstructed by the μTPC method for different levels of CS, and different configurations of the threshold (top-bottom) and the NL (left-right).

Bibliography

[1] P. Scholer for the ATLAS Muon Collaboration, *Test Beam Results and Performance Studies of ATLAS Micromegas Production Modules*, Journal of Physics: Conference Series **1498** (2020) 012053.

[2] New Small Wheel Collaboration, *New Small Wheel Public Results*, https://twiki.cern.ch/twiki/bin/view/AtlasPublic/NSWPublicResults. Accessed: Dec. 2021.

[3] ATLAS Collaboration, *Observation of a new particle in the search for the Standard Model Higgs boson with the ATLAS detector at the LHC*, Physics Letters B **716** (2012) 1 – 29.

[4] CMS Collaboration, *Observation of a new boson at a mass of 125 GeV with the CMS experiment at the LHC*, Physics Letters B **716** (2012) 30 – 61.

[5] G. Altarelli, *The Standard model of particle physics*, arXiv:hep-ph/0510281.

[6] G.'t Hooft, *Renormalizable Lagrangians for massive Yang-Mills fields*, Nuclear Physics B **35** (1971) 167–188.

[7] MissMj and Cush, *Standard Model of Elementary Particles*, https://en.wikipedia.org/wiki/File:Standard_Model_of_Elementary_Particles.svg. Accessed: Aug. 2021.

[8] LUMEN LEARNING. https://courses.lumenlearning.com/physics/chapter/4-8-extended-topic-the-four-basic-forces-an-introduction/. Accessed: Dec. 2021.

[9] S. L. Glashow, *Partial-symmetries of weak interactions*, Nuclear Physics **22** (1961) 579–588.

[10] A. Salam, *Gauge unification of fundamental forces*, Rev. Mod. Phys. **52** (1980) 525–538.

[11] S. Weinberg, *A Model of Leptons*, Phys. Rev. Lett. **19** (1967) 1264–1266.

[12] E. D. Bloom et al., *High-Energy Inelastic $e-p$ Scattering at 6° and 10°*, Phys. Rev. Lett. **23** (1969) 930–934.

[13] M. Breidenbach et al., *Observed Behavior of Highly Inelastic Electron-Proton Scattering*, Phys. Rev. Lett. **23** (1969) 935–939.

[14] Particle Data Group Collaboration, P. Zyla et al., *Review of Particle Physics*, PTEP **2020** (2020) 083C01.

[15] Y. Nambu, *Quasi-Particles and Gauge Invariance in the Theory of Superconductivity*, Phys. Rev. **117** (1960) 648–663.

[16] G. S. Guralnik, C. R. Hagen, and T. W. B. Kibble, *Global Conservation Laws and Massless Particles*, Phys. Rev. Lett. **13** (1964) 585–587.

[17] P. W. Higgs, *Broken Symmetries and the Masses of Gauge Bosons*, Phys. Rev. Lett. **13** (1964) 508–509.

[18] F. Englert and R. Brout, *Broken Symmetry and the Mass of Gauge Vector Mesons*, Phys. Rev. Lett. **13** (1964) 321–323.

[19] Super-Kamiokande Collaboration, *Evidence for Oscillation of Atmospheric Neutrinos*, Phys. Rev. Lett. **81** (1998) 1562–1567.

[20] KATRIN Collaboration, *First direct neutrino-mass measurement with sub-eV sensitivity*, `arXiv:2105.08533 [hep-ex]`.

[21] V. C. Rubin and W. K. Ford, *Rotation of the Andromeda Nebula from a Spectroscopic Survey of Emission Regions*, apj **159** (1970) 379.

[22] C. D. Anderson and S. H. Neddermeyer, *Cloud Chamber Observations of Cosmic Rays at 4300 Meters Elevation and Near Sea-Level*, Phys. Rev. **50** (1936) 263–271.

[23] J. C. Street and E. C. Stevenson, *New Evidence for the Existence of a Particle of Mass Intermediate Between the Proton and Electron*, Phys. Rev. **52** (1937) 1003–1004.

[24] UA1 Collaboration, *Experimental observation of lepton pairs of invariant mass around 95 GeV/c2 at the CERN SPS collider*, Physics Letters B **126** (1983) 398–410.

[25] LHCb Collaboration, *Test of lepton universality in beauty-quark decays*, `arXiv:2103.11769 [hep-ex]`.

[26] H. Kolanoski and N. Wermes, *Teilchendetektoren: Grundlagen und Anwendungen*. Springer, 2016.

[27] Particle Data Group, *Review of Particle Physics*, Phys. Rev. D **98** (2018) 030001.

[28] M. E. Rose and S. A. Korff, *An Investigation of the Properties of Proportional Counters. I*, Phys. Rev. **59** (1941) 850–859.

[29] F. Sauli, *Gaseous Radiation Detectors: Fundamentals and Applications*. Cambridge University Press, 2014.

[30] C. Montgomery and D. Montgomery, *Geiger-Mueller counters*, Journal of the Franklin Institute **231** (1941) 447–467.

[31] L. Evans and P. Bryant, *LHC Machine*, Journal of Instrumentation **3** (2008) S08001–S08001.

[32] M. L. Mangano, *The super-LHC*, Contemporary Physics **51** (2010) 211–231, https://doi.org/10.1080/00107510903367902.

[33] ATLAS Collaboration, *The ATLAS Experiment at the CERN Large Hadron Collider*, Journal of Instrumentation **3** (2008) S08003–S08003.

[34] CMS Collaboration, *The CMS experiment at the CERN LHC*, Journal of Instrumentation **3** (2008) S08004–S08004.

[35] P. Giubellino for the ALICE Collaboration, *The ALICE detector at LHC*, Nuclear Instruments and Methods in Physics Research Section A: Accelerators, Spectrometers, Detectors and Associated Equipment **344** (1994) 27 – 38.

[36] LHCb Collaboration, *The LHCb Detector at the LHC*, Journal of Instrumentation **3** (2008) S08005–S08005.

[37] ATLAS Collaboration, *Standard Model Summary Plots June 2021*, http://cds.cern.ch/record/2777014.

[38] G. Apollinari et al., *High-Luminosity Large Hadron Collider (HL-LHC): Preliminary Design Report*. CERN Yellow Reports: Monographs. CERN, Geneva, 2015. https://cds.cern.ch/record/2116337.

[39] ATLAS Collaboration, *Luminosity Public Results*, https://twiki.cern.ch/twiki/bin/view/AtlasPublic/LuminosityPublicResults. Accessed: Dec. 2021.

[40] ATLAS Collaboration, *Luminosity Public Results Run2*, https://twiki.cern.ch/twiki/bin/view/AtlasPublic/LuminosityPublicResultsRun2. Accessed: Dec. 2021.

[41] The HL-LHC Project. http://hilumilhc.web.cern.ch/about/hl-lhc-project. Accessed: Sep. 2020.

[42] F. Kuger, T. Trefzger, and C. Rembser, *Signal Formation Processes in Micromegas Detectors and Quality Control for large size Detector Construction for the ATLAS New Small Wheel*, Aug, 2017. https://cds.cern.ch/record/2277011.

[43] ATLAS Collaboration, *ATLAS inner detector: Technical Design Report, 1*. Technical Design Report ATLAS. CERN, Geneva, 1997. https://cds.cern.ch/record/331063.

[44] ATLAS Collaboration, *ATLAS inner detector: Technical Design Report, 2*. Technical Design Report ATLAS. CERN, Geneva, 1997. http://cds.cern.ch/record/331064.

[45] ATLAS Collaboration, *ATLAS Insertable B-Layer Technical Design Report*. Sep, 2010. https://cds.cern.ch/record/1291633.

[46] ATLAS Collaboration, *Production and integration of the ATLAS Insertable B-Layer*, Journal of Instrumentation **13** (2018) T05008–T05008.

[47] ATLAS Collaboration, *ATLAS liquid-argon calorimeter: Technical Design Report*. CERN, Geneva, 1996. https://cds.cern.ch/record/331061.

[48] ATLAS Collaboration, *ATLAS tile calorimeter: Technical Design Report*. Technical Design Report ATLAS. CERN, Geneva, 1996. https://cds.cern.ch/record/331062.

[49] ATLAS Collaboration, *ATLAS muon spectrometer: Technical Design Report*. Technical Design Report ATLAS. CERN, Geneva, 1997. https://cds.cern.ch/record/331068.

[50] ATLAS Collaboration, *ATLAS magnet system: Technical Design Report, 1*. Technical Design Report ATLAS. CERN, Geneva, 1997. http://cds.cern.ch/record/338080.

[51] ATLAS Collaboration, *ATLAS central solenoid: Technical Design Report*. Technical Design Report ATLAS. CERN, Geneva, 1997. http://cds.cern.ch/record/331067.

[52] ATLAS Collaboration, *ATLAS barrel toroid: Technical Design Report*. Technical Design Report ATLAS. CERN, Geneva, 1997. http://cds.cern.ch/record/331065.

[53] ATLAS Collaboration, *ATLAS end-cap toroids: Technical Design Report*. Technical Design Report ATLAS. CERN, Geneva, 1997. http://cds.cern.ch/record/331066.

[54] ATLAS Collaboration, *ATLAS Level-1 Trigger: Technical Design Report*. Technical Design Report ATLAS. CERN, Geneva, 1998. https://cds.cern.ch/record/381429.

[55] ATLAS Collaboration, *ATLAS high-level trigger, data-acquisition and controls: Technical Design Report*. CERN, Geneva, 2003. https://cds.cern.ch/record/616089.

[56] ATLAS Collaboration, *The ATLAS Data Acquisition system in LHC Run 2*, tech. rep., CERN, Geneva, Feb, 2017. https://cds.cern.ch/record/2244345.

[57] ATLAS Collaboration, *Git Repository of the ATLAS Offline Software*, https://gitlab.cern.ch/atlas/athena/. Accessed: Dec. 2021.

[58] GEANT4 Collaboration, *GEANT4 - A simulation Toolkit*, https://geant4.web.cern.ch/. Accessed: Aug. 2020.

[59] ATLAS Collaboration, *Letter of Intent Phase-I Upgrade*. CERN, Dez, 2011. https://cds.cern.ch/record/1402470.

[60] ATLAS Collaboration, *New Small Wheel Technical Design Report*. Geneva, Jun, 2013. https://cds.cern.ch/record/1552862.

[61] ATLAS Collaboration, *Letter of Intent for the Phase-II Upgrade of the ATLAS Experiment*, tech. rep., CERN, Geneva, Dec, 2012. https://cds.cern.ch/record/1502664. Draft version for comments.

[62] I. Roth, A. Klier, and E. Duchovni, *Testing sTGC with small angle wire edges for the ATLAS New Small Wheel Muon Detector Upgrade*, arXiv:1506.01277 [physics.ins-det].

[63] G. Iakovidis, *The Micromegas Project for the ATLAS Upgrade*, JINST **8** (2013) C12007, arXiv:1310.0734 [physics.ins-det].

[64] T. Kwan for the ATLAS Collaboration, *The New Small Wheel Project for the ATLAS Muon Spectrometer*, https://cds.cern.ch/record/2771658.

[65] Y. Giomataris et al., *MICROMEGAS: a high-granularity position-sensitive gaseous detector for high particle-flux environments*, Nuclear Instruments and Methods in Physics Research Section A: Accelerators, Spectrometers, Detectors and Associated Equipment **376** (1996) 29 – 35.

[66] D. Thers et al., *Micromegas as a large microstrip detector for the COMPASS experiment*, Nuclear Instruments and Methods in Physics Research Section A: Accelerators, Spectrometers, Detectors and Associated Equipment **469** (2001) 133 – 146.

[67] Y. Kataoka, S. Leontsinis, and K. Ntekas, *Performance studies of a micromegas chamber in the ATLAS environment*, Journal of Instrumentation **9** (2014) C03016–C03016.

[68] B. Al Atoum et al., *Electron transport in gaseous detectors with a Python-based Monte Carlo simulation code*, Computer Physics Communications **254** (2020) 107357.

[69] B. Flierl, *Particle tracking with micro-pattern gaseous detectors*, April, 2018. http://nbn-resolving.de/urn:nbn:de:bvb:19-221980.

[70] T. Alexopoulos et al., *Performance studies of resistive-strip bulk micromegas detectors in view of the ATLAS New Small Wheel upgrade*, Nuclear Instruments and Methods in Physics Research Section A: Accelerators, Spectrometers, Detectors and Associated Equipment **937** (2019) 125–140.

[71] G. Iakovidis, *Research and Development in Micromegas Detector for the ATLAS Upgrade*. PhD thesis, National Technical University of Athens, 2014. https://cds.cern.ch/record/1955475.

[72] K. Ntekas, *Performance characterization of the Micromegas detector for the New Small Wheel upgrade and Development and improvement of the Muon Spectrometer Detector Control System in the ATLAS experiment*, 2016. https://cds.cern.ch/record/2143887.

[73] P. V. C. Hough, *Machine Analysis of Bubble Chamber Pictures*, Conf. Proc. C **590914** (1959) 554–558.

[74] R. O. Duda and P. E. Hart, *Use of the Hough Transformation to Detect Lines and Curves in Pictures*, Commun. ACM **15** (1972) 11–15.

[75] OpenCV Dev Team, *Hough Line Transform*, https://docs.opencv.org/2.4/doc/tutorials/imgproc/imgtrans/hough_lines/hough_lines.html. Accessed: Nov. 2021.

[76] G. De Geronimo et al., *VMM1—An ASIC for Micropattern Detectors*, IEEE Transactions on Nuclear Science **60** (2013) 2314–2321.

[77] ATLAS Collaboration, G. Iakovidis, *VMM3, an ASIC for Micropattern Detectors*, Tech. Rep. ATL-MUON-PROC-2018-003, CERN, Geneva, Mar, 2018. https://cds.cern.ch/record/2309951.

[78] G. Sekhniaidze, *Clock and Trigger Generator and Fan-out for Scalable Readout System*, https://indico.cern.ch/event/676702/contributions/2818995/attachments/1575408/2487615/CTGF.pdf. Accessed: Nov. 2021.

[79] C. Bakalis, *Research and Development of the Electronics and Data Acquisition System for the New Small Wheel Upgrade of the ATLAS Detector at CERN and Performance Evaluation of the Micromegas Chamber.*, Jul, 2021. https://cds.cern.ch/record/2778078.

[80] D. J. Antrim, *Sweet Little Nothings; or, Searching for a Pair of Stops, a Pair of Higgs Bosons, and a Pair of New Small Wheels for the Upgrade of the Forward Muon System of the ATLAS Detector at CERN*, 2019. http://cds.cern.ch/record/2699575.

[81] A. Koulouris, *Performance characterization of the NSW Micromegas detector, services design and development of the Slow Control Adapter for the ATLAS upgrade.* , May, 2019. https://cds.cern.ch/record/2675805.

[82] G. Iakovidis, *VMM3a, an ASIC for tracking detectors*, Journal of Physics: Conference Series **1498** (2020) 012051.

[83] M. G. Herrmann, *Series calibration of segmented and multi-layered micromegas modules for ATLAS*, October, 2019. http://nbn-resolving.de/urn:nbn:de:bvb:19-250553.

[84] M. French et al., *Design and results from the APV25, a deep sub-micron CMOS front-end chip for the CMS tracker*, Nuclear Instruments and Methods in Physics Research Section A:

Accelerators, Spectrometers, Detectors and Associated Equipment **466** (2001) 359–365, 4th Int. Symp. on Development and Application of Semiconductor Tracking Detectors.

[85] G. Iakovidis. Personal communication, Sep, 2020.

[86] H. Schindler et al., *Garfield++*, `https://garfieldpp.web.cern.ch/garfieldpp/`. Accessed: Mar. 2021.

[87] CERN, *Documentation of the data analysis framework ROOT*, `https://root.cern.ch/`. Accessed: Sep. 2021.

[88] CERN, *TF1 Class Reference*, Sep, 2021. `https://root.cern.ch/doc/master/classTF1.html`. Accessed: Sep. 2021.

[89] L. Lönnblad et al., *CLHEP - A Class Library for High Energy Physics*, `https://proj-clhep.web.cern.ch/proj-clhep/`. Accessed: Sep. 2021.

[90] L. Martinelli. Personal communication, Jan, 2021.

[91] CERN, *TLinearFitter Class reference*, `https://root.cern.ch/doc/master/classTLinearFitter.html`. Accessed: Sep. 2021.

[92] CERN, *TMinuit Class Reference*, `https://root.cern.ch/doc/master/classTMinuit.html`. Accessed: Sep. 2021.

[93] S. Biagi, *A multiterm Boltzmann analysis of drift velocity, diffusion, gain and magnetic-field effects in argon-methane-water-vapour mixtures*, Nuclear Instruments and Methods in Physics Research Section A: Accelerators, Spectrometers, Detectors and Associated Equipment **283** (1989) 716–722.

List of Figures

List of Tables

Acknowledgements

At this point I want to take the chance and express my gratitude to all my colleagues, friends, and my family who supported me in the last years.

I want to thank my supervisors **Prof. Ulrich Landgraf**, **Dr. Stephanie Zimmermann** and **Prof. Gregor Herten** who offered me a very interesting topic and excellent support during my studies. I am especially thankful that you gave me the possibility to stay at CERN for over 2 years — conducting my research in such an international and very thriving environment was a very unique opportunity. I also appreciate that I got the chance the be part of the GRK 2044 which supported me financially and offered a very diverse and interesting scientific program. Furthermore I want to acknowledge the computing infrastructure that I got access to in Freiburg provided by the Black Forest Grid Initiative and the support by the state of Baden-Württemberg through bwHPC and the German Research Foundation (DFG) through grant no INST 39/963-1 FUGG (bwForCluster NEMO).

Special thanks is due to **Kim and Constantin Heidegger** especially for the great support received in the process of assembling this document under difficult circumstances. You also proofread my thesis the most, even on the weekends. Kim, we know each other since I started my Bachelor thesis in the group and you supported me through all the years. It was great to share the office in Freiburg with you, although I was not present that often. Also outside university all three of us had a lot of fun together, where I particular enjoyed the badminton games. And yes I will also come bouldering again once this thesis is done.
Thanks to **Thorwald Klapdor**, who joined the group at the end of my Bachelor studies, for the support and the interesting discussions throughout the years. I very much enjoyed the common coffee breaks and dinners whenever you visited CERN.
I am very grateful that I could spend a good fraction of time during the pandemic with **Ksenia Solovieva** and **Vladislavs Plesanovs** in our little "household"; you helped me to get distracted from continuous bad news and became good friends. Also the two of you helped in proofreading this thesis for which I want to say thank you.
Thank you to **Andrea Knue** for the advice you gave me during my thesis and for proofreading parts of it.
Jürgen Tobias and **Bernhard Pfeifer** offered me support in questions of the group's computing infrastructure and taught me a lot about designing mechanics. I very much enjoyed the discussions during our daily coffee breaks in Freiburg.

I also want to thank the other **members of the Herten and Heinemann group** for the great atmosphere we had on the corridor, the many interesting discussions, and also the activities outside work.

A very special thanks goes to all the colleagues at CERN, with whom I collaborated. Thanks to **Theodoros Alexopoulos**, who lead the test beam group, and to the whole team. It was a pleasure to work in such a highly motivated, dedicated and supportive team. Special thanks goes to **Kostas, Aimilianos, Christos, Christos, Polyneikis, Dimitris, Stavros, Alan, Ann, Alex, Gabriel, Luca, Valerio, Ralf, Felix, Philipp, Christoph, and Maximilian**. Thanks a lot to **George Iakovidis**, from whom I learned a lot about the μTPC method, the details of Micromegas, the VMM and the Micromegas digitization. Thanks to **Bernhard Flierl**, who was also part of the test beam team and who gave me the idea on the Cluster Time Projection which turned out to be very good. I also want to thank **Melissa Franklin** for the interesting discussion we had and to think of me in the most difficult moment of my thesis.
I want to thank all members of the muon software and NSW performance working groups, with whom I collaborated, for the great support. Special thanks goes to **Stefano Rosati** and **Mauro Iodice** for teaching me how to tame the beast called athena and the very detailed discussions on the performance of the digitization and reconstruction. Thanks as well to **Nicolas Köhler** and **Johannes Junggeburth** for the technical support.
Thanks as well to the colleges with whom I collaborated in order come up with a naming scheme for the NSW service connections and all the labels, especially to **Konstantinos Iakovidis** and **Aimilianos** who taught me about the thousands of services connections that needed to be named.

I also want to take the opportunity to thank people outside work. Special thanks to all members of the Psipsini crew; it was a pleasure to share the house with you during my time at CERN. Especially I want to mention **Mayank**, who became a good friend. We moved into the flat together and stayed there over the full time. You are a good student in terms of skiing and I really enjoyed the home-cooked Indian food.

A very special thanks is due to my parents and my brother! You always were my safe harbor, especially in the times when the pandemic started and I got stuck in Germany, but also in all the other times of my life. Thanks a lot for everything!!

Last but not least I want to come back to you **Stephanie**. Unfortunately you are not with us anymore when writing these lines, which is still such an devastating and highly incomprehensible loss to all of us. You offered me this very interesting topic and supported me over the years. It was a real pleasure to share the office with you during the my years at CERN and I really enjoyed the daily common lunches and coffee breaks, where I got the chance to get to know the inspiring personality behind the excellent physicist and NSW project leader that you were. Goodbye Stephanie and thank you for everything!

Erklärung

Hiermit versichere ich, die eingereichte Dissertation selbstständig verfasst und keine anderen als die von mir angegebenen Quellen und Hilfsmittel benutzt zu haben. Wörtlich oder inhaltlich verwendete Quellen wurden entsprechend den anerkannten Regeln wissenschaftlichen Arbeitens (lege artis) zitiert. Ich erkläre weiterhin, dass die vorliegende Arbeit noch nicht anderweitig als Dissertation eingereicht wurde.

Freiburg, den 25. Mai 2022

Patrick Scholer